Bose-Einstein Condensation of Photons

Jakov Marelić

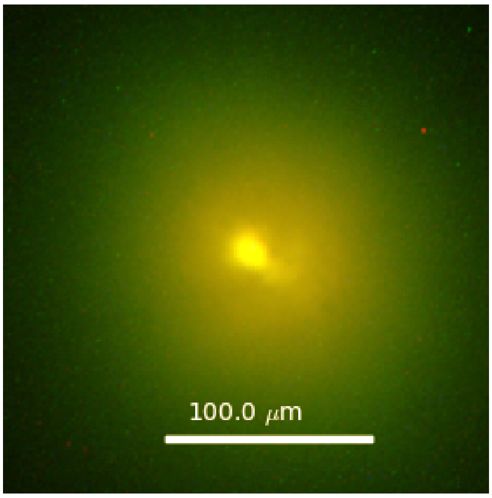

A thesis presented for the degree of
Doctor of Philosophy

Department of Physics
Imperial College London
United Kingdom
19th March 2018

Contents

List of Figures

Abstract

A Bose-Einstein condensate can be made of photons. The photons are held at thermodynamic equilibrium in a dye-filled microcavity and pumped with a laser. Thermalisation can be demonstrated and above the threshold a Bose-Einstein condensate will form. A Mach-Zehnder interferometer is built and used to measure the spatial and temporal first-order coherence under various conditions. We build a momentum-resolved spectrometer and use it to obtain views into the phase-space distribution of the photon condensate. We put an upper bound on the value of the interaction strength parameter and find that the microcavity system is ergodic even when not at thermal equilibrium. We build a setup to stabilise the pump laser power with the aim to observe the λ-point of the condensate.

Acknowledgements

Very few people achieve anything in isolation. I would like to thank the following for help with this project:

- Rob Nyman who was my supervisor and who had already built the laboratory by the time I arrived and had done several preliminiary experiments already.
- Ben Walker, Edward Ong, Lydia Zajiczek. Fellow students in the lab who played their part in the experiment and were great company.
- The Bonn group. Martin Weitz, Julian Schmitt, Jan Klaers, Frank Vewinger and others who made the first Photon BEC and allowed me to visit their laboratory.
- Our theory group collaborators Henry Hesten and Florian Mintert.
- Colleagues and friends from the Center for Cold Matter group at Imperial. For company, advice, borrowing equipment and talks.
- The technicians Jon Dyne, Melvyn Patmore, Stephen Maine, Valerijus Gerulis who were very helpful.
- Family members: Edita, Boris, Ana, Vicko, Krešimir, Luka, Mara, Elza.
- My friends and acquaintances.
- All the teachers, authors, lecturers and tutors who have educated and inspired me over the years.
- The netizens most of whom I only know via their IRC and github nicknames.

Declaration of Originality

I declare that this thesis is entirely my own work and that all else is appropriately referenced.

Copyright Declaration

Chapter 1

Introduction

This thesis is on Bose-Einstein condensate systems made of photons. It is structured in seven chapters, the first is this introduction which describes the theory of photon Bose-Einstein Condensation (BEC) and reviews the literature. Chapter 2 describes the experimental setup to create photon BEC. Chapter 3 describes the measurements taken to confirm that the observed phenomena were indeed true BEC. Chapter 4 and chapter 5 describe the interferometery and two-dimensional spectrometer experiments. Chapter 6 describes the laser stabilization setup and chapter 7 is the conclusion. I started my PhD studies in October 2013. For the next four years the group built up the experiment and obtained new scientific results, producing several published papers.

1.1 Bose-Einstein condensation

Bose-Einstein condensation (BEC) is a phase transition where bosonic particles macroscopically occupy the ground state of a system at thermal equilibrium. First predicted in 1924-25 by Bose and Einstein, this form of matter was not realised until advances in laser cooling allowed the condensing of an ultracold atomic gas in 1995 [1].

The average occupation number of $f(\epsilon)$ of a bosonic state at energy ϵ at thermal equilibrium can be found from counting statistics and is given by the Bose-Einstein distribution.

$$f(\epsilon) = \frac{1}{e^{(\epsilon-\mu)/k_B T} - 1} \tag{1.1}$$

where μ is the thermodynamic chemical potential, T is the temperature and k_B is the Boltzmann constant, suggesting this is valid for thermal equilibrium. Note that for $\mu < \epsilon$ the occupation is finite even if the total number of particles is infinite (in the thermodynamic limit the density of states is infinite). Bose-Einstein condensation happens when μ approaches the ground-state energy level (zero in this formulation) from below which causes $f(0) \to \infty$, making a very large number of the bosons in the system pile into the ground state. This is described as macroscopic occupation. Our definition of BEC is macroscopic occupation of the ground state at thermodynamic equilibrium.

It is worth briefly describing the statistical argument[2] which leads to equation 1.1. The distribution can be derived by considering a grand canonical ensemble where a system of non-interacting bosonic particles is able to exchange energy and particles with a reservoir, where the temperature T and chemical potential μ are held fixed. Due to the non-interacting nature of the particles, each single-particle energy level (with energy ϵ) forms a separate grand canonical ensemble of its own. Any number of bosonic particles n can be in a level, but as they are indistinguishable, each possible occupation number n is one microstate. We consider the resulting partition function Z:

$$Z = \sum_{n=0}^{\infty} \exp\left(\frac{-n(\epsilon-\mu)}{k_B T}\right) = \sum_{n=0}^{\infty} \left[\exp\left(\frac{-(\epsilon-\mu)}{k_B T}\right)\right]^n \tag{1.2}$$

$$= \frac{1}{1-\exp\left(\frac{-(\epsilon-\mu)}{k_B T}\right)} \tag{1.3}$$

Which is solved as a geometric series $(1+r+r^2+r^3+\cdots = 1/\left(1-r\right))$. From this we can obtain the average particle number $\langle n \rangle$ which applies for every single-particle level and therefore gives the occupancy number of the entire system:

$$\langle n \rangle = k_B T \frac{1}{Z}\left(\frac{\partial Z}{\partial \mu}\right)_{V,T} = \frac{1}{e^{(\epsilon-\mu)/k_B T}-1} = f(\epsilon) \tag{1.4}$$

An expression for the chemical potential μ as a function of number density and temperature of the ensemble can be found. Start with the expression for total number of particles $N = \int f(\epsilon)g(\epsilon)d\epsilon$ where $g(\epsilon)$ is the density of states and rearrange to find μ; this usually results in a transcendental equation. From that are found quantities like the critical number density and critical temperature for forming a BEC.

There are many physical system which exhibit BEC. Chronologically in the order of their first experimental achievement (although not necessarily in the order they were understood to be condensation phenoma): superfluid helium, atomic BEC first of Rubidium atoms but later other species of atoms and molecules, exciton-polariton condensation, photon BEC and plasmon BEC. Figure 1.1 shows data showing rubidium atoms going through the threshold of Bose-Einstein condensation and showing their macroscopic ground state occupation.

1.2 Superfluidity and Superconductivity

The earliest hint of BEC phenomena resulted from low temperature physics research in the early 20th century. The first achievement of helium in the liquid state by Kamerlingh Onnes in 1911 led to the discovery of superconductivity in some metals, where the electrical resistance vanishes. Superconductivity was given a theoretical explanation by Bardeen, Cooper and Shrieffer (BCS) theory in 1957[3]. Essentially the electrons which are fermions combine into pairs at the BCS transition. The resulting bosonic particles are called Cooper pairs which undergo something like Bose-Einstein condensation where a macroscopically large number of them inhabit one state. They can then flow and carry current without viscosity. Thus the phenomena of superfluidity and superconductivity are inherently related, as superconductivity can be seen as finite current with zero voltage drop while superfluidity can be seen as finite current with zero pressure drop. Landau theory is a way to model superfluidity; a moving particle will not create excitations that carry away momentum as long as the Landau criterion is satisfied. A similar mechanism involving BEC has been proposed to model the inner structure of neutron stars[4], as the high-density neutrons may also form Cooper pairs which will have a nonzero condensate fraction, with a maximum inside the inner crust of such a star. BEC has also been proposed to occur in helium white dwarfs[5] and dark matter[6].

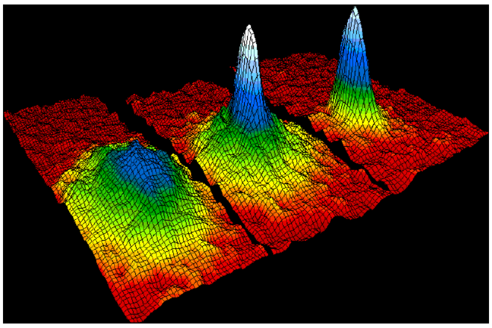

Figure 1.1: Velocity-distribution data for a gas of rubidium atoms going through threshold for BEC[7], showing all the particles occupying the ground state of energy and becoming concentrated in momentum. Left: distribution just below threshold. Center: at threshold. Right: further above threshold after almost all particles have condensed into the ground state.

Superfluidity in liquid helium was discovered in 1937[8, 9]. It is a phase where the matter behaves like a fluid with zero viscosity. This allows the liquid to apparently disregard the force of gravity and surface tension, and climb the sides of the container or seep through narrow capillaries, slits or small holes. It was given a theoretical underpinning by Landau in 1946[10] who reasoned it is a result of a BEC-like phase. However these species have quite strong inter-particle interactions. As a result, in Helium-4 only about 10% of the particles occupy the ground BEC state. This is known as quantum depletion[11, 12, 13] and does not fit in with Bose and Einstein's original model. Superfluids and superconductors are not usually considered true BECs.

1.3 Atomic BEC

The first unambiguous Bose-Einstein condensates were atomic condensates. They are dilute and therefore weakly interacting unlike the superfluid helium and superconductive metals. Merely increasing the number density of an atomic gas will cause molecules to form long before the BEC threshold is reached. Therefore it is necessary to reach low temperatures so as not to increase the number density. Advances in laser cooling in the 1980s and 1990s made this possible. Finally in 1995 the first recognised BEC was formed as described in Anderson et al[1]. The group used Rubidium-87 atoms in magneto-optical traps and then used laser cooling and evaporative cooling until 170 nK when the condensate appeared. Switching off the traps and allowing the gas cloud to expand is a method of measuring the velocity distribution of that atom cloud. Figure 1.2 shows the macroscopic occupation of the ground state in velocity (momentum) space which is taken from the original paper by Anderson et al. The peak appears at zero-momentum so this shows the atom cloud has undergone BEC.

Further developments were BECs made from other species. Davis et al[14] created a BEC in a gas of sodium atoms. Another early example is Bradley et al[15] who created a BEC from lithium. A BEC of spin-polarised hydrogen is described in Fried et al[16] which had the advantage of achieving an order of magnitude higher number density but had poor laser-atom interactions because the required wavelength is 105nm. BEC with potassium atoms was achieved by Modugno et at[17] by sympathetic cooling, essentially mixing potassium and rubidium in thermal equilibrium. Cooling the latter as normal then allows collisions to bring down the temperature of the potassium as well. A theoretical underpinning of BECs in gases trapped in harmonic potentials was reviewed by Dalfovo et al[10] and the Gross-Pitaevskii equation is derived in the paper.

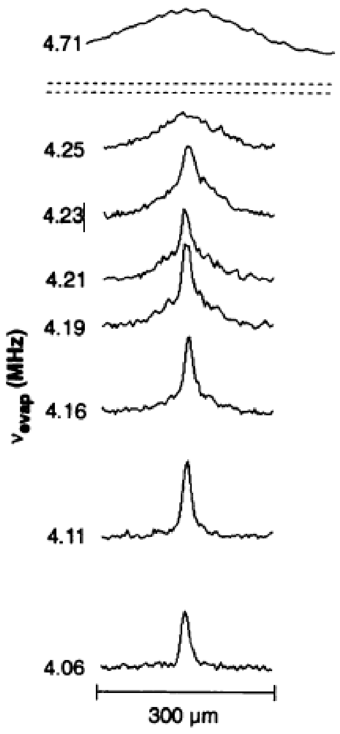

Figure 1.2: Sections taken through the velocity distribution of successive atom clouds. ν_{evap} is the frequency of final evaporative cooling stage where lower means a lower temperature and higher phase-space density. The 300 μ m bar is the size calibration. With the top diagram we see a thermal cloud distribution, while the bottom diagram shows almost all atoms to be in the ground state with near-zero velocity, indicating BEC. Compare this with figure 1.1. Data taken from Anderson et al.[1]

1.3.1 Gross-Pitaevskii Equation

The equation of motion for the wavefunction $\psi = \psi(\vec{r}, t)$ describing the condensed part of a non-dissipative Bose gas is:

$$\tag{1.5}$$

$$i\hbar\frac{\partial\psi}{\partial t} = \left(-\frac{\hbar^2}{2m}\nabla^2 + V(\vec{r}) + g|\psi|^2\right)\psi \tag{1.6}$$

where V is the potential, g is the interaction strength and all other symbols have their usual meanings. This equation can be derived from a variational approach, by assuming a point-interaction of particles and fixing the number of particles. The Lagrangian multiplier for number turns out to be the chemical potential μ. Minimizing this Lagrangian results in an expression for ψ which is the Gross-Pitaevskii equation. From it, it is possible to obtain solutions of propagating sound waves or vortices in the BEC.

The topic of vortices in BECs is reviewed by Fetter and Svidzinsky[18]. Solutions to the Gross-Pitaevskii equation are found which describe vortices and comparisons with experimental data are found to be in agreement.

Phase fluctuations in a BEC in a quasi-1D system were observed by Dettmer et al[19]. They used it to investigate the coherence properties with the idea to potentially use Rb-87 BECs for matter wave interferometry using the property of atom laser beams. Evidence for pronounced phase fluctuations is found in certain conditions in line with theory.

1.4 Exciton-Polariton Condensation

Excitons are optically-active dipoles that result from the Coulomb interaction between an electron in the conduction band and a hole in the valence band[20]. Polaritons are a wide class of quasiparticles where electromagnetic fields couple to another excitation. Exciton-polaritons therefore are quasiparticles arising from the strong coupling of excitons to photons, and being made up of two fermions and a boson, are bosons themselves. They can be produced in a microcavity to confine the photons and give rise to an effective mass and harmonic potential[21].

A dissipative BEC system such as certain exciton-polariton condensates is one where there is a dynamic equilibrium between bosons entering and leaving. It is described with the grand canonical ensemble, in contrast to a static BEC where an unchanged number of particles make up the condensate throughout the entire experiment, described by the canonical ensemble. It requires a modification to the Gross-Pitaevskii equation to take into account pumping, loss and saturation.

$$i\hbar\frac{\partial\psi}{\partial t} = \left[-\frac{\hbar^2}{2m}\nabla_\perp^2 + V(\vec{r}) + g|\psi|^2 + i\left(\gamma_{net} - \Gamma|\psi|^2\right)\right]\psi \tag{1.7}$$

where γ_{net} is the net influx (pump by laser minus loss through cavity) of particles and Γ is a constant controlling saturation[21].

In the last decade, a link between condensates and coherence effects in optical systems has been exploited to create exciton-polariton condensates in semiconductor microcavities. [22, 23, 24]. The typical experiment setup from Kasprzak et al[25] is shown in figure 1.3. A microcavity is made with inorganic semiconductors and two dielectric stack mirrors at resonance with excitons in quantum wells (QW). Excitons and optical modes in the strong coupling regime give rise to new eigenmodes known as microcavity polaritons. The laser pump creates the required electron-hole pairs. For a high enough laser power, the density of the polaritons exceeds the threshold density needed for Bose-Einstein condensation as shown in the bottom panel of the figure.

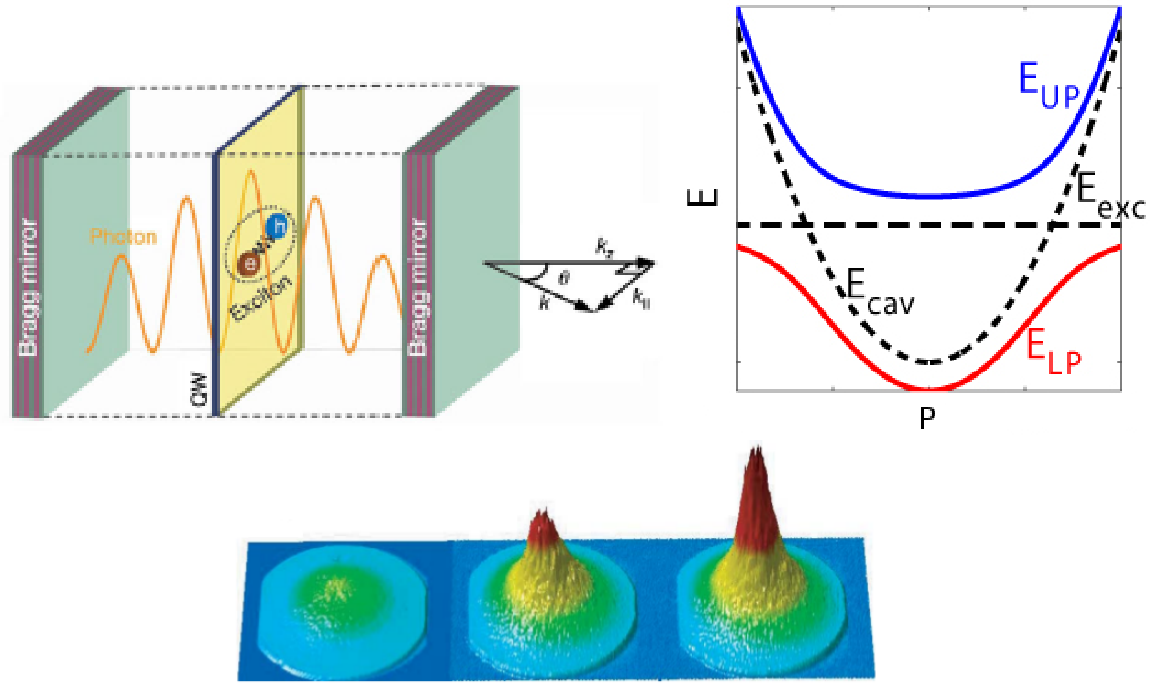

Figure 1.3: Figures from Kasprzak et al[25]. Top Left: A microcavity of two dielectric stack mirrors. Quantum wells (QW) hold optically-active dipoles where the Coulomb interaction results in excitons. Coupling of these with the optical cavity modes give rise to eigenmodes known as microcavity polaritons. Top Right: Dispersion relation curves (dashed lines) of exciton (near-straight line) and photons (parabola). Interaction between exciton and cavity photon modes gives rise to upper and lower polariton branches (solid curves) with a shape typical of the strong coupling regime. Bottom: Pseudo-3D images of the far-field emission from the microcavity. With increasing laser pump power a sharp and intense peak is formed in the center corresponding to zero momentum and the ground state. Compare with figures 1.1 and 1.2.

Kasprzak et al did not observe unambiguous evidence of thermalisation and therefore thermodynamic equilibrium, which is a necessary condition for BEC. It was found in some systems and attributed to polarition-polarition collisions within the gas[26]. Some of the earliest work on the topic is Deng et al[27] in 2002 who create the exciton-polariton experimental setup and observe a phase transition. They measure a corresponding decrease in the second-order coherence function; the emission behaves in a super-poissoninan way as would be expected from

Bose-Einstein statistics. A later paper[28] creates a Young's double-slit setup to observe the first-order coherence of emission light from the polariton condensate. They observe that the system gains coherence above the condensation threshold which is well explained by a model based on the Bose-Einstein distribution. Sun et al[29] in 2017 produced the first claimed example of unambiguous exciton-polariton BEC. They observe thermalisation of the polaritons at several different temperatures, and also observe the threshold behaviour as the sample transitions to the condensed state.

An alternative way of creating condensates is organic exciton-polariton condensation. A microcavity is made containing a thin film of TDAF[1]. As described in Daskalakis et al[30], the electrical characteristics of this organic semiconductor make it an attractive candidate for condensation. The dispersion relation is measured showing the quadratic law of a massive particle. Above threshold they observe formation of linearly polarized condensates, but because thermalisation is not demonstrated this has not been shown to be BEC according to our definition from the start of this chapter. The spatial coherence is measured and rapidly increases above threshold. Plumhof et al[31] achieve Bose-Einstein condensation with organic polaritons in a similar setup. They use a microcavity with the polymer MeLPPP as a medium and demonstrate thermalisation at room temperature and, above a critical excitation density, clear evidence of condensation in the ground state. Spatial and temporal coherence is measured with an interferometer showing an increase above condensation threshold.

1.5 Photon BEC

While blackbody photons are bosons, they are not suitable for creating BEC because lowering the temperature merely results in the photons being absorbed into the walls. The photons having zero mass means they can be created and destroyed easily and are therefore not a conserved quantity in this grand canonical ensemble.

A microcavity[32] is an optical resonator (i.e. two mirrors facing each other) which is close to or below the dimension of the wavelength of light. It results in the photons gaining an effective mass in the sense that there will be an energy cost to create them above the Planck-Einstein relation $E = h\nu$ (with h being Planck constant and ν being photon frequency). The lowest possible energy of photons is set by when the cavity has a length of a single half-wavelength. We call this the cutoff wavelength λ_0 because it is the longest possible wavelength of a photon that can exist in the cavity so it defines the ground state of the system. The curvature of the cavity mirror can be seen as a force pushing photons towards the cavity center, and so the mirror creates a harmonic potential $V(\vec{r})$ for the photons to exist in. The photons gain an effective mass m_{ph} found from the quadratic dispersion relation that they now obey.

Figure 1.4 shows a diagram of the cavity. One planar mirror is fixed opposite to a spherical mirror with radius of curvature R, the photons have angular frequency ω and wavenumber k which is made up of longitudinal and transverse wavenumber k_z and k_r respectively. The photon energy is $E = \hbar\omega = \hbar c^* k = \hbar c^* \sqrt{k_z^2 + k_r^2}$, where c^* is the speed of light in the medium rather than vacuum[2].

---

[1] 2,7-bis[9,9-di(4-methylphenyl)-fluoren-2-yl]-9,9-di(4-methylphenyl)fluorene

[2] As there is no dispersion, phase and group velocity are the same

The longitudinal wavenumber matches the boundary conditions k_z and is of the form $k_z = q\pi/L$, where q is the longitudinal mode number. The cavity length L is comparable to the wavelength. We use the paraxial approximation $k_r \ll k_z$. Simple geometric reasoning can find the expression for $L = L(r) = L_0 - r^2/2R$ using the assumption $r \ll R$. The photon energy can be shown to be:

$$E(r, k_r) = m_{ph}c^* + \frac{\hbar^2 k_r^2}{2m_{ph}} + \frac{1}{2}m_{ph}\Omega^2 r^2 \tag{1.8}$$

where effective photon mass $m_{ph} = \hbar k_z(r = 0)/c^{*2}$ and trap frequency $\Omega = c^*\sqrt{1/L_0 R}$. The conclusion is important: a short cavity will cause photons to behave like 2D massive particles having a rest-mass energy, a quadratic dispersion relation and be confined in a harmonic potential. It can further be shown that the density of states in the cavity with two degrees of freedom with an isotropic harmonic potential has a cutoff energy, below which there are no states.

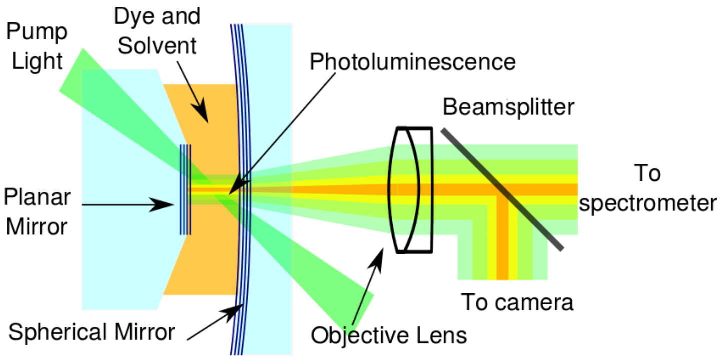

Figure 1.4: Simplified cavity schematic. A planar and spherical mirror face each other to form a cavity. Dye is dripped into the space and held in place by surface tension. The medium is incoherently pumped at the maximum angle of transmission of the dielectric mirrors.

The dye in the cavity is Rhodamine-6G. It is pumped with a high absorption at the laser wavelength 532nm and rescatters the light. As there is no phase relationship between the pump light and cavity light, we say the pumping is incoherent[21]. The photons scatter off the molecules with a timescale of about 1-1000ps depending on the cutoff wavelength and concentration; with correctly chosen parameters they can scatter many times before leaving the cavity, which has a lifetime of about 300ps. The photons are statistically likely to be emitted into cavity modes at wavelengths and intensities matching the Bose-Einstein distribution. We say that the dye in the cavity has caused the photons to become thermalised.

Reducing the temperature or increasing the number density of the photons in the microcavity (which brings the chemical potential closer to the ground state) would eventually cause macroscopic occupation of the ground state, which in our experiment is seen as a large photon population at the cutoff wavelength.

Another approach for studying the energy of the photons and deriving the potential energy imposed by the cavity mirrors is found in Nyman and Szymanska[33]. They derive a version of the Gross-Pitaevskii equation with dissipative terms from Maxwell's equations applied with the paraxial approximation and Kerr-type interactions. This equation of motion can handle an arbitrary potential and is more general than the energy equation 1.8, which can be derived from it, though we include the geometric derivation for ease of intuitive understanding. The result is equivalent to this energy equation anyway.

There are similarities between the photon BEC setup and that of a dye laser. This had led newcomers to the field to question whether photon BEC has any new physics at all, if it is just a new kind of laser. Dye lasers do not contain any thermalised photons, and their emission photons obey Poissonian statistics rather than the kind predicted by the Bose-Einstein model. Dye lasers also do not have a ground state and have weak rescatter[34][35], although this is not as strong an indication as the point about statistics it further builds up a picture of dye lasers and photon BEC involving different physics.

1.5.1 Thermalisation of Photons in Rhodamine-6G Dye

The dye in the cavity causes the photons to thermalise. The cavity is filled with optical dye. Photons are scattered several times and reach a thermalised condition matching the temperature of the dye. This takes on the order of a few picoseconds, which is much faster than the average time a photon takes to exit the cavity.

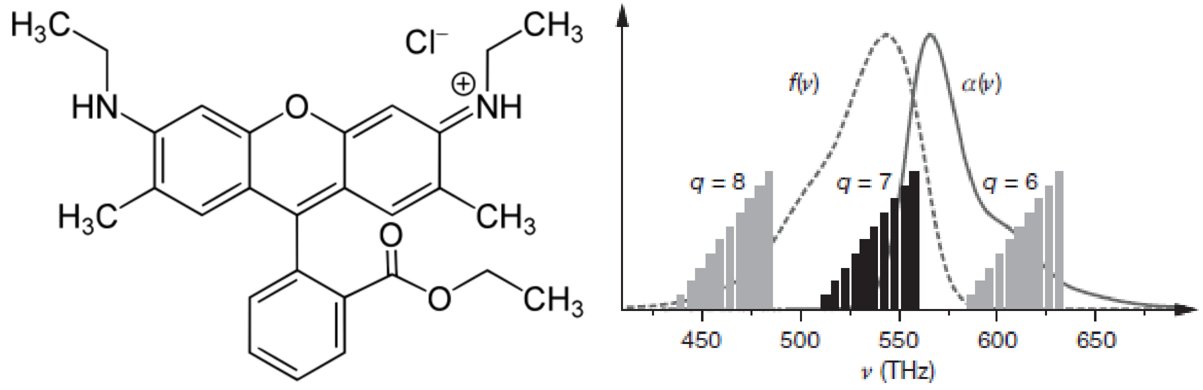

Figure 1.5: Left: Diagram of the Rhodamine-6G molecule which gives rise to the electronic and rotational-vibrational energy levels relevant to the thermalisation process. Image taken from Wikipedia. Right: Absorption $\alpha(\nu)$ and emission $f(\nu)$ spectra of Rhodamine-6G as a function of light frequency. q refers to the longitudinal mode number of the cavity and individual bars correspond to degeneracy. The length of the cavity is chosen so that the overlap in the absorption and emission spectra coincide with the photon modes, allowing them to be emitted and reabsorbed several times. Image from Klaers et al[36].

The dye absorbs light and is put into its electronic-excited state and the photons are repeatedly absorbed and re-emitted from the rotational-vibrational energy levels. The rescattering timescale ($\approx$ 300ps in our experiment) must be several times larger than the cavity lifetime, then the photons will have a high probability of being emitted with an energy distribution matching that of the dye molecules, so the photons become thermalised and when they are observed after exiting the cavity they will follow a Bose-Einstein distribution. The pump laser is pulsed to stop the triplet excited state becoming too populated, as it has a long lifetime and would be detrimental to thermalisation, the shelved molecule not being available for rescattering. Figure 1.5 shows a diagram of the Rhodamine-6G molecule which gives rise to the required electronic and rotational-vibrational energy levels. The figure also shows the emission and absorption spectra overlaid over the cavity modes. The length of the cavity is chosen so that the longitudinal mode $q = 7$ is at the overlap of the absorption and emission spectra, so that a photon existing in these modes can be emitted and reabsorbed several times in cavity lifetime.

The Kennard-Stepanov relation is essential to the thermalisation process. The relation has the form $f(\omega)/\alpha(\omega) \propto \exp\left(-\frac{\hbar\omega}{k_B T}\right)$ where $\alpha(\omega)$ and $f(\omega)$ are the absorption and emission spectral profiles respectively. The emission and absorption spectra are symmetric around the zero-phonon line, which is the wavelength at which the excitation and relaxation transitions are not phonon-assisted. The relation applies in many liquid-state dye solutions, semiconductor systems and high-pressure gases[37].

1.5.2 Creating Photon BEC

The first photon Bose-Einstein condensate was created by the group lead by Martin Weitz at Institut für Angewandte Physik at Bonn in 2010. Their papers[36][38] were both published in 2010 and show all the fundamental components of the dye-filled microcavity and thermalised photons. The paper investigates the photon thermalisation phenomenon and the conditions under which it holds and breaks down. A more detailed paper from the same group describes their experimental setup[39]. The results within a 2012 paper[40] help justify the results as well as predicting fluctuations and second order correlations. A later experiment[41] measures the second-order coherence of the emitted photons and shows they obey the expected super-Poissonian statistics.

This thermalisation of photons in a dye-filled cavity was first demonstrated by Klaers et al[38] in 2010. Figure 1.6 shows the relevant spectrum which is fitted to a theoretical curve with room temperature T=300K (although an experiment was also done where the setup was heated to T=365K). This theoretical curve is found by using the Bose-Einstein distribution and the density of states described above $\rho(\epsilon) = (\epsilon - \epsilon_0) / (\hbar\Omega)^2$. The resulting occupation number as a function of wavelength $n(\lambda)$ is

$$n(\lambda) = \frac{4\pi^2 c^2}{\Omega^2 \lambda_0^3} \left(\frac{\lambda_0}{\lambda}\right)^2 \left(\frac{\lambda_0}{\lambda} - 1\right) \frac{1}{\exp\left(\left(\left[\frac{hc}{\lambda_0}\left(\frac{\lambda_0}{\lambda} - 1\right)\right] - \mu\right)/k_B T\right) - 1} \tag{1.9}$$

where λ_0 is the cutoff wavelength corresponding to the cutoff energy, and all other symbols have their standard meanings or meanings defined earlier. Causing the thermalisation to break down is an important piece of evidence as Klaers demonstrates in figure 1.6. Cavity spectra are taken which match equation 1.9, but increasing the cavity cutoff wavelength causes the data to no longer follow the fit, indicating that thermalisation has broken down. The larger cutoff wavelength puts the cavity in the regime where photons on average leave before they are rescattered enough to become thermalised.

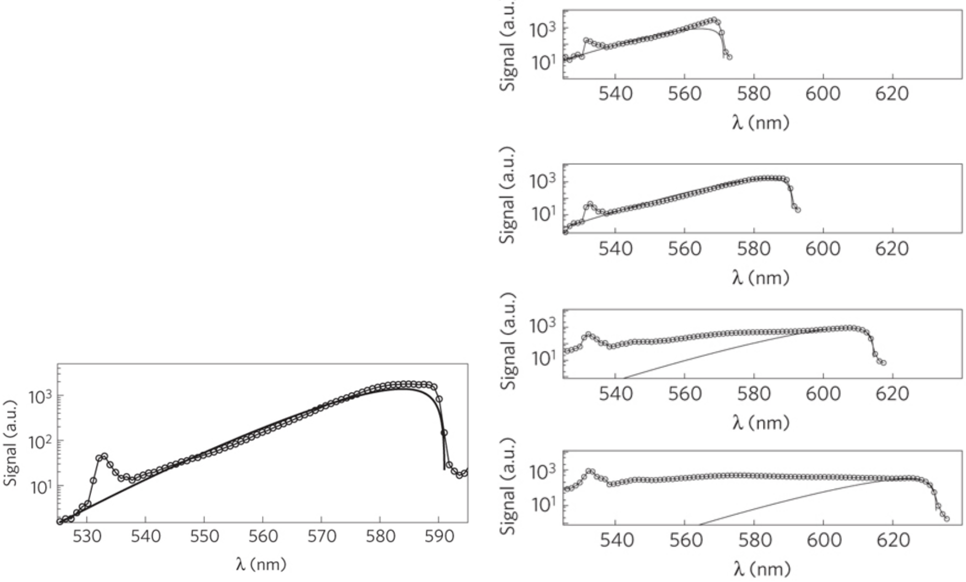

Figure 1.6: Left: The connected dots give measured spectrum of emission light from the cavity. The solid line is equation 1.9 plotted at temperature T=300K and it matches the data indicating that the cavity light is thermalised. The peak at 532 nm is the laser pump light. The cavity cutoff wavelength is 590 nm. Right: The same spectra at several different cavity lengths, showing that thermalisation breaks down as the cavity cutoff wavelength increases toward 620 nm. At these higher wavelengths the mirror reflectivity is greatly reduced and so the cavity losses are too high for thermalisation to happen. The fact that thermalisation can be broken in this way is evidence that this view is correct. Figures taken from [38]

To obtain a BEC after thermalisation it is simply required to turn up the laser pump power to increase the number density above condensation threshold. Klaers et al[36] first demonstrated this photon BEC in 2010. Figure 1.7 shows this process where lower laser powers result in the usual thermal cloud number density distribution, while above threshold a peak appears at the lowest energy mode for light, or ground state, indicating macroscopic occupation.

The threshold photon number can be calculated. Without loss of generality we set the ground state energy to be zero and set the chemical potential to vanish $\mu = 0$. We treat the ground state N_{ground} separately from the rest of the photon gas N_{th}. The total number is given by summing over population given by the density of states $\rho(\epsilon)$ and Bose-Einstein occupation number $f(\epsilon)$:

$$N = N_{ground} + N_{th} \tag{1.10}$$

$$N_{th} = \int_{0^+}^{\infty} \rho(\epsilon) f(\epsilon) d\epsilon \tag{1.11}$$

We substitute the density of states and occupancy number, and with a change of variables ($\epsilon' = \epsilon/k_B T$) get the integral to be of standard form.

$$N_{th} = \left(\frac{k_B T}{\hbar\Omega}\right)^2 \int_{0^+}^{\infty} \frac{\epsilon' d\epsilon'}{e^{\epsilon'} - 1} = \left(\frac{k_B T}{\hbar\Omega}\right)^2 \left(\frac{\pi^2}{6}\right) \tag{1.12}$$

After threshold, any new photons will occupy the ground state instead of the thermal cloud. There we can set $N_{th} \to N_C$ to obtain the critical number.

$$N_C = \left(\frac{\pi^2}{6}\right) \left(\frac{k_B T}{\hbar\Omega}\right)^2 \tag{1.13}$$

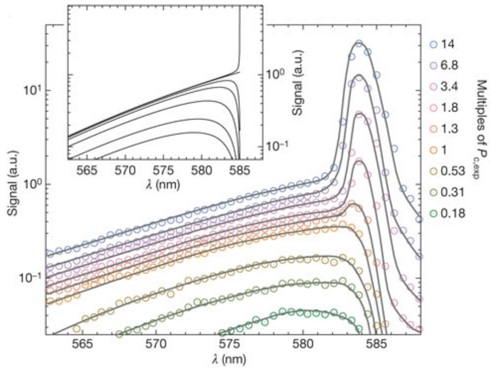

Figure 1.7: Shows the process of increasing pump power to induce Bose-Einstein condensation. The lower pump powers have the same thermal shape at T=300K as figure 1.6 while the higher powers have a pronounced peak at the cutoff wavelength indicating BEC[36]. This can be compared with figures 1.1 and 1.2 which also show a similar process of going through threshold, although they are in momentum space while this is in energy.

A later 2015 paper from the Weitz group[42] describes the time-resolved experiments. They pump the dye-filled cavity with a short pulse and observe with a streak camera. One set of data involves recording the spectrum below BEC threshold at many different times for a few cutoff wavelengths. For the slow thermalisation time regimes the spectrum is shown to deviate from the thermal spectrum at all times. For fast thermalisation time regimes the spectrum follows the thermalised fit at all times. But for medium thermalisation time we see the spectrum first not be thermalised and then at around 350ps starts to follow the thermal fit. They also take real-space images of the cavity vs time for several loss regimes. Oscillation of the light can be seen at exactly the cavity trap frequency. In the fast thermalisation time, the central region becomes brighter with time and oscillation at the edges dimmer, indicating the growth of BEC, while medium loss values show less and less BEC buildup with the oscillation staying the same brightness. The BEC builds up linearly for more than 200ps.

The Weitz group have also created a photon BEC using a solid-state sample of dye dissolved in a polymer inside a microcavity[43]. The thermalisation works the same and they achieve BEC, but the dye photobleaches in the high pump intensity within seconds so this setup is more unwieldy. The same group in a 2016 paper, Schmitt et al[44] measure the phase of a photon Bose-Einstein condensate by overlapping the cavity emission light with a stable reference laser, and measuring the resulting beat signal. They observe phase-jumps, happening when the condensate population drops to zero in a fluctuation; when the condensate reforms it has chosen a new phase to oscillate in. This is an example of spontaneous phase symmetry breaking in a driven-dissipative system. The Bonn group also published a paper [45] about accessing thermodynamic properties of the Bose-Einstein condensate. They reasoned that the internal energy U and total photon number N can be calculated using spectrometer readings $n(\lambda)$, and from there thermodynamic variables can be derived, in particular the heat capacity. They observe a lambda-peak-like structure, a cusp singularity in the specific heat capacity similar to that appearing in other BEC systems. The group in Bonn published a method to create thermalised light in lattice potentials created with thermo-optic imprinting of a dye-polymer solution. The experiment described in Dung et al[46] results in an ultrahigh-finesse cavity and achieves thermalised light and photon BEC. They also observe tunnelling between the two wells in a double-well potential system. The Bonn group has also published a paper in 2017 Damm et al[47] where they build an interferometer to measure the first-order spatial coherence of thermalised and photon BEC light. They find in the thermal cloud the coherence length is set by the de Broglie wavelength, and for BEC it extends over the entire ground state.

Our group lead by Rob Nyman at Imperial College London are the second group to have created photon BEC. We have produced a paper, Marelic and Nyman[48], about the experimental measurements taken immediately after the achievement of the BEC. It focusses on the effects of different kinds of pumping, namely inhomogeneous pumping with the pump spot not being matched to the cavity. The experimental results are described in chapter 3. Another paper produced by our group is Marelic et al[49] about the spatial and temporal coherence of the BEC as measured with an interferometer. The paper also describes multimode condensates observed in the experiment with the interferometer experiment being described in detail in chapter 4. A further paper produced by our group is Marelic, Walker and Nyman[50] about phase-space views into photon BECs. The paper revolves around a 2-dimensional spectrometer experimental setup which is used to take views into the phase-space of the system. It tests the strength of photon-photon and photon-molecule interactions, observes the effects of degradation of thermalisation in energy-momentum space, and finds that the system can be described as ergodic. The experiment is described in detail in chapter 5.

1.5.3 Theory Literature

A good summary of the theory literature on this topic can be found in Nyman and Walker[51]. As well as the theoretical work by the Klaers et al group mentioned earlier, photon BEC was also investigated by Kirton and Keeling[52] starting with a 2013 paper. They develop a simple non-equilibrium model of condensation and use it to examine the thermalisation process. They start with a hamiltonian similar to the Jaynes-Cummings hamiltonian H:

$$H = \sum_m \omega_m a_m^\dagger a_m + \sum_i \left[\frac{\Delta}{2}\sigma_i^z + \Omega \left(b_i^\dagger b_i + \sqrt{S}\sigma_i^z (b_i + b_i^\dagger) \right) \right] + g \sum_{m,i} (a_m \sigma_i^+ + a_m^\dagger \sigma_i^-) \tag{1.14}$$

where $a_m^\dagger$ and a_m are creation and annihilation operators of photons in cavity mode m. Each dye molecule is indexed by the label i and is modelled as a two-level system with the Pauli matrix σ_i (and raising/lowering operators $\sigma_i^+\sigma_i^-$) and splitting Δ between ground and excited-state levels. These levels are dressed by rovibrational states which can be thought of as phonons described by operators b_i and $b_i^\dagger$. g is the light-matter coupling strength. The symbol ω_m is the frequency of a photon in mode m, S is the Huang-Rhys parameter which refers to the strength of the electron-phonon coupling. The units are such that $\hbar = 1$, $k_B = 1$. The first term is the energy of all the photons, the second term is the energy associated with the electronic and rotational-vibrational excitation of the dye molecules, and the third term is energy associated with the interaction between photons and phonons.

To take into account loss and external pumping processes, this Hamiltonian is used to derive a density operator master equation:

$$\dot{\rho} = -i\,[H, \rho] - \sum_{i,m} \left\{ \frac{\kappa}{2}\mathcal{L}[a_m] + \frac{\Gamma_\uparrow}{2}\mathcal{L}[\sigma_i^+] + \frac{\Gamma_\downarrow}{2}\mathcal{L}[\sigma_i^-] + \frac{\Gamma(-\delta_m)}{2}\mathcal{L}[a_m^\dagger \sigma_i^-] + \frac{\Gamma(\delta_m)}{2}\mathcal{L}[a_m \sigma_i^+] \right\} \rho \tag{1.15}$$

Where the loss and pumping is described by the standard Markovian Lindblad terms $\mathcal{L}$. κ is the cavity mode decay rate, $\Gamma_\downarrow$ is the florescence rate of the dye molecules into noncavity modes, $\Gamma_\uparrow$ is the pumping rate. $\Gamma(-\delta_m)$ and $\Gamma(\delta_m)$ are the emission and absorption rates respectively into mode m, δ_m is the mode's detuning from the zero-phonon line. From this master equation is derived a semiclassical rate equation for the population of each photon mode which, after adiabatically eliminating the molecular degrees of freedom is:

$$\frac{\partial n_m}{\partial t} = -\kappa n_m + N \frac{\Gamma(-\delta_m)(n_m + 1)\tilde{\Gamma}_\uparrow - \Gamma(\delta_m) n_m \tilde{\Gamma}_\downarrow}{\tilde{\Gamma}_\uparrow + \tilde{\Gamma}_\downarrow} \tag{1.16}$$

Where N is the number of molecules, $\tilde{\Gamma}_\uparrow = \Gamma_\uparrow + \sum_m g_m \Gamma(\delta_m) n_m$ and $\tilde{\Gamma}_\downarrow = \Gamma_\downarrow + \sum_m g_m \Gamma(-\delta_m)(n_m + 1)$ which are the total pumping and decay electronic transition rates including the contributions from cavity modes (g_m is degeneracy). This model can be used to show how the Kennard-Stepanov relation leads to photon thermalisation. Kirton and Keeling obtain an expression for the steady-state photon distribution ($\partial n_m / \partial t = 0$), the population of cavity mode m is n_m and is:

$$\kappa n_m = N \frac{\Gamma(-\delta_m)(n_m + 1)\tilde{\Gamma}_\uparrow - \Gamma(\delta_m) n_m \tilde{\Gamma}_\downarrow}{\tilde{\Gamma}_\uparrow + \tilde{\Gamma}_\downarrow} \tag{1.17}$$

If we solve this equation in the equilibrium limit that all rates not involving the cavity directly are scaled to be very small so $\kappa, \Gamma_\uparrow, \Gamma_\downarrow \to 0$, then we obtain the Bose-Einstein distribution for photons:

$$\frac{n_m + 1}{n_m} = e^{\beta \delta_m} \frac{\tilde{\Gamma}_{\downarrow}}{\tilde{\Gamma}_{\uparrow}} \tag{1.18}$$

which allows us to set the chemical potential $\mu = k_B T \ \ln \tilde{\Gamma}_{\uparrow} / \tilde{\Gamma}_{\downarrow}$. Rearranging to put in the same form as equation (1.1) and using $\beta = 1/k_B T$ results in the more usual form:

$$n_m = \frac{1}{e^{(\delta_m - \mu)/k_B T} - 1} \tag{1.19}$$

A further paper by Kirton and Keeling[53] investigates breakdown of thermalisation. They use the same model as in the earlier paper to obtain a rate-equation describing the system. For relevant parameters it fits with the experimental data including the transition to condensed phase. Above a critical cavity loss rate or below a temperature, a crossover occurs and the system behaves in manner more typical for a laser. The paper shows how the model can reproduce experimental results such as the thermalisation and breakdown thereof.

A later paper[54] by the same people studies the effects of pump-spot size and location on the photon BEC. The group reproduces our results from the Marelic/Nyman paper[48] of the effect of small pump spots on the thermalisation. They find results for the relationship between spatial equilibrium and thermalisation in the condensate. Our lab also provided the absorption and emission data of Rhodamine 6G dye used in the paper[55].

A paper by Kopylov et al[56] uses a full master equation approach of a two-mode system to analyse photon BEC. They are able to model photon condensation but not thermalisation. A paper by de Leeuw et al[57] investigates the effect of finite-lifetimes in dissipative systems like photon BEC on the first-order correlation function. They conclude that the finite lifetime has no effect on the spatial correlation but an important effect on the temporal correlation. They also consider a non-BEC photon system (thermal cloud) and demonstrate that both spatial and temporal first-order correlation functions are decreased. Another paper by the same group (van der Wurff et al[58]) investigates how interactions between particles in a BEC affect the number fluctuations. They find an expression for the second-order zero-delay number correlation function $g^{(2)}(0)$ for different interaction strengths and condensate fractions. The theory is compared to experimental results of photon BEC from the previously-mentioned Bonn group 2014 paper on fluctuations[41]. The van der Wurff paper notes that the interaction strength depends on dye concentration and detuning between cavity resonance and ZPL. The paper then goes on to discuss possible origins of such an interaction force. They conclude thermal lensing and Kerr effect photon-photon interactions are not the cause. They form a hypothesis of photon-photon scattering mediated by dye-molecules modelled as a two-level system which is a function of dye concentration and detuning. They obtain a theoretical value of $\widetilde{g}$ which is small compared to experiment but they say their model is a simplification of the dye rovibrational levels and thus there is significant uncertainty.

The same theory group, de Leeuw et al[59], also produced a paper describing the dynamics of the photon gas using the Schwinger-Keldysh formalism which is commonly used in the quantum optics community. That approach can simultaneously treat coherent and incoherent effects; in particular it enables the description of the complete time evolution of photons including the relaxation towards equilibrium. They find the finite lifetime of photons can be captured in a single parameter (they call α) in their model which depends on the intensity of the pumping laser. There are further papers by the Utrecht group on the dissipation[60] and phase diffusion[61] in a photon BEC, where an interference experiment is proposed to observe the effects experimentally.

Henk Stoof's group[62] also constructed a model of photon BEC in nanofabricated semiconductor microcavities which could potentially be a better way to create photon BEC. Fani and Naderi[63] also propose a new rather difficult and complicated experimental setup: a hybrid optomechanical microcavity composed of a two-level atomic ensemble and a membrane oscillator enclosed in an optical cavity.

There are several other theory papers examining photon BEC. Some describe it using the hierarchical maximum entropy principle[64][65], the Schwinger-Keldysh formalism[59] and Dicke states and Mott-Hubbard physics[66]

1.6 Conclusion

The physics of Bose-Einstein condensation has a history going back to the early 20th century and advances in laser cooling of atoms allowed the first creation of the state in 1995. Condensation is also possible in photons which was achieved in 2010 and again by our group in 2014. Several theoretical models have been created to describe and analyse the photon BEC phenomenon.

Chapter 2

Experimental Setup for Creation of BEC

2.1 General Overview

This chapter is about the experimental setup for creating photon Bose-Einstein condensation. Throughout my PhD study the laboratory has been built up into five or six different experiments. The setup can broadly be separated into a few components: pumping, cavity, imaging, stabilisation and measurement (including camera, spectrometer, interferometer and momentum-resolved spectrometer). The laser emits a beam which is chopped by an acousto-optic modulator (AOM). The beam enters the cavity which is filled with Rhodamine-6G dye. Light leaking out of the mirrors is collected and focussed onto a camera, spectrometer and any other measuring equipment.

2.1.1 Acousto-Optic Modulator

An AOM is used to chop the laser beam to create pulses, and to control the transmission of laser light (see chapter 6). The AOM requires plane waves of light, so a set of lenses is used to focus the laser, at the focus the wavefronts of a laser beam are planar.

A voltage-controlled oscillator was built by the electronics workshop which outputs a radio-frequency (RF) voltage signal at 110 MHz. There is an RF switch controlled by transistor-transistor logic (TTL). This signal is amplified by a 20 dB amplifier, the output of which is sent to the AOM. This signal drives a piezo-electric crystal which sets up a grating pattern in the AOM crystal which makes the laser light diffract. Two beam-blockers are set up to block all except one first-order diffracted beam. Another way to view this is that the piezo emits phonons which interact coherently with the photons, and impart them some momentum which results in them diffracting.

The TTL switch controller allows this setup to block or allow laser light through. This can chop the laser beam into pulses as the RF switch can change state in about 100 ns. Changing the amplitude of the RF signal changes the amount of diffraction and therefore changes the transmission, which can be used to control the intensity of laser light as in figure 2.1. An increase in the amplitude increases the transmission, presumably because the light is diffracted more efficiently, but after a point the transmission efficiency drops likely because more light is diffracted into higher orders.

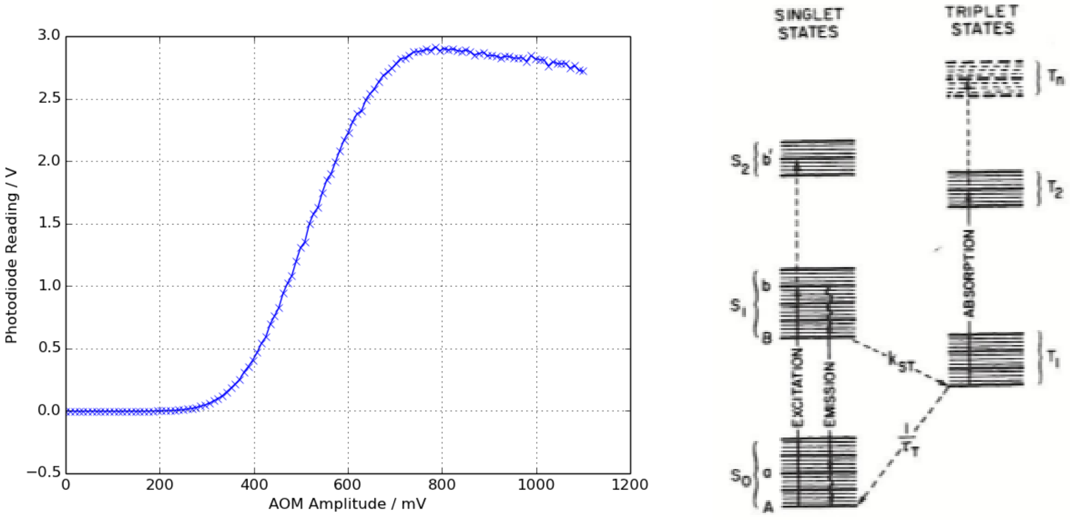

Figure 2.1: Left: Laser power transmitted through AOM vs RF amplitude voltage. Varying the RF amplitude controls the transmission. Transmission increases with amplitude until a point around 800 mV after which it drops due to more light being diffracted into higher orders. Right: Schematic energy level diagram for the Rhodamine-6G dye molecule. The horizontal lines represent rotational-vibrational sublevels of the electronic states. The first triplet state is long-lived which is why we use the AOM to chop the light and give it time to deexcite back to the ground state.

2.1.2 Cavity

The cavity is made up of a large spherical mirror and small planar mirror. The planar mirror was ground down to a circle of diameter 1mm by a manufacturer Ultrafast Innovations. The mirror is mounted on an optical flat as shown in figure 2.3. Rhodamine-6G dye[34] is dissolved in Ethylene Glycol and dropped in between the mirrors, held by surface tension. Figure 2.1 shows a schematic of the energy levels of the molecule, the laser pumps electrons from the ground state to the first excited singlet state, with a small probability the electrons may also be excited to the triplet state. A cavity schematic is shown in figure 2.2. Because the high-reflectivity cavity mirrors are dielectric stacks, there exists an angle of maximum transmission where about 70% of the light reaches into the cavity. Knowing this angle is essential for designing the optical assembly. Rob Nyman mounted the mirror on a rotating stage and scanned through the angles with a laser and power meter, which yielded the angle for maximum transmission at horizontal polarization to be 61.5 degrees. The angle of incidence in air can then be converted with Snell's law to an angle in the mounting glass; it is 37 degrees. A ray tracing diagram showing this is in figure 2.3. There are four glass prisms glued to the optical flat, two of which provide a path for light to be incident on the mirror. This ensures that the laser beam enters at approximately normal incidence and helps with aligning particularly due to the polarization effects.

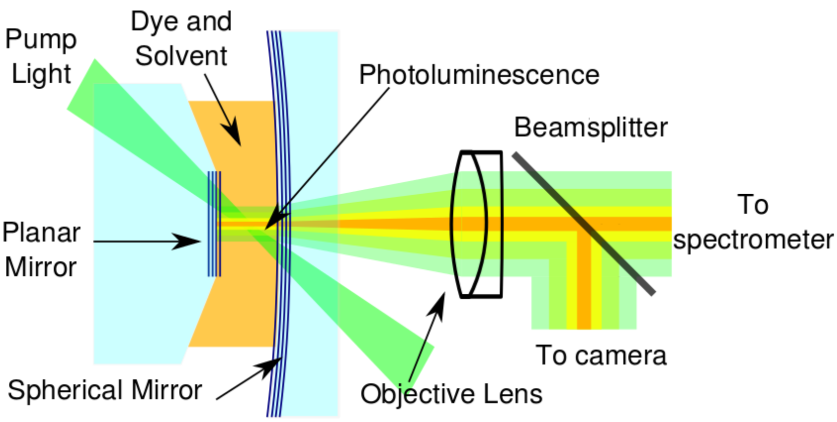

Figure 2.2: Schematic diagram of cavity. Rhodamine-6G dye dissolved in Ethylene Glycol is held by surface tension between two mirrors. Pump light enters via the angle of maximum transmission of the dielectric-stack mirrors. Cavity emission light is collected by an objective lens and sent to measuring equipment.

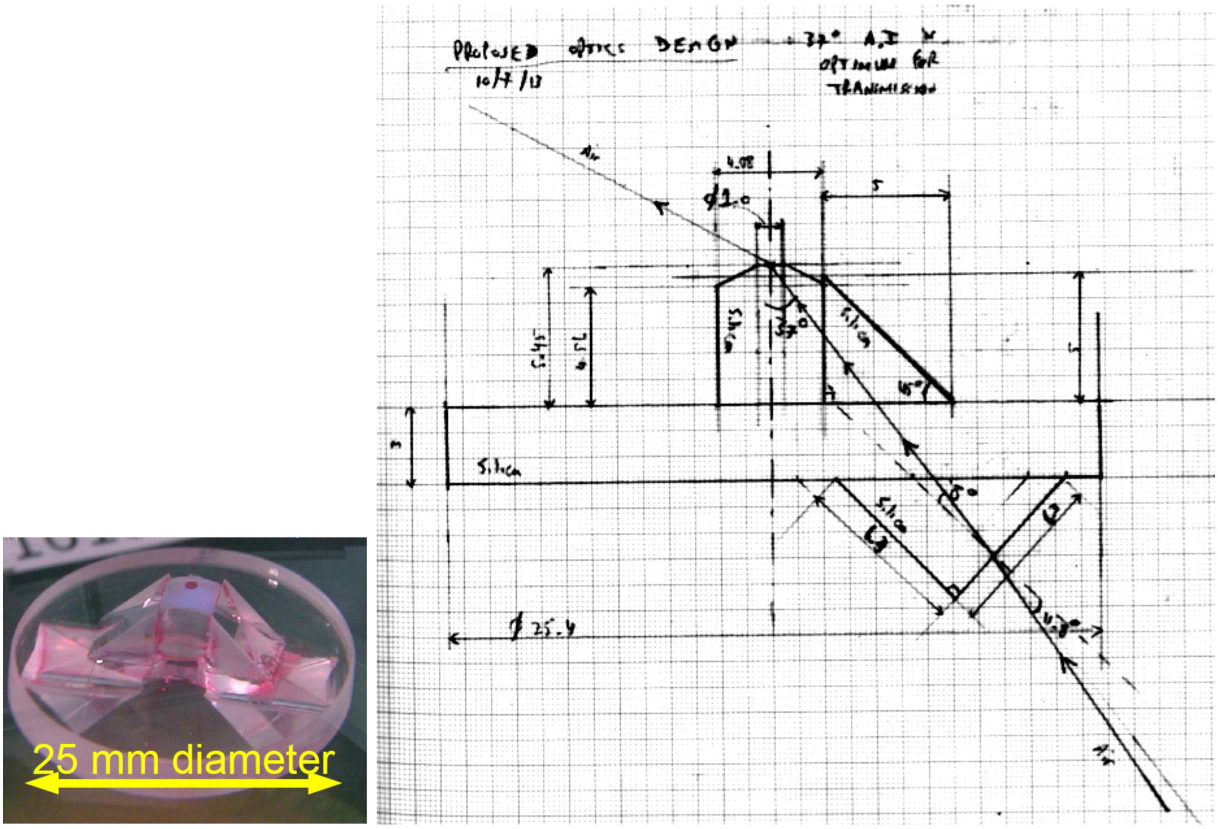

Figure 2.3: Left: Optical assembly for pumping cavity at a transmission-maximum angle for mirrors. Four glass prisms are glued onto an optical flat, as well as a glass platform with the high-reflectivity mirror mounted on top. Assembled by Melvyn Patmore. Right: Ray tracing diagram of the planar mirror mounting, involving a glass slide, a small glass platform and two glass prisms. Diagram shows a 37° incidence on the back surface.

2.1.3 Pumping and Alignment

The optical setup is shown in figure 2.4. We used four pathways (which do not necessarily exist at the same time) for the 532 nm laser light. The beam line in use is chosen with flip-mount mirrors. The first beamline is incident on the back of the planar mirror. It is reflected normally from both mirrors, this is used to align them parallel to each other. A TEM00 mode appears via coherent pumping when the two mirrors are parallel and is visible on camera. Note that the mode is only visible when the cavity is exactly resonant with 532 nm, for this reason we scan the piezo driver with a function generator to oscillate the cavity length.

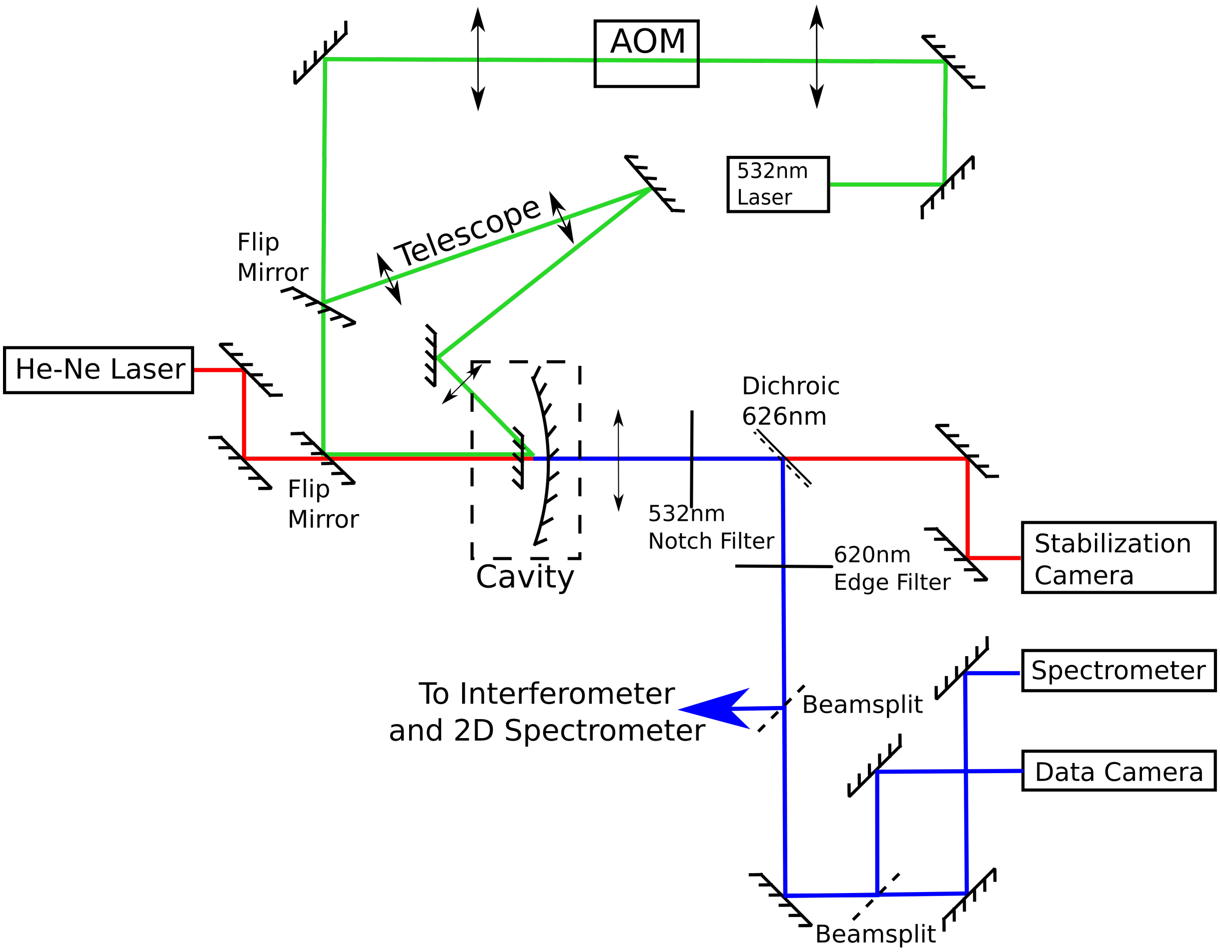

Figure 2.4: Setup for the main cavity when experiment is running. A beam of photons (shown in green) comes from the laser and is chopped by an AOM, the beam is expanded by a telescope and enters the cavity at an angle. The pump light can also enter on-axis to help with aligning the cavity. The He-Ne cavity stabilization beam is shown in red. The cavity emission light shown in blue is sent to a camera, spectrometer and other experiments.

The second beamline (henceforth called the pumping beamline) guides the laser to be focussed into the cavity at an angle of 61.5 degrees internal through prisms on the back of the mirror assembly. A telescope in the pump beamline is used to expand the beam before the lens and so achieve a smaller focal spot. To help align the cavity pumping, a third beamline is used which goes in reverse of the previously-mentioned pump beamline. It goes around the back of the experiment and enters the cavity through the large spherical mirror which has a much larger diameter of 12.5 mm. The mirrors are adjusted to walk the beam until it emerges from the back of the small planar mirror. Then the relevant flip-mirror is flipped to switch back to the pumping beamline, and it should be close-to perfectly aligned, requiring only angle-of-incidence changes to reach maximum transmission. These beamlines used for aligning are shown in figure 2.5.

A fourth beamline misses the cavity entirely and goes down the imaging line. This beam is used for calibrating and aligning various instruments, especially the energy-momentum spectrometer (see chapter 5). There is also a He-Ne 633nm laser incident on-axis on the back of the planar cavity mirror without being focussed. This is used for stabilizing the cavity length. (See section 2.5)

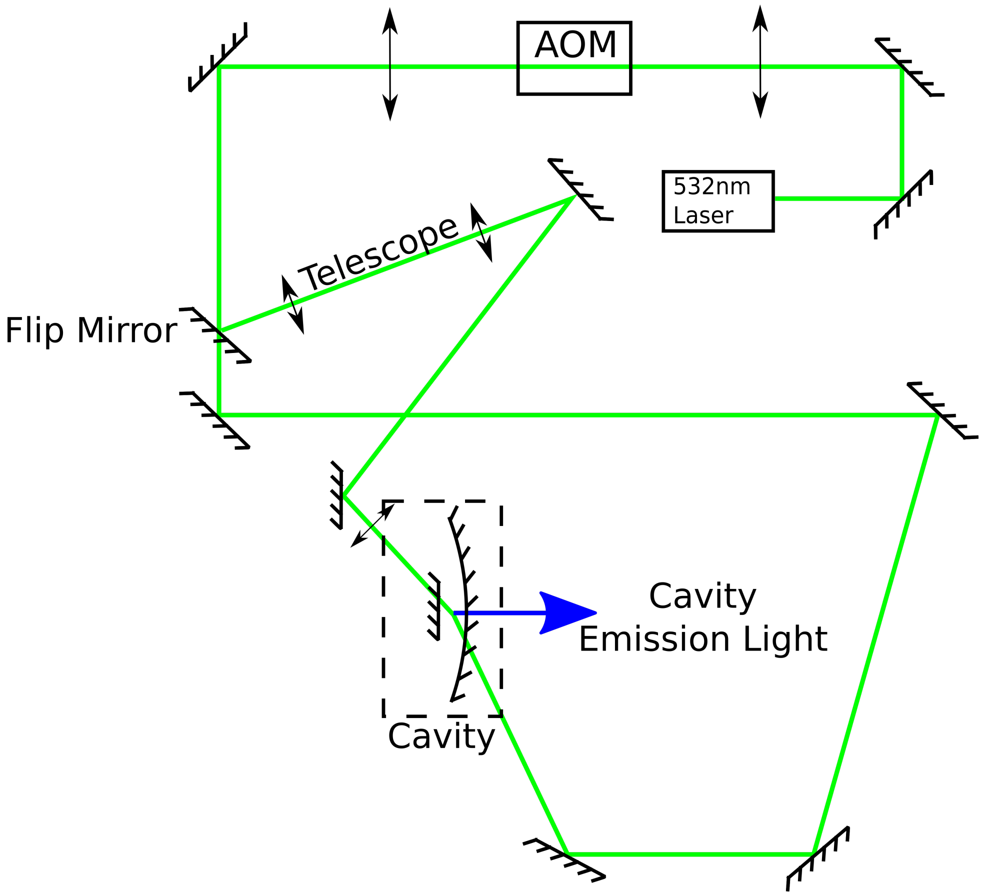

Figure 2.5: Experimental setup for aligning the cavity and pump beam. Two beamliness shown: off-axis pumping beamline and reverse pumping beamline. Beamline in use selected by flip mirrors. The larger surface of the spherical mirror makes it easier to align the pump beam to enter the cavity at the correct angle.

2.1.4 Optomechanics

A Computer-Aided Design diagram drawn by Rob Nyman of the optomechanics of the cavity is shown in figure 2.6. The spherical mirror is mounted fixed while the planar mirror is mounted on a translation stage. It has five degrees of freedom to move, including that the micrometer controlling the length of the cavity is also connected to a piezo-electric actuator which can be controlled by a computer or a function generator to change the cavity length on the scale of a few nanometers.

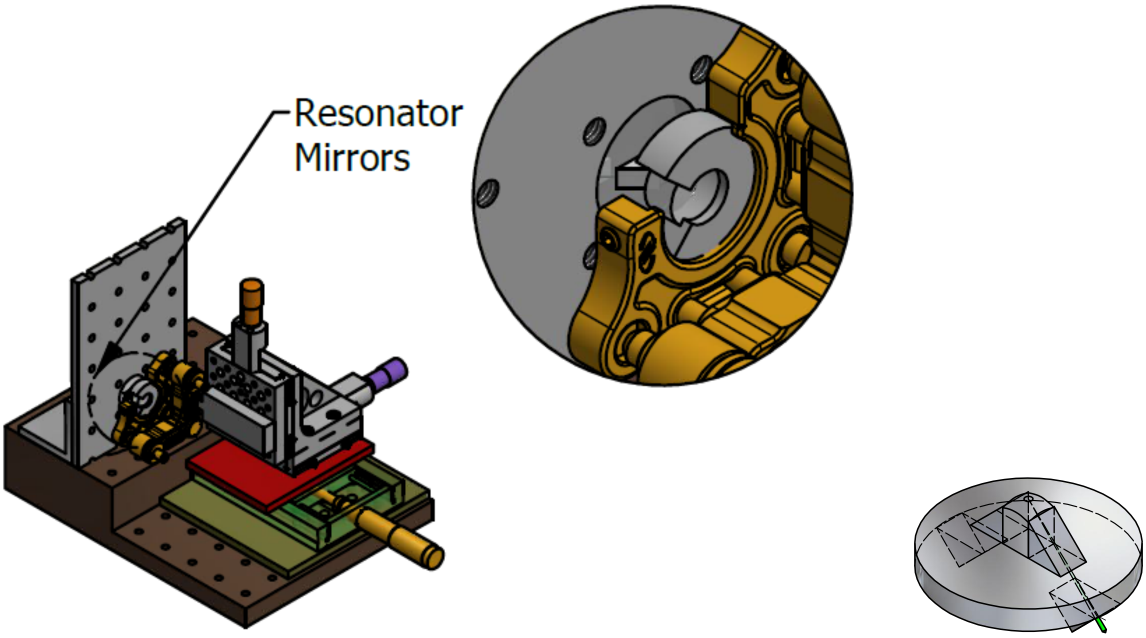

Figure 2.6: Diagram of optomechanics of the cavity. A three-way translation stage holds the 1mm diameter planar mirror on a two-angle mirror mount. The other cavity mirror is spherical 12.5mm diameter and is fixed. Left: Entire optomechanics. Center: Close-up of cavity. Right: Planar mirror assembly, with green line showing pump laser.

2.1.5 Imaging

Down-beam from the cavity there is an achromatic doublet acting as an objective lens. The imaging is an afocal system with the image formed infinitely far away. A notch filter absorbs at 532 nm to block the pump. A dichroic filter (cutoff at 626nm) separates the He-Ne 633 nm light from the photoluminescence light. A beamsplitter sends part of the light to the Point Grey Chameleon camera and Avantes spectrometer used for taking data and debugging, with the rest of the light going to the other specialised experimental measurement optics: the interferometer and energy-momentum spectrometer.

To line up the imaging system we add dye to the shortened cavity and place the objective lens, then we direct the beam to form an image as far away as possible. The image is first formed on paper held by hand reasonably close, then the objective lens distance is carefully adjusted to gradually move the image further and further away. This is a delicate task requiring two people. The image ends on the door of the lab about 8 metres away, much larger than the focal length. Then we direct this afocal image to the camera. We move the camera lens until the outline of the planar mirror is sharply in focus on camera. The size of this planar mirror outline, along with knowledge of the size of the camera pixels, allow us to find the magnification of this imaging system. As we use a 50 mm focal length objective lens with a 200 mm camera lens, the theoretical magnification is 4 and we find a value of about 3.9 ± 0.2 in practice. The spectrometer is similarly aligned by observing the dye fluorescence spectrum from the cavity.

2.2 Characterising Equipment and Materials

2.2.1 Cavity Alignment and Longitudinal Modes

An optical cavity will have a high transmission at certain wavelengths. This condition is known as resonance. Filling the cavity with dye results in a wide spectrum of wavelengths being emitted. Observing the light emitted from one cavity mirror shows these resonance peaks and changing the cavity length by varying the voltage to the piezoelectric driver changes the position of modes. Figure 2.7 shows four different spectra of cavity light.

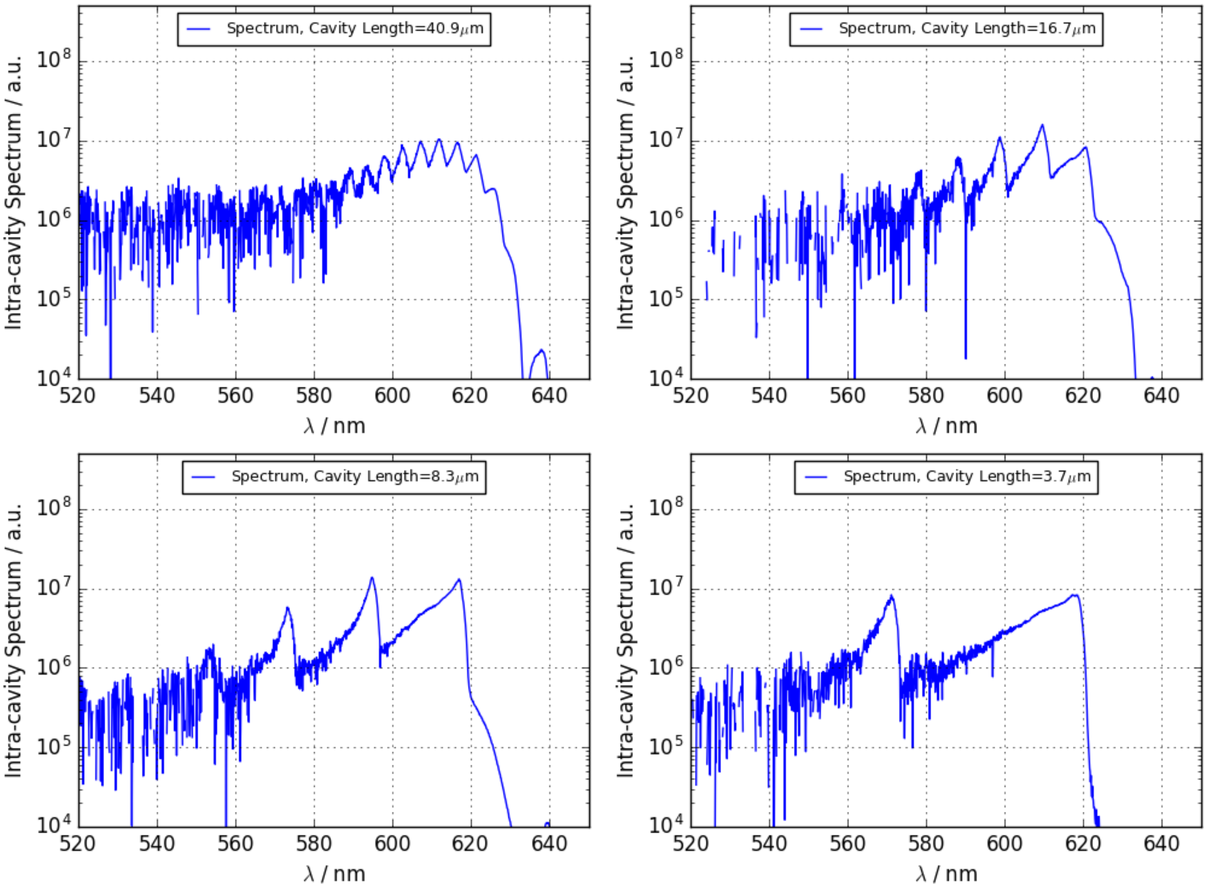

Figure 2.7: Spectrometer readings at four different cavity lengths. Reducing the cavity length increases the distance between successive peaks (also known as the free spectral range) and increases the width of the Bose-Einstein distribution as a wider range of transverse modes become supported.

A formula (Equation (2.3)) for calculating the mode number q of a longitudinal cavity mode a can be found by considering these resonances. Resonance occurs when the cavity is an integer number of half-wavelengths long. The longest wave and lowest mode-number that is resonant with the cavity is when a single half-wavelength $\lambda_a/2$ fits into a cavity of length L. We consider a mode number and also the mode number below that

$$\frac{\lambda_a}{2} q = L \tag{2.1}$$

$$\frac{\lambda_{a+1}}{2}(q-1) = L \tag{2.2}$$

We eliminate the variable L. The resulting formula is useful for finding the mode number of a peak just from one spectrometer data set. The spectrum peaks do not go all the way down to the first mode number because of the limited wavelength range of the mirror, so we cannot simply count the peaks.

$$q = \left(1 - \frac{\lambda_a}{\lambda_{a+1}}\right)^{-1} \tag{2.3}$$

2.2.2 Ringdown Measurement of Mirror Reflectivity

The quality of the cavity mirrors was tested by measuring the response of the cavity when the driving light is suddenly extinguished, also known as the cavity ringdown. Light in the cavity will bounce between the two mirrors (which have reflectivities of R_1 and R_2), being transmitted, absorbed or scattered out at each reflection. We derive an expression for the time evolution of light intensity in a cavity of length L immediately after the driving light has been extinguished. Consider the change in light intensity δI and time δt after one round trip

$$\delta I = I_{final} - I_{initial} \tag{2.4}$$

$$= I\left(R_1 R_2 - 1\right) \tag{2.5}$$

$$\delta t = 2L/c \tag{2.6}$$

where I is light intensity in cavity, c is the speed of light between the cavity mirrors (in air). In the limit of timescales much longer than δt, the fraction $\delta I/\delta t$ becomes the derivative dI/dt which can be solved

$$\frac{\delta I}{\delta t} \approx \frac{dI}{dt} = -\frac{c}{2L}\left(1 - R_1 R_2\right) I \tag{2.7}$$

$$I(t) = I(0) e^{-t/\tau_c} \tag{2.8}$$

$$\tau_c = \frac{2L}{c} \frac{1}{1 - R_1 R_2} \tag{2.9}$$

The time constant τ_c can be understood as the average lifetime of a photon inside the cavity, alternatively as the time taken for a photon round trip multiplied by the average number of round trips.

The optical setup is shown in figure 2.8. It is similar to, though simpler than, the main experimental setup. The 532nm laser shines onto the back surface of the mirror which excites the TEM00 cavity mode. The AOM is used for switching the light and a photodiode used for measuring the intensity. We measure the time constant τ_c verses many L cavity lengths. Plotting these values on a graph and fitting to a straight line results in the gradient which is equal to $\frac{2}{c}/\left(1-R_1R_2\right)$. From there we can check the reflectivity of the mirrors at the laser wavelength 532 nm which will give an indication of their quality at 590 nm for thermalising light.

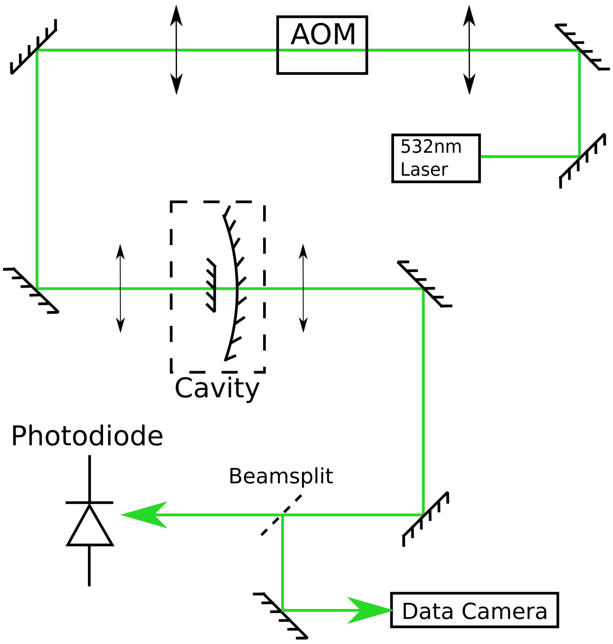

Figure 2.8: Optical setup of the ringdown measurement experiment. The laser passes through an AOM and is focussed on the cavity. The cavity emission light is sent through a beamsplitter with one half going to a photodiode and the other half to a camera.

Schmitt Trigger

A Schmitt trigger is a circuit used for the ringdown measurement. It holds the output at TTL false (0) until an input goes above a threshold. Then the output becomes TTL true (1) for a period of time, before reverting to false. For the ringdown measurement, the Schmitt trigger output controls the AOM transmission and the input is taken from the photodiode. The order of events would go as follows: the laser would pump the cavity full of light until the photodiode reading goes above the threshold, then the schmitt trigger would use the AOM to switch off the laser light for a period of time. The decay of cavity light could be observed on an oscilloscope. The length of the cavity is scanned by driving the piezo length controller to guarantee that the laser pump light will coherently couple to a cavity mode.

The circuit diagram is on figure 2.9. It is made up of a comparator which outputs a TTL true signal when the voltage difference between the input terminals ($+IN$ and $-IN$) is above zero. There is a low-pass filter to filter out noise before $+IN$ and a variable voltage divider before $-IN$ to allow the comparison level to be chosen. The output of the comparator Q_{out} and its negation $\overline{Q_{out}}$ go to an AND gate which leads to the latch pin that resets the output when high.

The negated output is delayed by a resistor-capacitor (RC) circuit which means the comparator will be reset in a timescale set by the RC circuit. However this setup was found to be unstable, flipping on and off in an unexplained way, so afterwards there is a flip-flop component with its own RC circuit that implements the latching again. It holds the signal for a time set by the RC time constant and then resets it. Figure 2.10 shows an example Schmitt trigger run with no averaging.

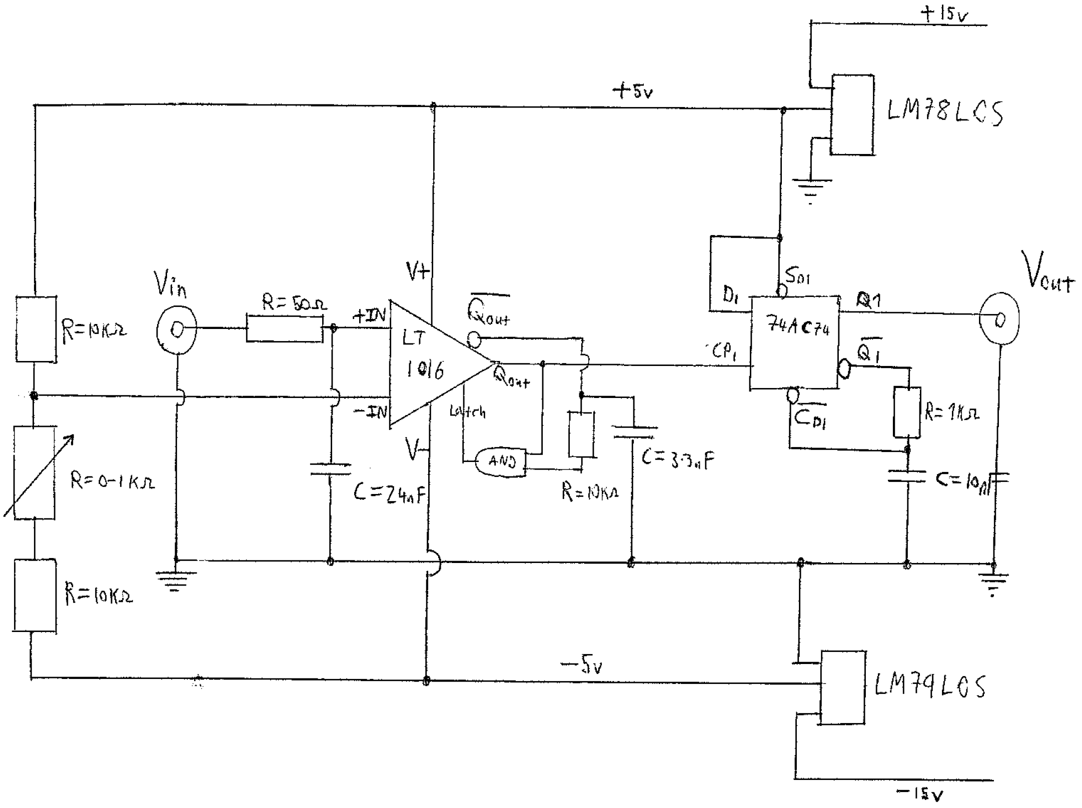

Figure 2.9: Circuit diagram of Schmitt trigger. Voltage regulators LM78LO5/LM79LO5 step down the power supply voltage to ±5V. The comparator component LT1016 uses a threshold voltage produced by a variable voltage divider. The flip-flop component 74AC74 is used as a latch to keep the output high for a period of time before resetting.

In this way the ringdown can be seen on the oscilloscope in real time and changing the cavity length and other parameters immediately alters the results. As before when aligning the cavity mirrors, the cavity emits enough light only when it is resonant with 532 nm, for this reason we scan the piezo driver with a function generator to move the cavity length back and forth quickly.

We use an analogue avalanche photodetector (APD) of make/model Analogue Modules 712A-4, chosen because of its desirable combination of speed and sensitivity. Data from the photodiode is acquired using an oscilloscope and averaged many times. The data is fitted to an exponential function to extract the time constant. The time constant is found for many different cavity lengths, which can be plotted on a graph to find the mirror reflectivities using equation (2.9).

A typical result is shown on figure 2.11 with the conclusion that the spherical mirrors are indeed of a high enough quality but that the planar mirrors may not be, their quality being at around the lower limit of the acceptable value. Note that this was all done at 532nm while the photon BEC experiment takes place at around 580nm, so this experiment does not confirm or deny that the mirrors do not have a high enough reflectivity. We decided to go ahead and build the experiment anyway despite these inconclusive tests.

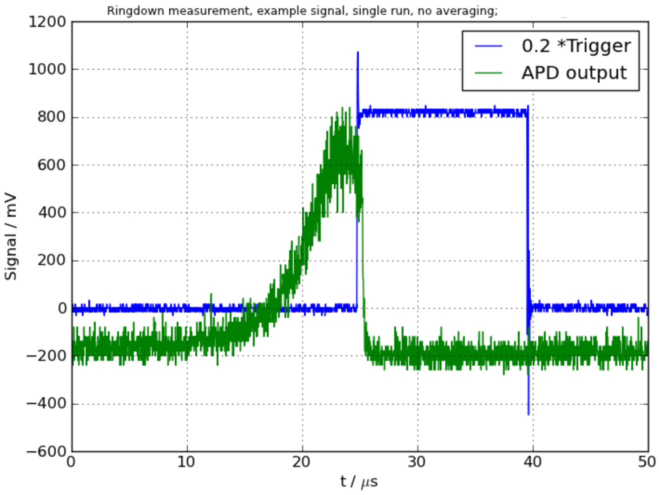

Figure 2.10: Example Schmitt trigger run. Green line is the cavity light measured by the APD, blue line is Schmitt trigger output and AOM RF switch controlling transmission. The plot shows how when the cavity light goes above a threshold, the Schmitt trigger output goes high for 15 μs and the cavity light drops to zero. This drop has the cavity ringdown shape depending on the length and mirror reflectivities.

2.3 Dye Properties

2.3.1 Absorption Spectrum of Dye

Using a spectrophotometer we measured the absorption spectrum of the dye A_λ, in order to infer the absorption cross section. The value does not seem to be in the literature at the wavelengths we needed (around 590nm) so we measured it. It should be noted there is an important systematic error which is that the spectrophotometer uses just one monochromator. It should be using two monochromators, one for the dye pumping and the second to cut out all the light of different wavelength from the dye fluorescence. This results in the largest absorptions being underestimates of the true cross section (but only in unimportant wavelength ranges). Several concentrations of dye were measured and the results merged together depending on which concentration made best use of the dynamic range of the detector. The cross section σ is calculated from the absorbance data A_λ[55].

$$n = kN_A \tag{2.10}$$

$$\sigma(\lambda) = \frac{A_\lambda}{nl} \tag{2.11}$$

where n is the number density, k is the concentration of the dye, N_A is Avogadro's number and l is the thickness of the cuvette holding the dye. Different concentrations are used because of saturation of the detector by high fluorescence outputs at certain wavelengths. Figure 2.12 shows the cross section plot and fit. We can work out the scattering timescale of photons τ_s using equation (2.12), essentially the mean free path divided by the speed of light in the medium.

$$\tau_s = \frac{1}{c^* n\sigma(\lambda)} \tag{2.12}$$

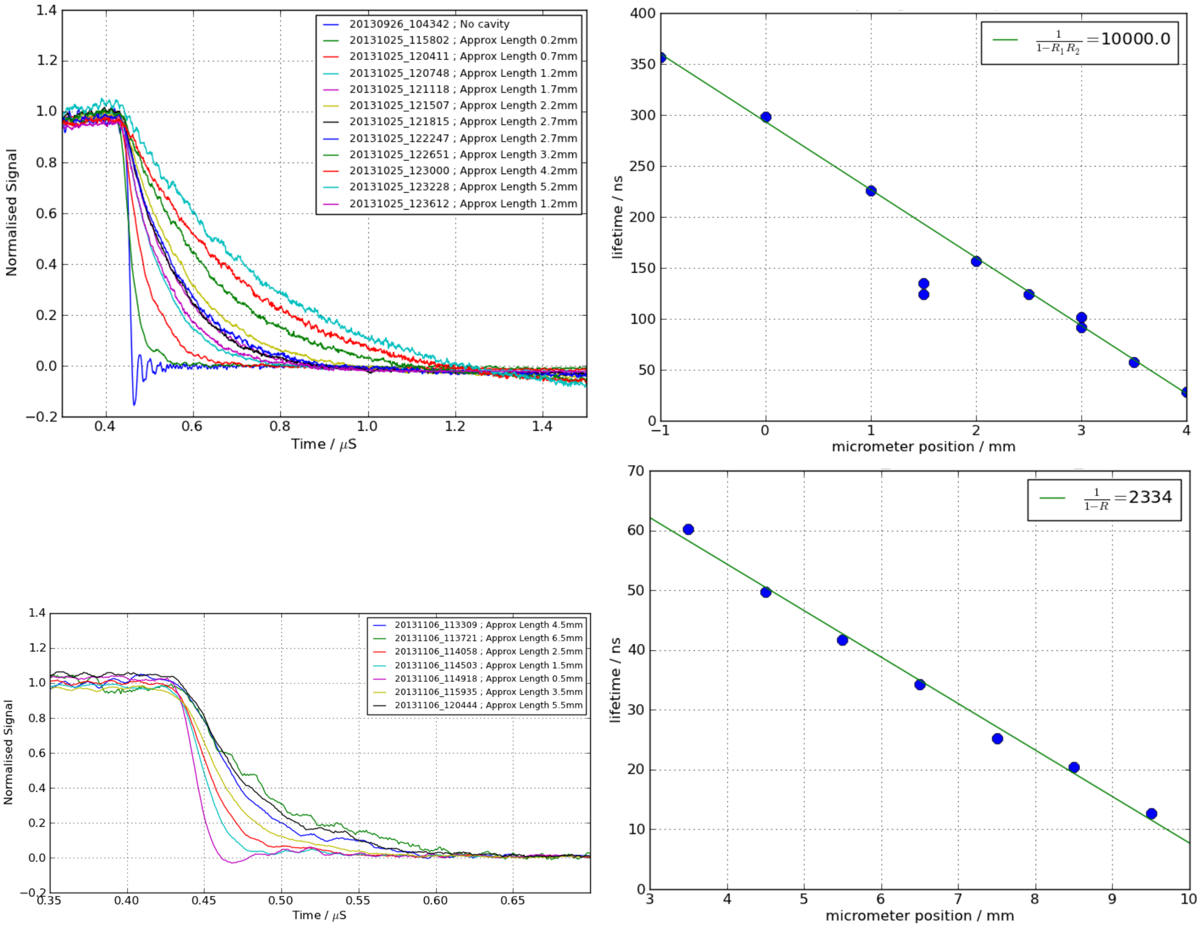

Figure 2.11: Ringdown comparison for several cavity lengths, including no cavity, for two spherical mirrors. The left graphs shows the exponential decay of light from different lengths of cavity which leads to an increase of the time constant. The right graphs shows these time constants plotted against length of cavity. The straight line fit is done by eye and the legend shows the implied round trip count. Note that lower micrometer positions correspond to longer cavity lengths. Top two graphs are for a spherical-spherical cavity, bottom graphs for a spherical-planar.

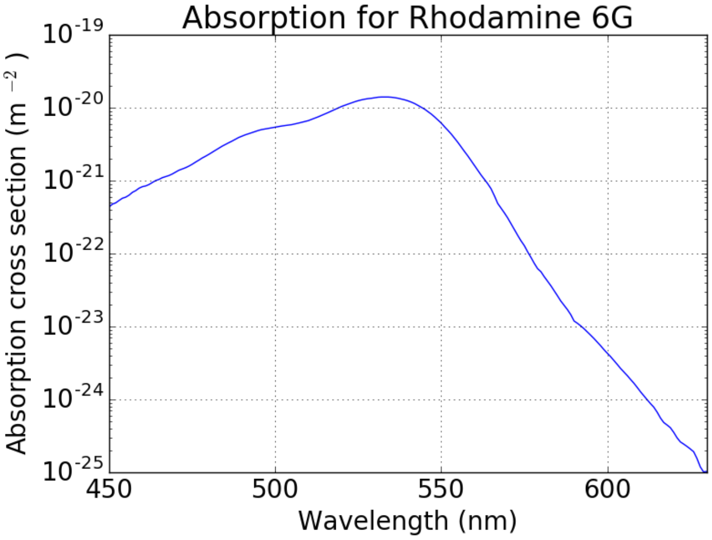

Figure 2.12: Absorption cross section of Rhodamine-6G, taken at various concentrations using a single-monochromator spectrophotometer. Data taken in four different concentrations and stitched together depending on which concentration best uses the dynamic range of the detector.

2.3.2 Fluorescence Spectrum of Dye

We measured the fluorescence spectrum of the dye by placing a drop of it between two optical flats and pumping with a laser. The emission light was directed to the spectrometer. This data and the absorption data can be found on the research data repository Zenodo[55].

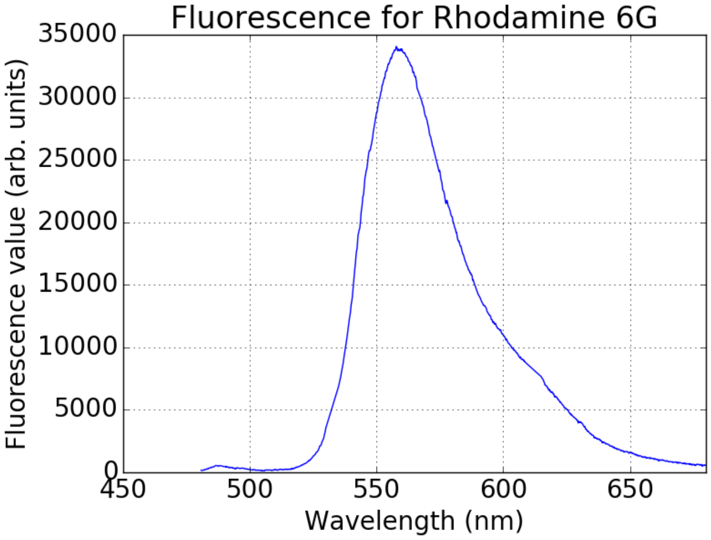

Figure 2.13: Fluorescence emission spectrum of Rhodamine-6G

2.3.3 Checking the Kennard-Stepanov Relation

Our measurements of the fluorescence spectrum $f(\omega)$ and absorption spectrum $A(\omega)$ of the dye allow us to check the Kennard-Stepanov Relation. We can calculate an implied temperature from the spectra $T_{spectral}$, which should be equal to room temperature if the relation holds. We start the derivation from the Kennard-Stepanov relation itself:

$$\frac{f(\omega)}{A(\omega)} = C \exp\left(-\frac{\hbar\omega}{k_B T}\right) \tag{2.13}$$

where C is a constant of proportionality, ω is the angular frequency of light and the other symbols have their usual meanings. The absolute values of the fluorescence and absorption do not matter only their ratio does, so we can choose the constant of proportionality C to be unity at the zero phonon line (ZPL). From there we convert to wavelength λ, λ_{ZPL} and rearrange to obtain temperature:

$$T_{spectral} = \frac{hc}{k_B \log\left(f(\lambda)/A(\lambda)\right)}\left(\frac{1}{\lambda} - \frac{1}{\lambda_{ZPL}}\right) \tag{2.14}$$

Figure 2.14 shows the normalised fluorescence and absorption spectra on the same graph with the zero phonon line as the line of symmetry. The implied temperature is plotted showing that it indeed is very close to room temperature in the range of wavelengths where these photon BEC experiments take place, demonstrating that the Kennard-Stepanov relation holds.

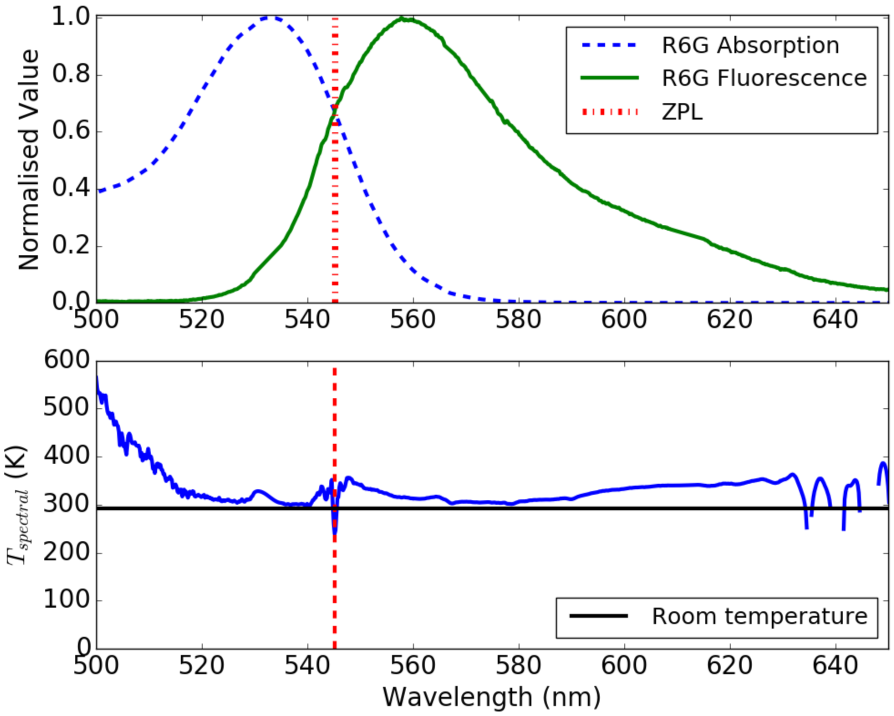

Figure 2.14: Top: Normalised fluorescence and absorption spectra data with the zero phonon line as the line of symmetry. Bottom: Implied temperature from spectra assuming that the Kennard-Stepanov relation is true. Spectral temperature is close to room temperature at relevant wavelengths 550 – 590 nm for the Photon BEC experiments.

2.4 Control Software and Automation

The manufacturers of our cameras, spectrometer, piezoelectric and stepper motor translation stages have provided software application programming interfaces (APIs) to allow control and data acquisition. The camera and spectrometer interface was made by modifying the C++ example programs to connect to a python extension module, that way a python script written by us could be written to access the C++ code which interfaced with the cameras and specrometers. A very useful trick was in in the C++ code to obtain the pointer of a python numpy array, writing data to this pointer made the data appear on the numpy array in python. This allowed quick transfer of data from the camera or spectrometer to the python script, as no new memory needed to be allocated. The translation stages which control the interferometer mirrors (see chapter 4) were controlled by reading their manual and implementing their protocol in python.

For storing the experimental data on disk, each data run has an associated metadata file which contains the timestamp, parameters, comments and links to the camera images, spectrum, interferometer camera fringes compressed in zip files or other raw data depending on the experiment. The timestamp allows us to quickly find and cross-reference different pieces of data taken at different occasions, each type of data is stored in a device-specific filetype. The source code can be found on the project's Github page[67].

2.5 Stabilising the Cavity

The cavity is uniformly illuminated by 633 nm wavelength Helium-Neon laser light chosen because it is narrowband, stable and cheap. The longitudinal modes of the cavity are visible as red circles centred at the cavity centre with a radius depending on the cavity length. By analogy with Newton's rings, these circles are contour lines of the points where the length is equal to an integer number of 633nm half-wavelengths. A camera (this make/model is called Point Grey Flea, chosen because of its speed) connected to a computer, monitors the ring radius taking greyscale images with frame rates up to 150Hz (although only with the brand-specific USB3 card).

2.5.1 Cavity Lock

The creation of the camera- and piezo- control interface, as well as the 633nm He-Ne laser, allowed the implementation of cavity length stabilisation. We created a GUI for the lock software. The centre of the rings is found by using an algorithm which minimizes a cost function related to the apparent ring width. This algorithm is not perfect so the cavity image is also shown to the human user who is prompted to click the centre. The ring radius is obtained by calculating the radial profile of the intensity. A peak appears at the radius matching the laser ring. Figure 2.15 shows an image from the Flea camera overlaid with a circle of the detected ring radius. The black area of the image corresponds to the reflective mirror surface, the grey areas are the non-reflective mirror mount. The imperfections and damage of the mirror can be seen in the non-circular rings and other marks. This ring radius is the signal fed back to the piezoelectric actuator through a proportional-integral controller algorithm. The application also creates a server socket allowing other applications to communicate with it, this was very useful for automatically changing the cavity length to take data as a function of the cutoff wavelength.

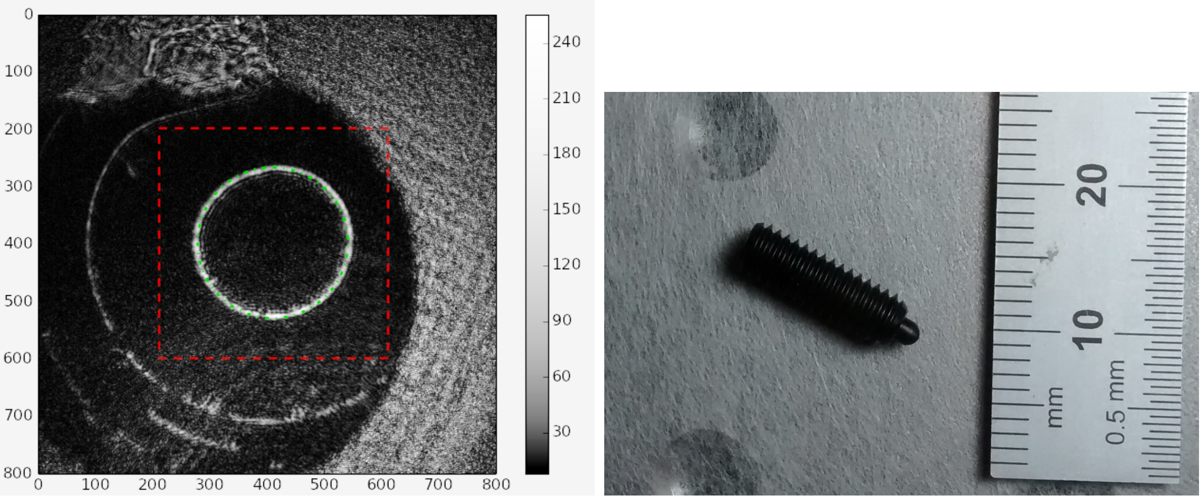

Figure 2.15: Left: Point Grey Flea camera image showing He-Ne rings. Green circle is fitted ring radius. Red square is search region. The mirror appears black on this image and the grey arc on the right side is the non-reflective mirror mounting. The non-circular rings and imperfections correspond to mirror damage. Right: Spring screw used to further stabilise the cavity length, the tips press against PEEK disks to brace the cavity.

Cavity Lock Stabilization Algorithm

The ring radius data is fed to a discrete proportional-integral-double-integral (PIII) controller. In a very similar way to the PID controller used in the laser power stabilization (see chapter 6 for a more detailed explanation), this software calculates the difference (called the error signal) between set point and current signal. This error signal is operated on with a proportional gain, integral gain and double-integral gain, and then fed back to the input (in this situation, the cavity length piezoelectric actuator). As before, the entire source code can be found on the project's github page in the `CavityLock/` directory.

The Cavity Lock software was successful in stabilising on the longer time frame, in the order of one second to minutes. The remaining noise was equivalent to about 0.7nm in wavelength and was visible on the spectrometer.

2.5.2 Spring Screws

The Cavity Lock software was unable to stabilise on a shorter timescale than about 1 second so to further improve stability we used spring screws as pictured in figure 2.15. We obtained three small disks about 1cm in diameter made of polyether ether ketone (PEEK) and superglued them onto the planar mirror mount. On the spherical mirror mount we had drilled and tapped three screw holes to hold ball and spring plungers (part number Wixroyd 31600.W0104), essentially screws with springs on the end. These press against the PEEK disks. A careful (and not always repeatable) procedure of slowly screwing them in along with the micrometer actuator resulted in the cavity braced against the screws but still able to change length over the length of a few cavity modes. The capped springs increased the stiffness of the mirror assembly which moved the resonance away from our interesting region of frequency space. The result was an increased coherence time (see chapter 4) by a factor of about three and reduced the noise fluctuations in wavelength to about 0.1nm.

2.6 Technique for Cleaning Cavity Mirrors

One of the perpetual problems with data-taking in the Photon BEC experiment is dirt appearing in the cavity[1]. We investigated several possible methods for the best way of cleaning the mirrors, and using a microscope to observe we settled on the following method.

To clean the cavity mirrors, fully lengthen the cavity and wearing latex gloves remove the spherical mirror mounting. Fold a piece of Thorlabs optical cleaning paper many times and hold it with a surgical clamp, pour High-Performance Liquid Chromatography (HPLC) grade methanol onto the bundle of paper and with some force wipe the mirror once. Do this for both mirrors and replace the spherical mirror mounting. A quick alternative to cleaning this way which sometimes works is to repeatedly lengthen and shorten the cavity using the piezoelectric actuator which may move, break up or dissolve the dirt.

Other methods attempted at various times were using First Contact optics cleaning solution, and an airbrush with the same HPLC methanol.

2.7 Obtaining Filtered Dye

The dye used is Rhodamine-6G dissolved in Ethylene Glycol at a concentration of 2 millimolar. We filter four times before putting a drop of dye in the cavity, which is held in place by surface tension. Twice the dye is filtered in a funnel with 0.7 μm filter paper and once with a 0.2 μm syringe filter. This dye is placed in a syringe with another identical syringe filter and so filtered once more immediately before reaching the cavity.

2.8 Obtaining BEC

2.8.1 Thermalisation

Under the right conditions (single mode cavity, 7mM – 0.2mM dye concentration, pump spot size well matched to cavity mode) the thermalisation is visible. Applying Bose-Einstein statistics to the density of states of a short cavity yields a curve of the emission from the cavity vs wavelength, described by equation (1.9). Fitting this using least-squares with log-difference residuals to the data gives a room temperature fit as shown in figure 2.16. See chapter 3 for much more details about the evidence that this is indeed genuine thermalisation.

---

[1] This may be due to polymerisation of the dye or another unknown mechanism but for the purposes of this text we will just call it dirt.

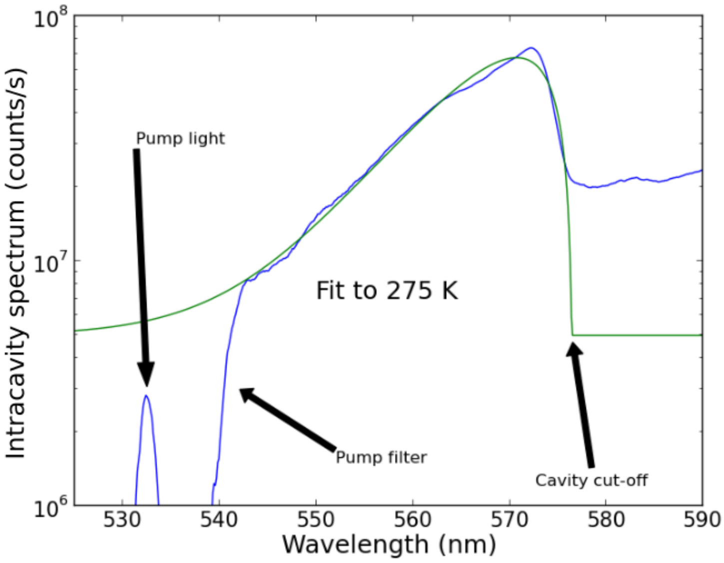

Figure 2.16: Spectrum of background-subtracted cavity light, demonstrates thermalisation essentially at room temperatures. Fitted to equation (1.9) with cutoff wavelength $\lambda_0 = 575$ nm. The data at wavelengths higher than 575 nm also includes emission from the next longitudinal mode.

2.8.2 BEC Threshold

Once thermalisation is confirmed, we increase the number density by raising the pump power until a threshold is reached. At this point the lowest energy state at the cutoff wavelength will become macroscopically occupied with photons, as in figure 1.7 from the Klaers paper[36]. This is photon BEC. This process can be observed on the spectrometer as in figure 2.17 which shows the process of increasing pump power to induce BEC at the ground state. Condensation appears as a peak at the cutoff wavelength. We use the camera to take a real space image of the cavity. It shows the condensate appearing as a bright spot in the centre of the thermalised cloud which is also the center of curvature of the cavity. The cross-section through the image shows the peak of the condensate appearing after threshold. The data is shown in figure 2.18. We first achieved threshold behaviour in December 2013 but it took us until May 2014 until we convinced ourselves of thermalisation with further measurements (see chapter 3).

2.9 Conclusion

We built an experimental setup for creating photon BEC. Rhodamine-6G dye is held by surface tension between two parallel high-reflectivity mirrors in a cavity. Laser pump light is chopped by an AOM to stop the triplet excited state population of the dye from being populated, and enters the cavity at an angle-of-incidence corresponding to the maximum of transmission of the mirrors. The photons in the cavity become thermalised and BEC is achieved when the pump intensity goes above a threshold. The cavity length is stabilised with a He-Ne probe laser and spring screws, and the finesse of the cavity is measured with a ringdown measurement.

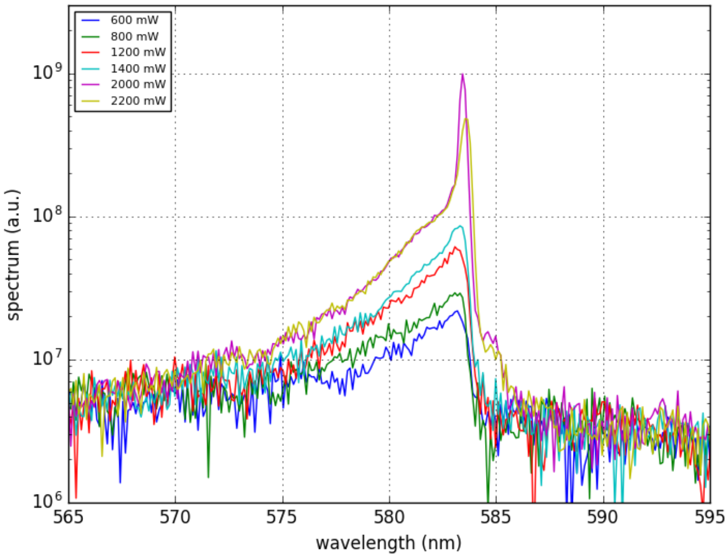

Figure 2.17: Increasing pump power to induce Bose-Einstein condensation in thermalised photons. Legend is nominal pump power emitted from the laser (which is attenuated mainly by the AOM before reaching the cavity). At pump powers below threshold the spectrum matches the thermal cloud distribution (eq (1.9)). Pump powers above threshold (about 600 mW) show a peak at the cutoff wavelength as the ground state becomes macroscopically populated. Note that this data predates the cavity stabilization (see Section 2.5) so the location of the cutoff wavelength fluctuates between readings.

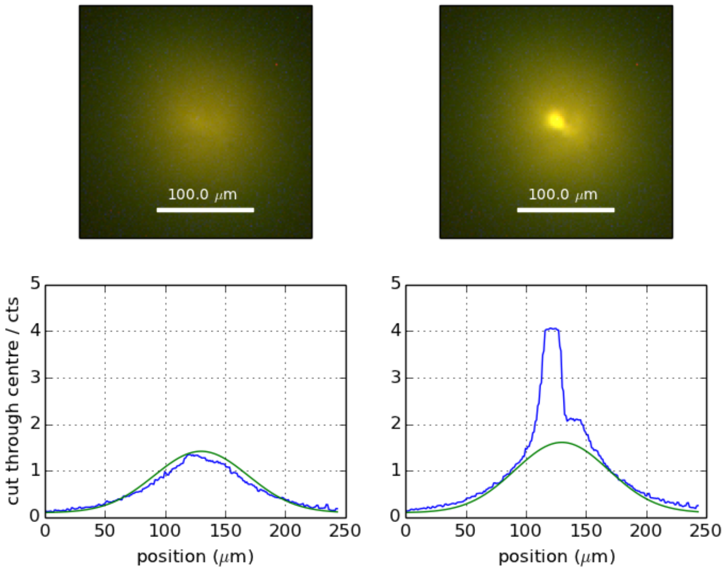

Figure 2.18: Camera image of cavity light, just below and just above BEC threshold pump power. The curves are fitted to the wings only because the central peak of BEC does not fit the thermal cloud gaussian. The cutoff wavelength is 590 nm and the condensate appears at the center of the thermal cloud which is at the center of curvature of the cavity. The transverse modes can be seen further away from the cavity center by the shorter-wavelength colours.

Chapter 3

Demonstrating Thermalisation

This chapter aims to demonstrate that the dye-filled microcavity system indeed produces thermalised photons, and therefore the condensation phenomenon is a true Bose-Einstein condensate. The chapter has data mostly taken in 2014 soon after BEC was achieved. Many of the results were published in Physical Review A[48]

3.1 Thermalisation and Thermal Equilibrium

Bose-Einstein condensation is defined as macroscopic occupation of the ground state at thermodynamic equilibrium of bosonic particles. In the previous two chapters we demonstrated a microcavity can create a ground state for photons and how this ground state can become macroscopically occupied. To show that this is true BEC we need to demonstrate that the photons are indeed at thermodynamic equilibrium. The photons being confined spatially by the cavity places them in mechanical equilibrium, so this chapter is about showing that they are in thermal equilibrium. The mirrors confining photons in space and so providing mechanical equilibrium can be seen as the equivalent of the magnetic trap which confine the atoms in atomic BEC experiments.

The models of photon BEC at the time these investigations took place also all had the assumption of spatial homogeneity of pumping and loss. In this chapter we find evidence against homogeneity of pumping but not of loss. The model used in the first photon BEC paper [36] calculates an average number of photons in the cavity and that above a certain photon count a condensate will form. These models would benefit from more experimental data. Kirton and Keeling used their published model[68][53] to investigate thermalisation of the photon gas. At low temperatures or large cavity losses, the absorption and emission rates of photons were too small to allow them to reach thermal equilibrium. So BEC cannot happen if thermalisation breaks down. They were able to plot “phase-diagrams” showing regions where BEC was a good or bad description.

What follows is a simple model of BEC in a dye-filled cavity. We derive some expressions and evaluate some quantities to analyse the system, later we use this as a guide to interpreting our data and to what extent this simple model reflects reality. In the introduction chapter we derived equation (1.13) the critical photon number for a BEC in our conditions. $N_C = \frac{\pi^2}{6}\left(\frac{k_B T}{\hbar\Omega}\right)^2$ where T is temperature and $\Omega = (c/n_L)\,1/\sqrt{LR}$ is the trap frequency with c/n_L being speed of light in the dye, L being cavity length and R being spherical mirror radius of curvature. By assuming homogeneous pumping, we find an expression for N_{cav} the number of photons in the dye-filled cavity. It is equal to the light power absorbed P_{abs} at the pump wavelength λ_p divided by the energy per absorbed photon $E_p = \frac{hc}{\lambda_p}$, multiplied by the time spent in the cavity by the photons τ_{cav}, which results in:

$$N_{cav} = \frac{P_{abs}\tau_{cav}}{E_p} \tag{3.1}$$

We can set $\tau_{cav} = F \times \frac{L}{c/n_L}$, the round trip count[1] F multiplied by the cavity round trip time. Also we can replace the cavity length with an expression relating longitudinal mode number q, cutoff wavelength λ_0 and refractive index of dye medium n_L, all of which are more easily observed in lab, $L = q\lambda_0/2n_L$ resulting in:

$$\tau_{cav} = \frac{F\lambda_0 q}{2c} \tag{3.2}$$

P_{abs} is found by considering n_{mol} the number density of dye molecules and A the absorption cross section for light at wavelength λ_p. Using change of intensity $dI = -n_{mol}AIdz$ for the absorbtion of light of intensity I through a distance dz and assuming a thin layer of absorbing dye in the microcavity being only 3-4 wavelengths long, we obtain an expression for power absorbed:

$$P_{abs} = n_{mol}AP_pL_{dye-short} \tag{3.3}$$

where $L_{dye-short}$ is the length of the dye in the cavity that the laser beam passes through. Figure 3.1 is a diagram of the cavity showing the difference between the cavity length of the dye and cavity length of the field, and the path of the pump light through the cavity. The electric field penetrates into the dielectric-stack mirrors where each stack reflects a proportion of the light back. The length of cavity experienced by the light field is equation (2.2) $L = q\lambda_0/2n_L$. The length of the cavity experienced by the dye assuming a short cavity is:

$$L_{dye-short} = \frac{(q - q_0)\lambda_0}{2n_L} \tag{3.4}$$

Where $q_0 \approx 4$ is the mode number indicating the depth of light field penetration. For a longer cavity the thin-cavity assumption does not hold and the absorbtion equation gets an exponential shape, also the angle of the pump beam at 37° internal angle has an effect, the effective cavity length which we'll use later is then:

---

[1] The average number of times a photon makes a round trip in the cavity before leaving through one of the mirrors

$$L_{dye-long} = \frac{(q - q_0)\,\lambda_0}{2n_L cos\,(37°)} \tag{3.5}$$

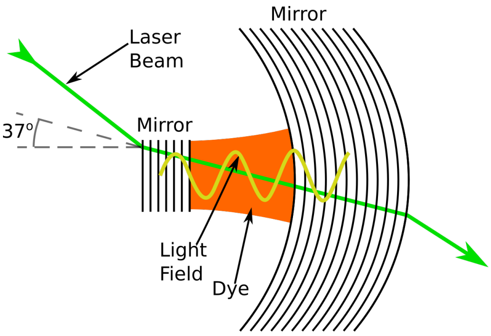

Figure 3.1: Diagram of mirrors, dye (orange), cavity light (yellow) and pump beam (green). Mirrors are drawn as dielectric stacks with the light penetrating into them. The dye is held by surface tension. The laser pump light enters at an internal angle of 37°.

From this the number of photons in cavity is:

$$N_{cav} = \frac{P_p n_{mol} A F \lambda_0^2 \lambda_p q\,(q - q_0)}{2n_L h c^2} \tag{3.6}$$

This quantity can be measured experimentally by observing the intensity of the light exiting at one mirror of the cavity. We can use this N_{cav} and equation (1.13) to derive a critical power, which is easily measured experimentally. Imposing $N_{crit} = N_{cav}$ and set $P_p \to P_c$, we obtain:

$$P_c = \frac{2\pi^4 g R\,(k_B T n_L)^2}{3h n_{mol} A F \lambda_p \lambda_0\,(q - q_0)} \tag{3.7}$$

We can evaluate to get an estimate of the critical power. Using a known figure of the cross-section for Rhodamine6G at the pump wavelength of 2.5×10^{-20} m^2 and knowing the concentration of our dye droplet is 2.2 mM, taking the round-trip count F to be 20000 and $n_L = 1.44$ as usual, which gives a result of about 80 mW for BEC threshold pump power which is within the right order of magnitude to real experiments.

The thermal cloud in our model would be of a size determined by the mirror curvature and temperature. The size can be derived by equating the thermal energy to the potential energy: $\frac{1}{2}m\Omega^2 r^2 = \frac{1}{2}k_B T$. Rearranging and setting $r \to \sigma_{th}$ results in the thermal cloud size of $\sigma_{th} = \sqrt{k_B T q \lambda_0^2 R / 2hcn_L} \approx 70\ \mu$m.

3.2 Setup

3.2.1 Measuring Beam Size

The pump spot size can be changed by defocusing the pump lens (see figure 2.4). The cavity length must be long enough so that many different longitudinal modes are excited and so the photoemission reflects the size of the pump spot rather than the size of any cavity modes. As the pump beam enters off-axis the pump spot is typically elliptical, the difference in fit between the axes dominates the error of this method of measuring the pump spot size. Figure 3.2 is an example pump spot with fit in both axes.

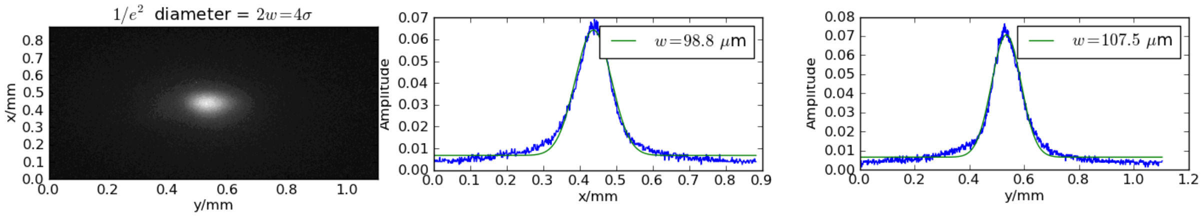

Figure 3.2: Example pump spot fitted with a 2D gaussian. The cavity is lengthened so that many longitudinal modes can be populated so that the cavity emission will match the pump spot. The uncertainty in this measurement is determined by the difference between the y-axis fit width and the x-axis fit width. In this particular measurement we obtain $\sigma_p = 103 \pm 4\mu$m.

3.2.2 Measuring BEC Threshold

The threshold pump power P_{th} is the nominal power at which BEC starts to be formed. We measure it by varying the pump power and noting when the spectrum deviates from the thermal cloud number distribution. The thermalised gas spectrum is followed for the lower powers, after threshold the ground state energy develops a peak as it becomes macroscopically occupied. This method has proven to be repeatable and precise, however it is fairly labour-intensive and somewhat subjective. A more automated method we also tried was to fit a cross-section of the camera image to a gaussian. Threshold is found when the fit breaks down as also shown in the figure 3.3.

3.2.3 Measuring Cavity Photon Count

We can infer the number of photons in the cavity, N_{cav} by measuring the power of light leaking from one mirror P_m and accounting for mirror transmission $T(\lambda)$ and cavity round trip time; the result is: $N_{cav} = P_m q \lambda^2 / hcT_m(\lambda)$. The power P_m is measured using a photodiode. Figure 3.4 shows the setup used, the cavity light is collected with an objective lens, then filters are used to remove any 532 nm pump light and any light with a wavelength longer than 620 nm using an edge filter, the light is then focussed onto the photodiode. The interesting cavity light from the thermal cloud is in the range 532 nm – 600 nm. We use the photodiode responsivity from the manufacturer's datasheet to convert the voltage reading into an optical power.

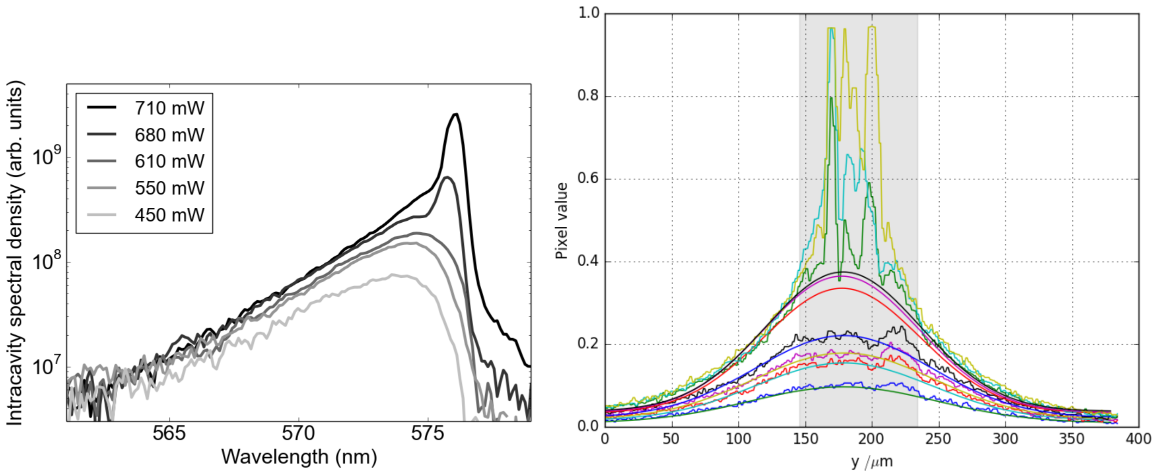

Figure 3.3: Left: Spectrum data at varying nominal pump powers. At powers below threshold of 610 mW the spectrum follows the thermal number distribution. After threshold of about 680 mW a peak develops at the ground state. Right: Cross-sections through the centre of camera image. Fits are gaussian excluding the greyed-out area. Threshold is seen where the centre of the cut no longer follows the thermal cloud gaussian shape. The spiky character is an artifact of dust in the cavity.

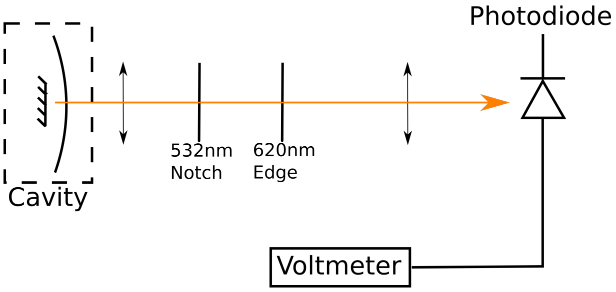

Figure 3.4: Cavity photon count measurement is done by measuring the light power from the thermal cloud. A 532 nm notch filter is used to remove any stray pump light and a 620 nm edge filter is used to remove any stray dye fluorescence emission wavelengths that are not part of the thermal cloud. Voltage is converted to number of photons in cavity.

3.2.4 Measuring Dye Concentration in Cavity

For the next calculation we want to find the number density of Rhodamine-6G dye. Starting from the Beer-Lambert law of absorption, the transmission T_{BL} is

$$T_{BL} = e^{-AlN} \tag{3.8}$$

where again A is the cross section at the pump wavelength 532 nm, l is the path length and N the number density in question. We can also relate the path length to the cavity longitudinal mode number q using equation (3.5). From data taking we have fits for the transmission of the cavity against piezo voltage which controls cavity length $T\left(V_{pzt}\right)$, and the longitudinal mode number against piezo voltage $q\left(V_{pzt}\right)$.

$$T\left(V_{pzt}\right) = Be^{\beta V_{pzt}} \tag{3.9}$$

$$q\left(V_{pzt}\right) = mV_{pzt} + c \tag{3.10}$$

Where B, β, m and c are fitting parameters. We combine these equations together along with equation (3.5) to obtain an expression for transmission as a function of l.

$$T\left(l\right) = Be^{\beta\frac{c}{m}}e^{\beta\frac{q_0}{m}}e^{\frac{\beta}{m}\frac{2n_L cos(37^\circ)}{\lambda_0}l} \tag{3.11}$$

This is the same form as equation (3.8) so we can equate the exponents and rearrange to find N.

$$N = -\frac{2n_L\beta cos\left(37^\circ\right)}{m\lambda_0 A} \tag{3.12}$$

Then we measure the transmission of the cavity at various piezo voltages in order to obtain experimental values of the fitting constants β and m. See figure 3.5 for the data and values of these parameters, which show a linear and exponential fit as expected. Plugging in the numbers results in a dye concentration of 4.8mol/m^3. In our photon count measurement data we find fewer photons than expected. One suggestion for the cause was that photo-bleaching of the dye caused molecules to permanently stop fluorescing. The inferred concentration of 4.8 mM of dye means the dye concentration actually rose from 2.2 mM rather than fell, presumably because of the ethylene glycol solvent evaporating in the few days since the last dye change. However it is a small change compared to the difference between measured and expected photon count and our results cannot be explained solely this way.

3.3 Data

3.3.1 Threshold Power versus Pump Spot Size

The simple model used earlier ignores any effect of photon reabsorption by the dye, as well as assuming that the details of pump geometry are irrelevant to coupling the photons to the cavity. The Figure 3.6 shows the threshold pump power against the spot size which contradicts the assumption of homogeneity. The graph shows the threshold pump power at different pump spot sizes with a fit to guide the eye following a power law distribution of $P_{th} \propto \sigma_p^{1.5\pm0.1}$. It suggests that the redistribution of photons from pump to thermal cloud is not fully efficient, because it does not follow equation 3.1 which predicts the threshold power does not depend on pump spot size.

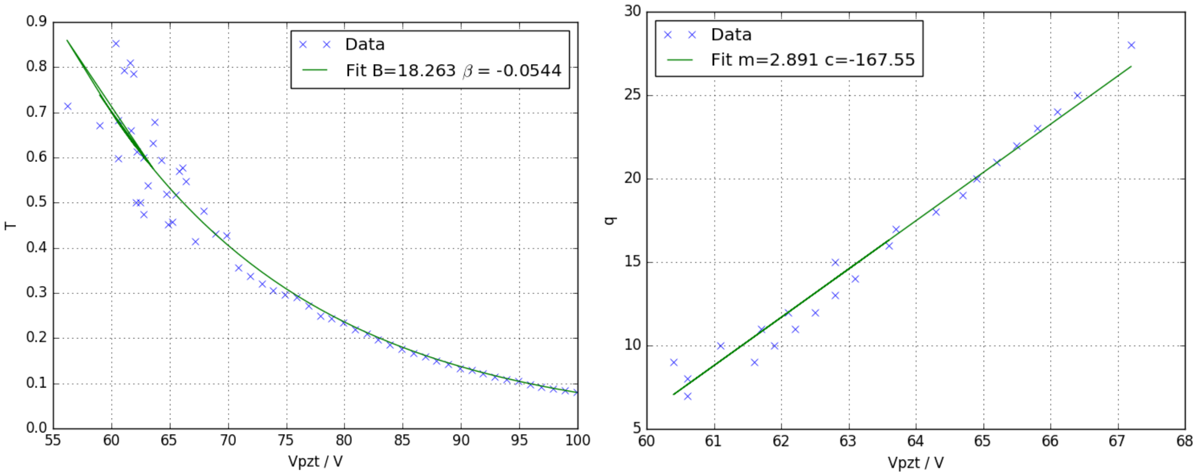

Figure 3.5: Left: Transmission of cavity plotted verses piezo driver voltage and fitted to exponential law as in equation (3.9). Right: Longitudinal mode number plotted verses piezo driver voltage with linear fit as in equation (3.10). This data is used to obtain fit paramaters which are required to measure the concentration of dye in cavity. We find an increase in dye concentration which is not sufficient to explain a drop in thermal photon number.

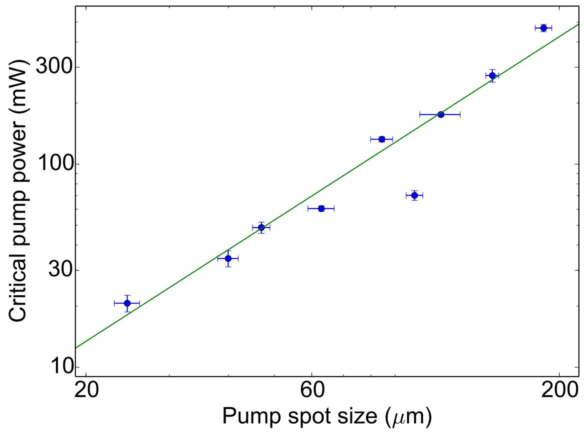

Figure 3.6: Critical (threshold) pump power variation with pump spot size. Taken at $\lambda_0 =$ 586nm at longitudinal mode number q = 8. Fitted to $P_{th} \propto \sigma_p^{1.5\pm0.1}$. The error bars of the spot size represent the difference between the y-axis fit and the x-axis fit, as this ellipticity is the major source of error. The error bars in power come from the range over which threshold power appears to be.

3.3.2 Threshold Power versus Ground State Energy

Measurements of the threshold power while varying the cutoff wavelength and longitudinal mode number are shown in Figure 3.7. We see a minimum of threshold power for each mode number, suggesting two competing effects. This can be understood from existing theory.

At the shorter wavelengths, the photons are closer to the molecular resonances so will be coupled stronger and exist more as molecular excitations, so fewer photons will be available to contribute to the BEC mode, therefore a higher pump power is required to cross threshold[52]. At longer wavelengths, the transmission of the mirrors increases so the cavity loss rate goes up. Eventually it will become close to the thermalisation timescale and a BEC will not be possible; photons would not stay in the cavity long enough. Thus at longer wavelengths the critical pump power must rise too. The minimum threshold pump power we find is a tradeoff between these two effects.

The variation at different longitudinal mode numbers could be explained by the fact photons stay in the cavity for more time in longer cavities, because they reflect from the mirrors less often. This means the balance between loss mechanisms shifts the lowest P_{th} to longer wavelengths.

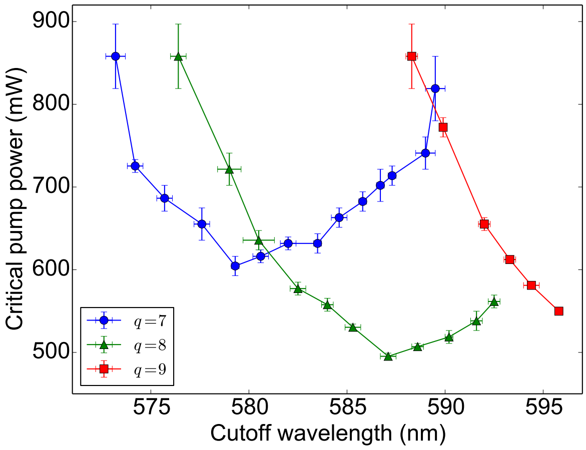

Figure 3.7: Critical (threshold) pump power variation with cutoff wavelength and longitudinal mode number. Taken at $\sigma_p = 170\ \mu$m.

3.3.3 Thermal Cloud Size and Photon Count versus Pump Spot Size

The thermal cloud size below threshold can be measured by fitting to a 2-dimensional gaussian curve in the same way as for measuring the pump spot size. The fitted size can also be used as a measure of thermalisation. Figure 3.8 shows data of the thermal cloud size plotted against pump spot size and it shows the thermal cloud size dropping for pump spot sizes smaller than the thermal cloud but approximately constant for large sizes. This implies that light from larger pump spot sizes thermalises better than small spots, but that pumping with an equal spot size to the thermal cloud size results in optimal coupling. The cavity photon count is measured with a photodiode with the method described earlier and the same figure shows data of N_{cav} verses pump spot size. It again shows a maximum when the spot size is equal to the thermal cloud size σ_{th}.

3.3.4 Thermal Cloud Size versus Ground State Energy

The thermal cloud size is plotted as a function of cutoff wavelength in figure 3.9. Cutoff wavelength is obtained by measuring the spectrum and fitting. This measurement is repeated for two different dye concentrations, the standard used concentration of 2 mM and a much lower concentration of 200 μM. For the standard concentration the result is a mostly constant thermal cloud size regardless of wavelength, while this is less true for the lower concentration. This is an example of how thermalisation can be broken by changing certain parameters, in this case the dye concentration.

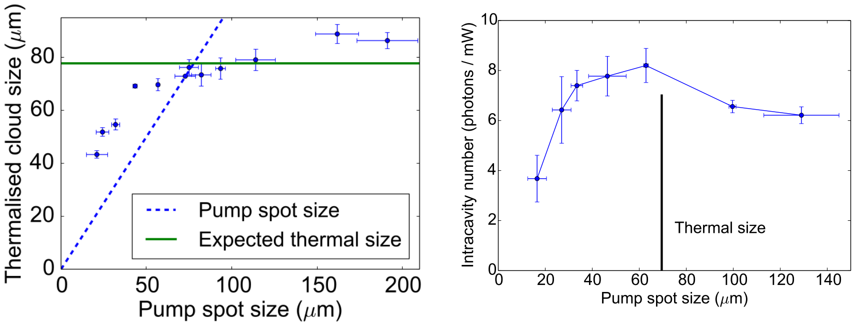

Figure 3.8: Left: Thermal cloud size verses pump spot size. Shows the thermal cloud size dropping for pump spot sizes smaller than the thermal cloud but approximately constant for large sizes. The error bars represent the difference between the y-axis fit and the x-axis fit, as this ellipticity is the major source of error. Right: Thermal cloud cavity photon count normalized to pump power. Taken at eighth longitudinal mode with cutoff wavelength $\lambda_0 = 590nm$. The error in number is found from three repeated measurements at different pump powers. We used continuous wave pumping for this data at a power much lower than any saturation or threshold.

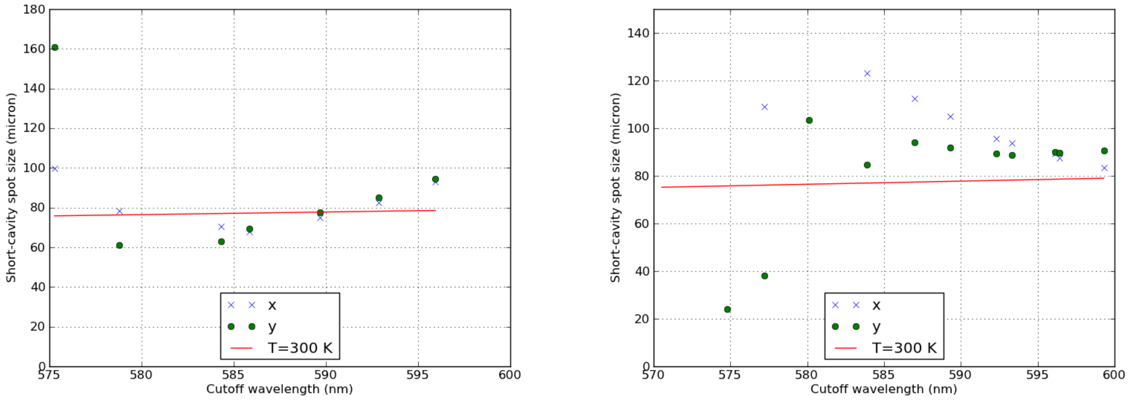

Figure 3.9: Left: σ_{th} vs λ_0 at a dye concentration of 2 mM, showing a constant thermal cloud size for all wavelengths. The single large fit at 575 nm is a bad point due to a smudge in the cavity. Right: Same measurement with dye concentration of 200 μM, showing much more variance and suggesting that thermalisation can be broken by reducing the concentration. Large pump spot size here at 250 μm.

3.3.5 Threshold Power and Cavity Photon Count versus Longitudinal Mode

We can probe the effects of cavity length by adjusting the longitudinal mode number and measuring the photon count and threshold power. Figure 3.10 shows the result where the threshold power varies inversely with q and photon count goes quadratically. This can be made to fit our simple model of equations (3.6) and (3.7), suggesting that the model of photons being absorbed by the dye in this manner reflects reality here. The intracavity photon count graph could also be fitted by a straight line instead of a quadratic, we fitted with a quadratic because we have a model where such a fit makes sense. This data is inconclusive on its own.

3.3.6 Timescale Effects in Thermalisation

We want to distinguish thermalisation from other effects that merely look like true thermalisation. To further convince we demonstrate that thermalisation breaks down in accord to a theory based on timescales. Thermalisation can be broken by having the photons leave the cavity through the mirrors before they scatter enough to thermalise. From the spectrophotometer measurements of cross section $\sigma(\lambda)$ at wavelength λ, we calculate the photon scattering timescale τ_s from equation (3.13). We also know the photon cavity lifetime τ_c from equation (3.14). These equations are derived in chapter 2.

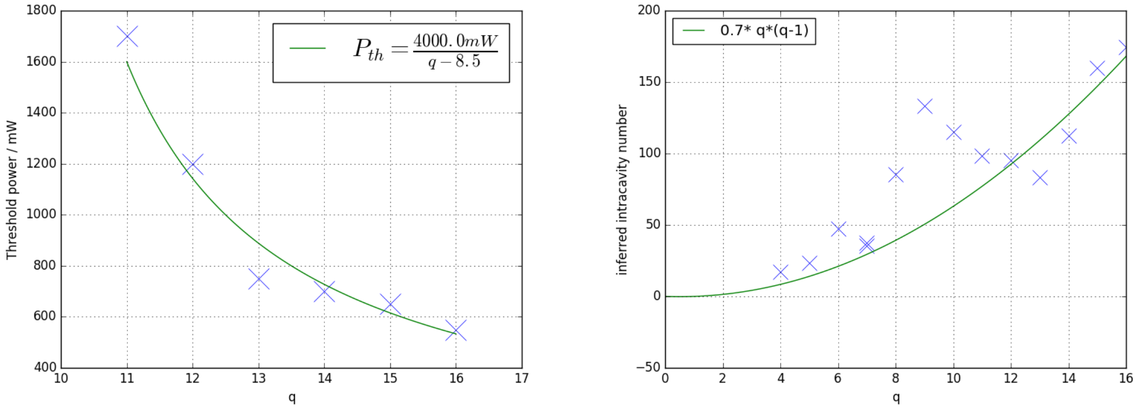

Figure 3.10: Left: Threshold power versus longitudinal mode number q. Shows an inverse correlation matching with equation (3.7). Right: Intracavity photon number varying quadratically with mode number, matching equation (3.6).

$$\tau_s = \frac{1}{c^* n\sigma(\lambda)} \tag{3.13}$$

$$\tau_c = \frac{2L}{c^*}\frac{1}{1-R_1R_2} \tag{3.14}$$

Where c^* is the speed of light in the dye medium, n_{mol} is the number density of molecules,

R_1, R_2 are reflectivities of each cavity mirror and L is the cavity length. The manufacturers of our mirrors provided reflectivity as a function of wavelength $R(\lambda)$, which shows a significant variation but has a flat stop band at the wavelengths relevant to this experiment.

A necessary condition for thermalisation is $\tau_c > \tau_s$, namely that the photons scatter off of the dye molecules before they leave the cavity. Plotting both equations on the same graph verses wavelength (see figure 3.11) allows us to see regions where thermalisation is possible and regions where thermalisation breaks down. The plot shows us a crossover between the two timescales. Plotting the wavelength this crossover happens at against dye concentration gives us the second plot in figure 3.11. The region above and to the left of the line are non-thermalised while the region down and to the right is thermalised. So to break thermalisation we simply need to move the cutoff wavelength to higher values by lengthening the cavity.

With reference to this, we increase the cavity cutoff wavelength so that absorption of scattered photons is suppressed. We also reduce the dye concentration to 70 μM to reduce the rate of rescattering. Figure 3.12 shows a scan through cutoff wavelengths showing that the shorter wavelengths of the spectra fit much less well at longer cutoff wavelengths, indicating that thermalisation is much poorer. This data reproduces the conclusions from the 2010 Klaers et al[38] paper on photon BEC.

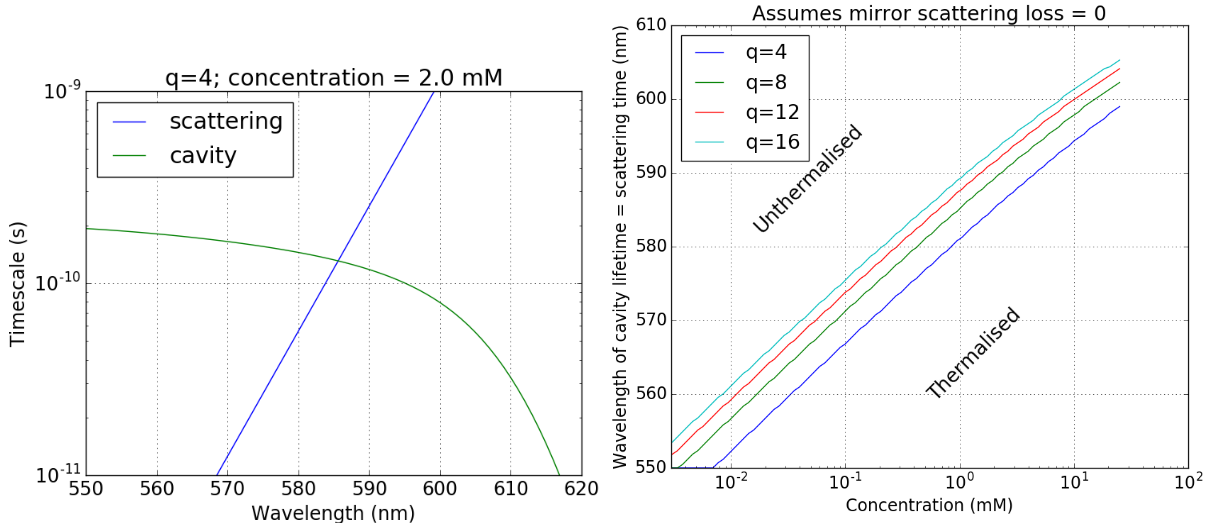

Figure 3.11: Left: Plot of cavity lifetime (eq (3.13)) and scattering time (eq (3.14)), vs wavelength. There is a crossover at approximately 587 nm for these parameters. Right: Plot of crossover wavelength as a function of dye concentration. The different coloured lines refer to the cavity longitudinal mode number.

3.3.7 Discussion

Our simple model is able to show how thermalisation of the cavity light can be broken. The threshold power and cavity photon count vary strongly with pump geometry. Our data suggested a modification to the model by Kirton and Keeling[52] from 2013 to include excited state effects, photon loss and inhomogenous pumping effects. In 2015 soon after our results were published, they updated their model which finds a similar law although with an exponent of 2 rather than 1.5[54]. Their model explains our result through proposing an inhomogenous molecular excitation fraction.

Figure 3(a) in their paper[54] is reproduced here as Figure 3.13. It reproduces our data from figure 3.8 in this thesis. Their paper uses a dimensionless quantity $\eta = \kappa/\rho_0\Gamma_{max}$ where κ is the cavity mode decay rate, ρ_0 is the density of molecules and Γ_{max} the maximum value of absorption of dye molecules. Thermalisation requires $\eta \ll 1$ and a small pump spot σ_p.

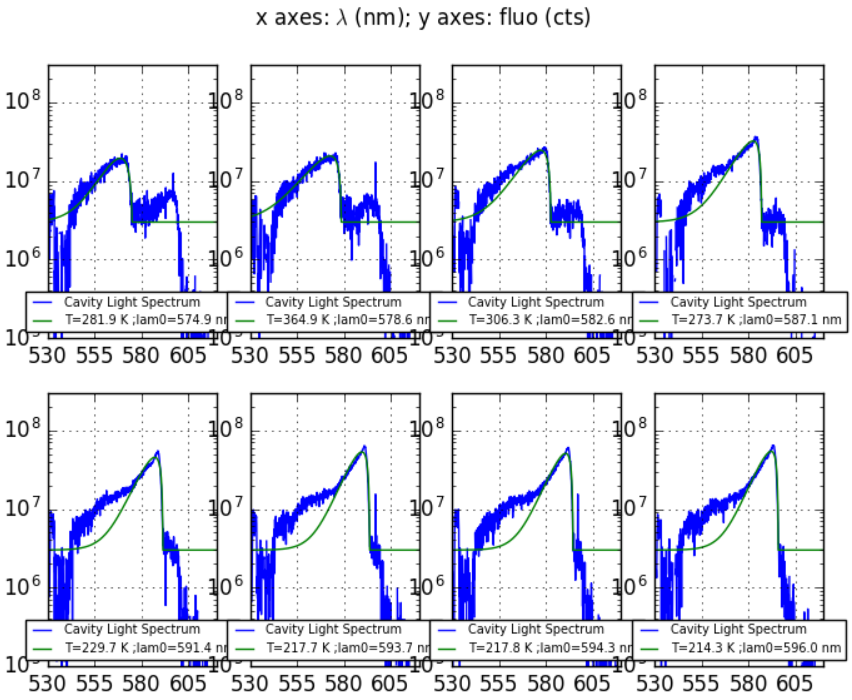

Figure 3.12: Scanning through cutoff wavelengths on the 10th longitudinal mode with 20 μM dye concentration. It shows a marked deviation from the theoretical number distribution curve (eq (1.9)) at longer cutoff wavelength which demonstrates thermalisation breaking down.

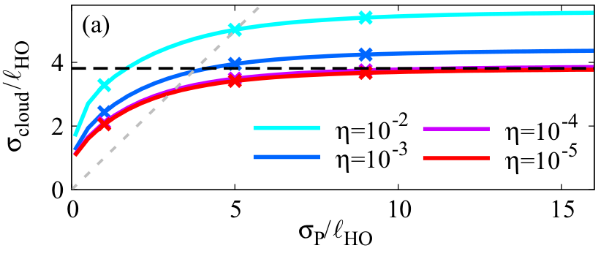

Figure 3.13: Kirton and Keeling updated model results corresponding to our figure 3.8 showing thermal cloud size versus pump spot size. l_{HO} refers to the characteristic scale of the cavity harmonic oscillator. η refers to the ratio of cavity mode decay rate, density of molecules and maximum absorption by dye molecules.

3.4 Conclusion

We took data of photon BEC and below-threshold thermal cloud in an effort to find under which conditions thermalisation breaks down. Data is taken of the threshold power, thermal cloud size and population of photons inside the cavity. We found that a simple homogeneous pumping model cannot explain some of our results. We found the conditions under which thermalisation can be broken, which shows thermalisation is a real effect matching theory and so BEC is a good description of this system. The Kirton and Keeling model[54] explains our results and reproduces our data on threshold power and cavity photon count versus pump spot size.

Chapter 4

Interferometry

4.1 Motivation

Condensation phenomena can be investigated by studying coherence as seen in the first-order correlation function, which is related to visibility measured in an interferometer. This has been investigated in other condensation systems[69, 70]. This treatment is taken from Loudon's book on quantum optics[71] page 92–101. A diagram of a Mach-Zehnder interferometer is shown in figure 4.1 which splits up the incoming field into two arms with different path lengths z_1 and z_2 where z is the axis of propagation, and then recombined in a second beamsplitter.

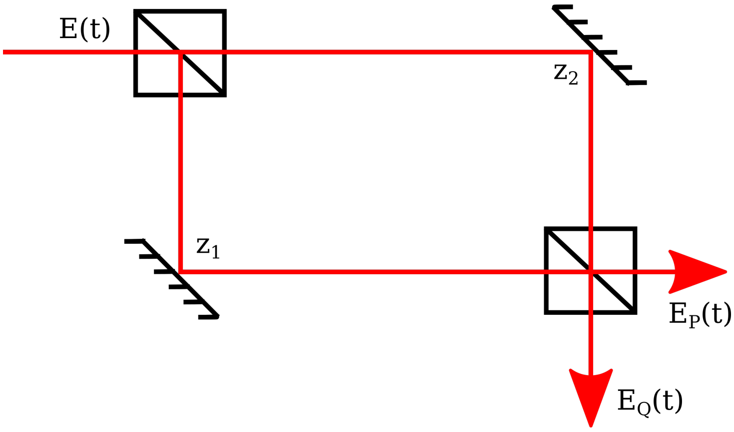

Figure 4.1: Mach-Zehnder Interferometer diagram. An incoming light field is split by a beam splitter into two arms with different path lengths z_1 and z_2 which are then recombined in a second beam splitter. The interferometer has two outputs known as the in-phase (P) and quadrature (Q).

If each beamsplitter has a transmission $\mathcal{T}$ and reflectivity $\mathcal{R}$, then in-phase output port is made up of the superposition of field variables in the two arms:

$$E_P(t) = \mathcal{R}\mathcal{T}E(t_1) + \mathcal{T}\mathcal{R}E(t_2) \tag{4.1}$$

where the times are defined by the propagation path lengths:

$$t_1 = t - z_1/c \text{ and } t_2 = t - z_2/c \tag{4.2}$$

The intensity is found by averaging over a cycle of oscillation:

$$I_P(t) = \frac{1}{2}\epsilon_0 c\,|E_P(t)|^2 \tag{4.3}$$

$$\implies I_P(t) = \frac{1}{2}\epsilon_0 c|\mathcal{R}|^2|\mathcal{T}|^2\left\{|E(t_1)|^2 + |E(t_2)|^2 + 2Re\left[E^*(t_1)E(t_2)\right]\right\} \tag{4.4}$$

Where ϵ_0 and c have their usual meanings of electric constant and speed of light. In an experiment the measured quantity is typically found from a long-term average reading from a camera or photodiode which is over a time T much larger than any coherence time or oscillation time, the time-average :

$$\langle I_P(t)\rangle = \frac{1}{2}\epsilon_0 c|\mathcal{R}|^2|\mathcal{T}|^2\left\{\left\langle|E(t_1)|^2\right\rangle + \left\langle|E(t_2)|^2\right\rangle + \left\langle 2Re\left[E^*(t_1)E(t_2)\right]\right\rangle\right\} \tag{4.5}$$

This quantity consists of three contributions: the first two are just averages of the field in each interferometer arm while the third is the fringes resulting from the interference and involve the *first-order correlation function* for the fields at times t_1 and t_2. This is defined explicitly as:

$$\langle E^*(t_1)E(t_2)\rangle = \frac{1}{T}\int_T dt_1 E^*(t_1)E(t_2) \tag{4.6}$$

It is worth noting that the integral has only one free variable, as t_2 is related to t_1 via equation (4.2). The nature of this first-order correlation function and therefore the interferometer fringes depends on the incident light. Also we assume the processes involved are long-term stationary meaning the starting point of the T does not matter as long as T is long enough. As the result depends on the delay $\tau = t_2 - t_1$ in the interferometer arms, it is helpful to rewrite equation (4.6) in terms of τ.

$$\langle E^*(t_1)E(t_2)\rangle = \frac{1}{T}\int_T dt E^*(t)E(t+\tau) \tag{4.7}$$

The *degree of first-order temporal coherence* of a light field from a stationary process is defined as the normalized version:

$$g^{(1)}(\tau) = \frac{\langle E^*(t)E(t+\tau)\rangle}{\langle E^*(t)E(t)\rangle} \tag{4.8}$$

And the output intensity of the interferometer at the in-phase port can be written involving this new quantity:

$$\langle I_P(t)\rangle = \frac{1}{2}\epsilon_0 c|\mathcal{R}|^2|\mathcal{T}|^2 \left\langle |E(t)|^2\right\rangle \left\{1 + Re\ g^{(1)}(\tau)\right\} \tag{4.9}$$

Now going back to equation (4.5), we assume a plane wave with fixed amplitude E_0, phase ϕ, frequency ω and wavenumber k, and substitute it in:

$$E(z,t) = E_0 e^{(i[kz-\omega t+\phi])} \tag{4.10}$$

$$\implies \langle I_P(t)\rangle = \frac{1}{2}\epsilon_0 c|\mathcal{R}|^2|\mathcal{T}|^2 \left\langle |E(t)|^2\right\rangle \left\{1 + V cos\left[\frac{\omega}{c}(z_1 - z_2)\right]\right\} \tag{4.11}$$

The other output port I_Q has a sin instead of a cos. The quantity V is the visibility:

$$V = \frac{(I_{max} - I_{min})/2}{(I_{max} + I_{min})/2} = \frac{I_{max} - I_{min}}{I_{max} + I_{min}} \tag{4.12}$$

$$\tag{4.13}$$

So we have an expression describing how the interference fringes will have a co-sinusioudal shape as the delay $z_1 - z_2$ is scanned in an experiment. The amplitude of these fringes is the visibility, which by comparing with equation (4.9), we can see is directly related to the degree of first-order temporal coherence.

$$V = \left|g^{(1)}(\tau)\right| \tag{4.14}$$

This model can be generalized to an interferometer setup where the two arms can also translate the beams relative to each other, resulting in the first-order spatiotemporal coherence:

$$g^{(1)}(\vec{r_1}, t_1, \vec{r_2}, t_2) = \frac{\langle E^*(\vec{r_1}, t_1)E(\vec{r_2}, t_2)\rangle}{\sqrt{\langle |E^*(\vec{r_1}, t_1)|^2\rangle \langle |E^*(\vec{r_2}, t_2)|^2\rangle}} \tag{4.15}$$

Thus we have shown how interferometer measurements can provide access to the coherence of a condensate. A Bose gas is expected to be a much more coherent object above threshold. The work for this chapter was mostly done in the author's second year of PhD and was published.[49]

4.2 Setup

4.2.1 Interferometer

Interferometers work by splitting beams of waves in two and then recombining them. The interference pattern between the wavefronts of the two beam paths is used to extract information.

Our interferometer is of the Mach-Zehnder configuration as shown in figure 4.2. One beam splitter is used to split the incoming light. Each arm is influenced by a delay line and/or tilting mirror to shift the position. The two beamlines are combined in another beamsplitter cube which provides two output ports, known as in-phase and quadrature. Two separate polarizations of light from the thermal cloud reduce the visibility so we place a linear polarizing filter to just pick one. The interferometer was built by Lydia Zajiczek in her MSc project[72]. The delay lines use mirrors mounted at 90° to cause the light to always return in the same angle in the horizontal plane. Both output ports are brought in focus onto the same camera so they are recorded simultaneously.

There are two translation stages for delaying the light. The so-called "coarse" translation stage has a stepper motor and has a range of 50mm with resolution about 1μm. The other stage is moved by a piezoelectric driver; it has a range of 20μm with resolution about 20nm and is known as the fine translation stage. We use the fine stage to scan over individual fringes and the coarse stage for scanning longer-range phenomena like the coherence time. There is a stepper motor which turns one screw of a mirror mount, used to tilt one mirror before the second beamsplitter. It can translate the light in one arm of the interferometer which results in one image being translated relative to another, this is used to measure spatial coherence. In general the course stage moves to the desired z-position to choose the desired time delay and/or the tilt mirror is moved to the desired x-position to choose the desired spatial translation, then the fine stage is scanned (after a short delay to allow things to settle) while the camera takes images of both outputs. Note that the z-axis is defined as the direction of light propagation so moving along it in one interferometer arm is equivalent to changing the time delay between the arms, and the x-axis is defined as the horizontal direction so moving along it is equivalent to horizontally shifting one interferometer image relative to another.

The coarse translation stage and the mirror tilt motor are both from Thorlabs with part numbers BSC201 and TST101 respectively. They both use the same serial-port-over-USB protocol to communicate with the computer. We implemented the protocol in python. It uses an object-oriented style to maximize code re-use and readability. The relevant file in our github[67] repository is `thorlabs_apt.py`.

The bottom of figure 4.2 shows the value of a pixel as the fine delay line is scanned, with the value normalized to be all on the same scale. The coarse position moves on a scale of 10 μm while the fine position moves only in steps of 100 nm. The fine position and coarse position are both plotted on the same x-axis but with different scales so that the shape of the fringes can be seen as well as the distance between them. Each new line colour on the graph is a different fringe at a new coarse stage position.

Stability of the cavity length had a significant effect on the interferometer data because the vibrations produce significant amounts of frequency noise. It can be seen how the central fringe is a clear sine wave while the fringes at the edges have no clear frequency due to the cavity length jitter. Improving the cavity stability greatly improved the coherence times measured by this interferometer. More details on the cavity stabilization setup can be found in section 2.5.

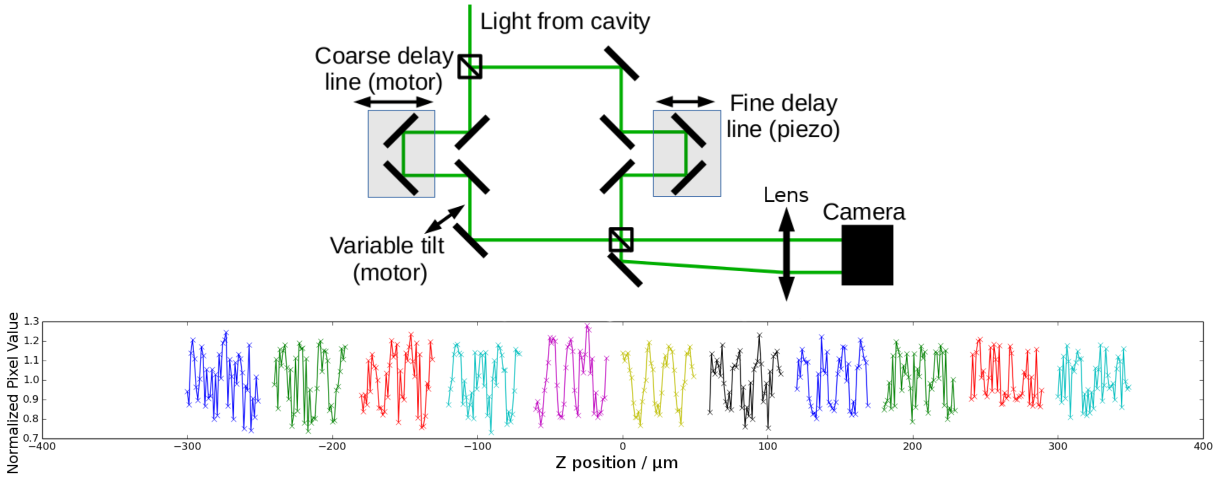

Figure 4.2: Top: Schematic of the Mach-Zehnder interferometer setup. Light is split by the first beam splitter. Each arm can delay or translate the light before recombining the beams at the second beam splitter. Both output ports are focussed onto the same camera in order to take images simultaneously. The coarse translation stage is driven by a motor on one arm while the fine translation stage by a piezoelectric driver on the other interferometer arm. Bottom: Interference fringes scanned with the fine translation stage plotted on the same axis but with different scales as the position of the coarse translation stage. The coarse position moves on a scale of 10 μm while the fine position moves only in steps of 100 nm. The fine position and coarse position are both plotted on the same x-axis but with different scales so that the shape of the fringes can be seen as well as the distance between them. Each new line colour on the graph is a different fringe at a new coarse stage position. Light from non-stabilized cavity. Each new line colour is a different fringe at a new coarse-stage position. The central fringes are clearer sine waves than the fringes at the edges, this is due to frequency noise from the cavity length jitter which was reduced with cavity stabilization measures.

4.2.2 Analysis

An image taken at an output of the interferometer we call an intensity image $I(x, y|Z_c, Z_f)$ taken at a given coarse Z_c and fine Z_f position, where Z is the path length difference noting that $Z = Z_c + Z_f$. By scanning Z_f we can step within individual interference fringes, from which the visibility at this given Z_c can be calculated. Caculating the visibility of each (x, y) pixel this gives us a so-called visibility image $V(x, y|Z_c)$ for the given coarse position Z_c. Visibility as a function of coarse position allows us to infer the coherence length, so we can obtain a coherence image which is an image where each pixel represents the coherence length at that point. Figure 4.5 is a diagram of this process. A final detail is that the raw camera image has red, green and blue channels, but we obtain the signal by summing red and green channel only as most of the interesting thermal cloud and photon BEC light is in these wavelengths.

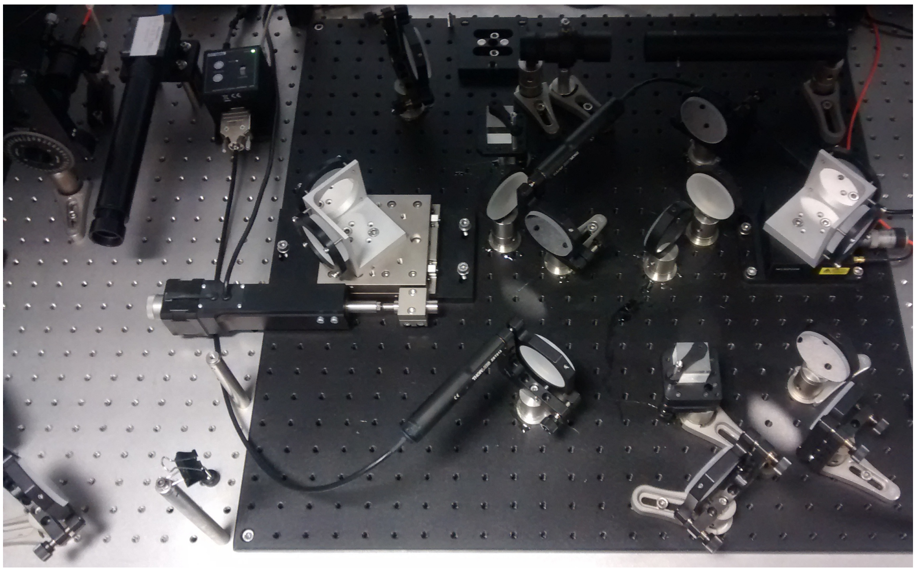

Figure 4.3: A photograph of the interferometer from August 2017. Light enters from the top, the coarse translation-stage is on the left, fine translation-stage is on the right. The output ports are on the bottom right and the camera is far left.

The wavelength of the fringe data is directly related to the wavelength of the incoming light. Figure 4.4 shows an interesting effect coming from this. The thermal cloud has a wavelength depending on radial position in a circularly symmetric way. This results in one cavity image at the output of the interferometer showing these rings of alternating maxima and minima of the fringes. We also show a cross-section image of a real spatial coordinate X plotted against the fine position Z_f to create a Z-fine / X image. We see lines of constant phase, where phase is $U(r)t/\hbar$ where the harmonic potential energy $U(r) = m\Omega^2 r^2/2$ and t is the relative time delay between the arms. This results in the parabolic shape seen.

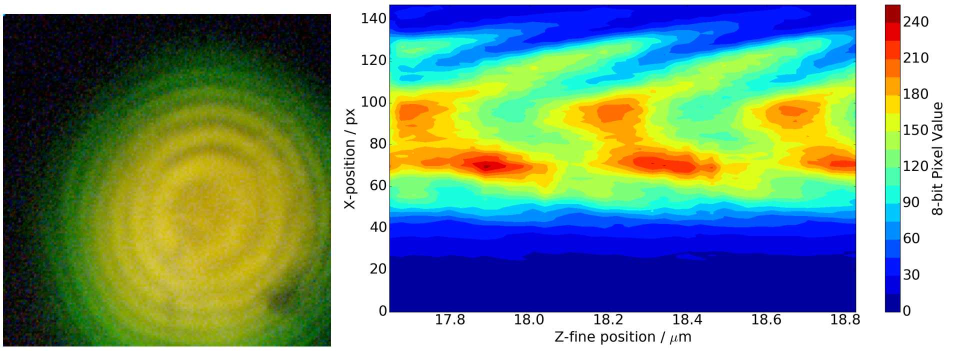

Figure 4.4: Left: The longest wavelengths (with less energy) are found at the cavity centre, with the wavelength dropping (and energy increasing) as the radial position increases. Results in ring shaped fringes on top of the cavity thermal cloud. Right: Z-fine / X image of a thermal cloud. In a thermal cloud the wavelength of a pixel depends on the position, wavelengths undergo constructive and destructive interference with different phases which results in the observed parabolic shapes.

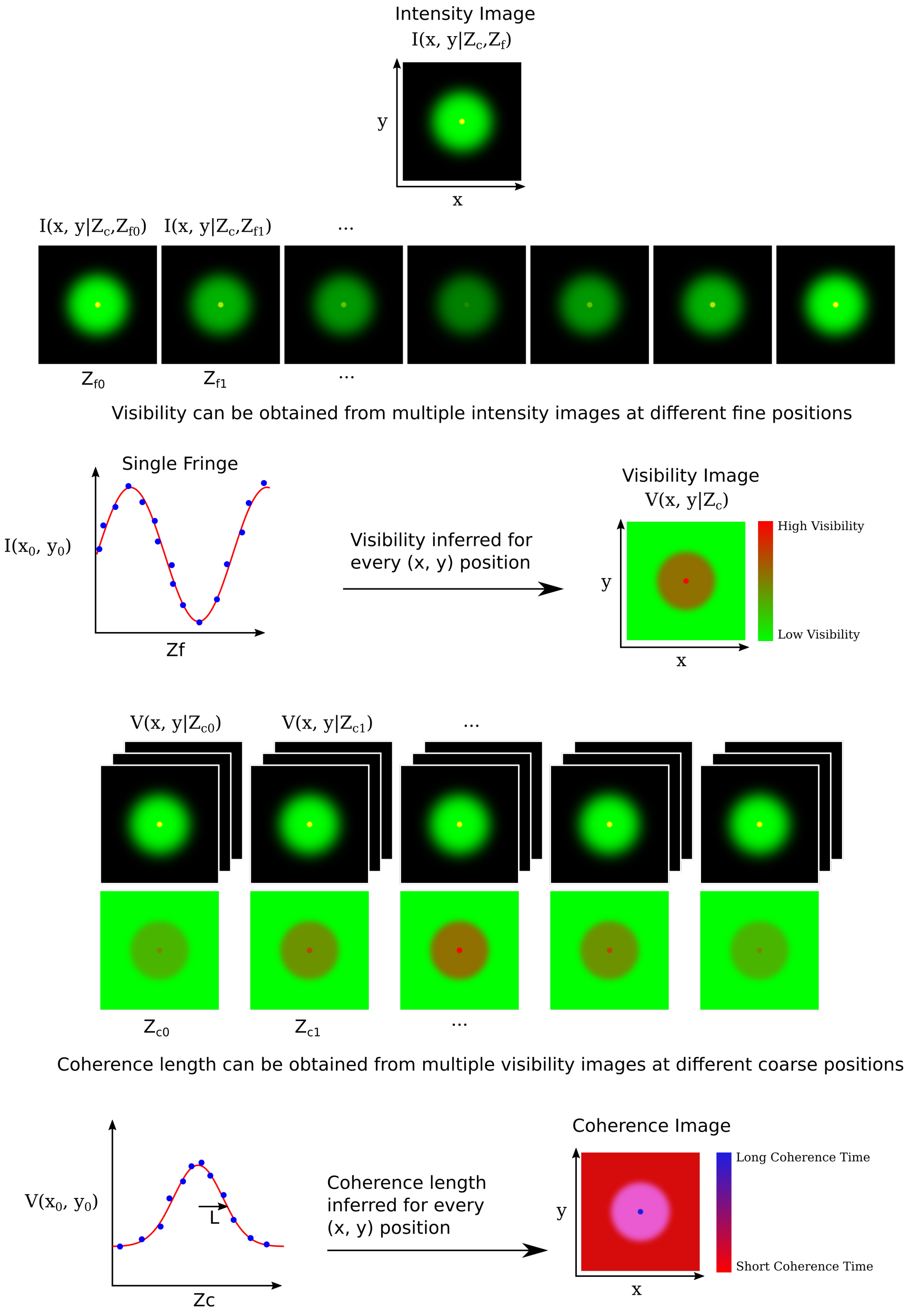

Figure 4.5: Diagram of the process of obtaining an intensity image at the output of the interferometer and using it to calculate the visibility by varying the fine delay Z_f, and from there obtaining the coherence length by varying the coarse delay Z_c. The process can be done for each pixel to obtain visibility images $V(x, y|Z_c)$ and coherence length images $L(x, y)$. The coherence in space as opposed to time delay is found in the same way except by varying the x-tilt mirror position which moves one arm image laterally relative to another.

In-Phase and Quadrature Output Image Overlapping

Both output ports of the interferometer are focused onto the same camera device. This guarantees the images are obtained at the same time without any complicated triggering electronics. A common origin for the two images must be found so that the same points in object space can be compared when calculating visibility and intensity. Before each set of measurements we block one arm of the interferometer so that the two output ports will be exactly the same image and not showing any interference, then we use an algorithm to find the origin where the images perfectly overlap. The algorithm works by minimizing a function of the differences in pixel values between the images squared. There is also an intensity scaling parameter representing the difference in intensity between the two images, which is usually fitted to be very close to unity. The form of the function is given in expression (4.16).

$$\min_{\delta x,\delta y,\alpha} \sum_{\text{Joint valid}x,y} \left[I^P(x,y) \;-\; \alpha I^Q(x-\delta x, y-\delta y)\right]^2 \tag{4.16}$$

where $x, y, \delta x, \delta y$ refer to image positions and shifts in the horizontal and vertical direction respectively. I^P, I^Q refer to intensities from the in-phase and quadrature output ports, and α is a scaling. The joint valid means that the sum will only be computed over the parts of the image which are present in both images I^Q and I^P after one is shifted. The global minimum is when the two images overlap by zero pixels, although the initial guess for minimizing the function is at $\delta x = \delta y = 0$ and to reach the zero-pixel-overlap the function would have to pass through high values of the difference squared. The point of overlap is therefore a deep local minimum.

Noise and Visibility

There is significant noise in the interferometer signal especially close to the BEC threshold. The noise is from numerous sources but a significant one is described in the Klaers et al.[40] theoretical paper on number fluctuations in photon BEC. The cavity light fluctuates in amplitude, frequency and phase. The fluctuations may also be indirectly caused by cavity length fluctuations or other instabilities. Regardless of the cause, the absolute signal value is often too noisy to directly feed into the Michelson criterion equation (4.12), as the max and min values are heavily dependent on single outlier noise readings. The noise causes a bias in the apparent coherence length.

The amplitude noise is correlated across the in-phase and quadrature outputs, so we decided on a measurement of the arctangent of their ratio. As in $I_{atan} = \arctan(I_P/I_Q)$. This corresponds to the angle of the phasor made up of the two outputs. Although not resulting in a purely a sinusoidal curve, we can still use it to extract the visibility. There are other sources of noise, namely frequency and phase noise, which are not removed by calculating the arctan and that would still give an incorrect visibility if naively inserted into equation (4.12). Therefore we settled on using a fourier analysis method of finding visibility.

The Fourier analysis method involves taking the first peak of Fourier transform and deriving from it the amplitude of the sinusoid. If $\hat{S}(\omega_0)$ is the Fourier transform of S at the first peak of frequency ω_0 then the visibility is $V = 2\hat{S}(\omega_0)/\hat{S}(0)$. The factor of two takes into account the identical peak at $-\omega_0$. The value $\hat{S}(0)$ is also equal to the mean.

The major frequency ω_0 is found using the autocorrelation of one of the fringes. The mean signal value is subtracted from the signal, which is then passed into the autocorrelation function which produces a smooth sinusoidal shape despite the noisy underlying signal. We do not use the well-known discrete fast Fourier transform algorithm because ω_0 may not be exactly in one of the discrete frequencies calculated. Instead we wrote a routine that calculated the Fourier transform directly for the region of frequencies around ω_0, which allowed us to find it with more precision. This straightforward method is equivalent to finding the Fourier transform of our signal multiplied by a rectangular window with width set by the size of the sample S, which in Fourier space results in the underlying Fourier components convolved with a sinc function.

Now the calculated visibility of the arctangent signal is not necessarily equal to the true underlying visibility we are interested in, so we wrote a Monte-Carlo simulation of data with many possible types of noise to find a mapping between the two visibilities. Figure 4.6 shows the resulting histogram from which the measured arctangent visibility can be converted back to the true visibility. The function converting between true and inferred visibility has a downwards bias at higher values, an underlying true visibility of 1.0 results in a mean inferred visibility of 0.8, however the function monotonically increases.

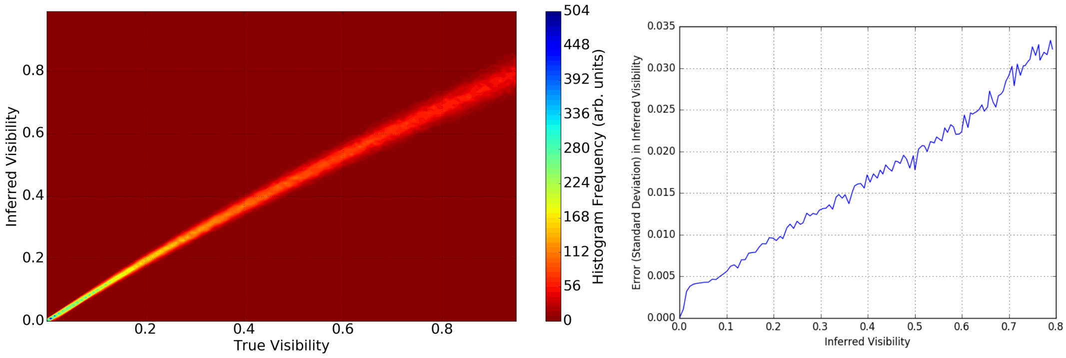

Figure 4.6: Left: Monte Carlo simulation histogram. Data of a given visibility is generated along with plausible models for noise. Our algorithm of finding the visibility of the arctangent is used to calculate the vertical axis and plotted against the underlying visibility. The colour gives the probability of inferring a given visibility when a given underlying visibility is put into the Monte-Carlo model. Right: Absolute error (standard deviation) of arctan visibility finding method from the same simulation.

Our model of the random noise influencing measurements in the simulation is described by equation (4.17). In the experiment we take camera data, measuring the intensity of pixels out of the in-phase and quadrature output ports of the interferometer. We model this as:

$$P = \left(A + \tilde{A}\right)\left(1 + \cos(\omega\tau + \phi + \tilde{\phi})\right) + \tilde{R_P} + offset \tag{4.17}$$

$$Q = \left(A + \tilde{A}\right)\left(1 + \sin(\omega\tau + \phi + \tilde{\phi})\right) + \tilde{R_Q} + offset \tag{4.18}$$

Variables with tilde overlaid are stochastic. $\tilde{P}$ and $\tilde{Q}$ are the in-phase and quadrature outputs. A and $\tilde{A}$ are respectively amplitude and amplitude noise, which follows a Poisson distribution expressing the graininess of measuring light photons. ω is frequency of fringes and τ is time delay. ϕ and $\tilde{\phi}$ are the phase and phase noise, which is normally distributed. $\tilde{R}$ is the normally-distributed readout noise that is added on top of the $offset$. By adjusting parameters we found that amplitude noise had very little effect on the calculated visibility presumably due to taking the ratio of Q and P. The readout noise increases the errors at low visibility. Phase noise was found to increase the total amount of error. The file `/Control/PythonPackages/interferometer_utils.py` in the project github repository contains all the interferometer analysis functions. Table 4.1 shows all the values of various parameters of the stochastic values used in the simulation.

Variable Symbol	Distribution	Parameter Value
$\tilde{A}$	Poisson	Amplitude = 0.2 A, $\lambda = 0.5$
$\tilde{\phi}$	Normal	$\mu = 0$, $\sigma = 0.2$
$\tilde{R_P}$, $\tilde{R_Q}$	Normal	$\mu = 0.1$ A, $\sigma = 0.1$ A

Table 4.1: The values of the various parameters of the stochastic parameters used in the simluation chosen so that the simulation results approximate what is seen in the experiment.

4.3 Results

4.3.1 Interference Fringes

A typical interference fringe is shown in Figure 4.7. It displays the quantity $S_{atan} = \arctan(S_P/S_Q)$ and is low noise as described in section 4.2.2. An image of a photon condensate just above threshold is shown as well as its visibility image and coherence length image. The colourmap has been chosen to show dim pixels more clearly, which results in very faint features being visible in particular the thermal cloud around the condensate. The visibility image shows very high visibility in the centre where the condensate is. The visibility is perceptible in the thermal cloud region and is essentially zero outside that. The coherence length image shows that the condensate has a uniform coherence length over its entire area indicating the entire condensate is coherent with itself, matching with other Bose-Einstein condensate systems.

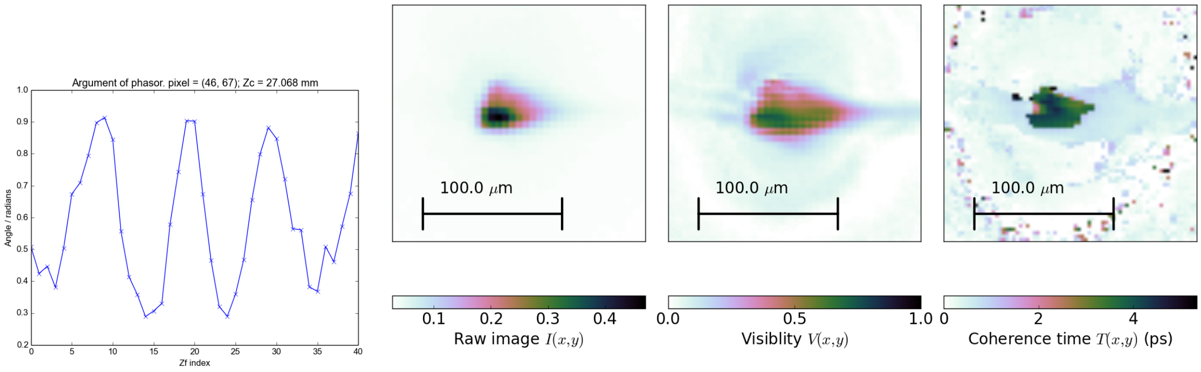

Figure 4.7: Left Image: A typical interference fringe showing a sampling of the fringe shape with sufficient data to infer the visibility. Right Images: Photon BEC just above threshold displayed in real space, as a visibility image and as a coherence length image. These three ways are described in section 4.2.2.

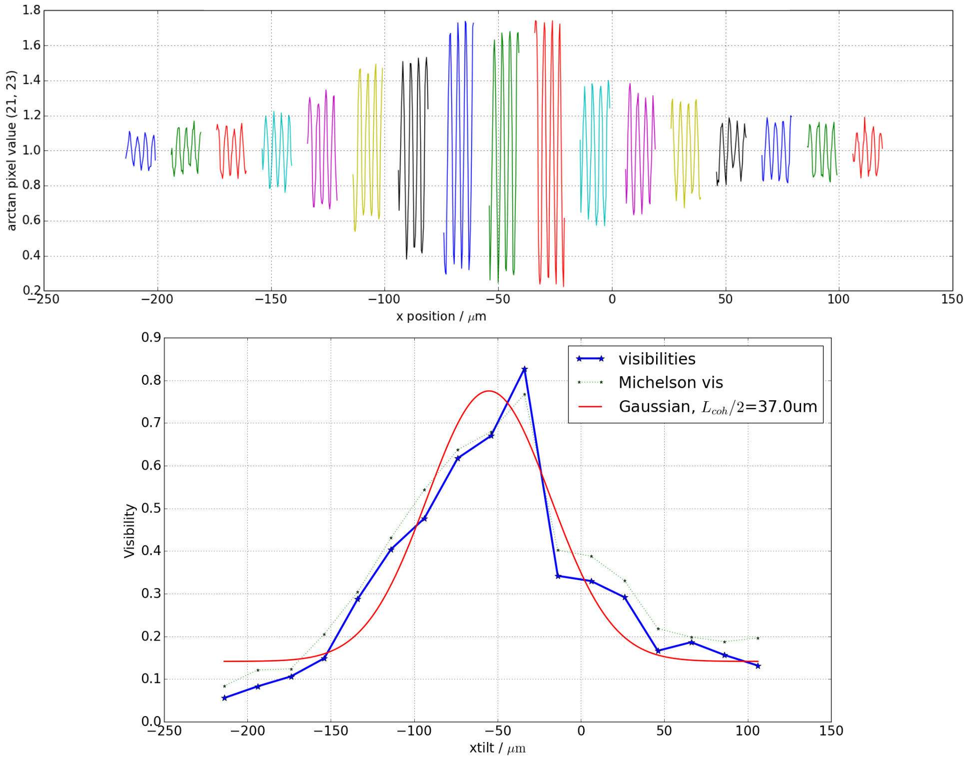

Figure 4.8: Spatial coherence. Top: Fine delay and coarse shift combined onto one graph. Interference fringes scanned with the fine translation stage plotted on the same axis but with different scales as the position of the coarse translation stage. Light from non-stabilized cavity. Each new line colour is a different fringe at a new xtilt position. The x-axis indicates the coarse shift of one image relative to another, while the coloured fringes indicate a small delay stepped over and used to measure the visibility. Bottom: Derived visibility fitted with a Gaussian curve. Michelson visibility (equation (4.12)) is also plotted which for these very clean fringes actually produces a good estimate.

Figure 4.8 shows a typical example of spatial coherence measured when one arm of the interferometer is shifted relative to the other. Very clear fringes can be seen and the coherence length matches the size of the condensate itself, suggesting that in this measurement the entire condensate oscillates with one phase. The visibility is fitted with a Gaussian curve.

4.3.2 Coherence

Figure 4.9 shows the coherence in space and time of the system above and below threshold. A single pixel is chosen to examine for visibility. The spatial displacement and time delay parameters are scanned on the same scales. The results show the coherence greatly increases above threshold. The coherence length of the thermal cloud is measured to be 4.5 μm which is limited by spatial resolution.

The coherence dramatically increases above threshold as is expected for BEC. The photon BEC coherence length is 14 μm which matches the size of the condensate itself, suggesting that coherence extends across the entire BEC, as is expected. Coherence time is 10ps, which was first believed to be limited by frequency noise resulting from poor mechanical stability of the cavity and implementing ideas from section 2.5 improved this.

Recently as this thesis was being written, another PhD student Ben Walker was using the interferometer to study microfabricated cavities that produce spatially smaller photon BECs. He discovered that the design of the interferometer reduces the coherence time. The root of the problem is that the two mirrors at right-angles mounted on the coarse translation stage do not correct for any vertical displacement; they are ‘corner squares’ not corner cubes. The coarse translation stage has a slight dip in the middle which shifts the image in one arm vertically when the stage is moved. This could be corrected by moving the tilting stepper motor to the vertical direction and compensating.

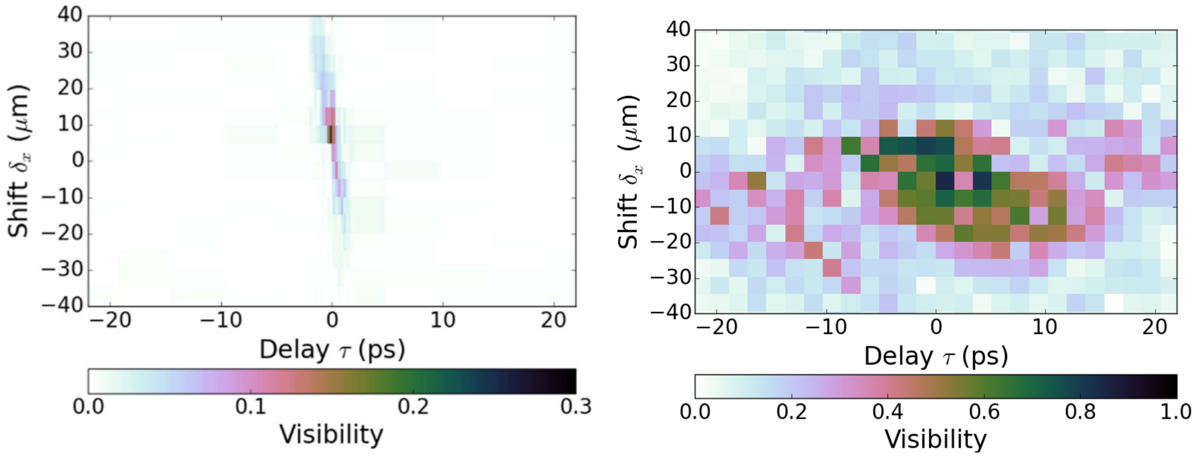

Figure 4.9: Visibility at a specific pixel at below-threshold thermal cloud (left) and above threshold photon BEC (right). Plotted on the same scale but with different visibility scales due to the much lower visibility below threshold. The fitted coherence lengths are 4.5 μm and 14 μm for thermal cloud and BEC respectively, the fitted coherence times are 0.2ps and 10ps.

A paper by Kohnen and Nyman[73] predicts that revivals may be visible. Revivals are where coherence rises again after certain delays. These revivals are not visible in our data.

4.3.3 Variation with Pump Power

Figure 4.10 shows the properties of the thermalized photons as power is varied. We show the shape (intensity) of the photon gas, as well as the visibility verses spatial shift, above and below threshold.

The measurements of scales of coherence and intensity were compared to theory, which assumes thermal equilibrium, absence of dissipation, and 2D symmetry in our Bose gas system. It starts from a well-established theory of correlations from Kohnen and Nyman[73] of a non-interacting trapped Bose gas at thermal equilibrum. The theory used is based on a series expansion in fugacity $\zeta = \exp(\mu\beta)$, $\beta = 1/k_B T$. The resulting non-normalised first-order correlation function is:

$$G^{(1)}(\vec{r}, \vec{r}', t - t') = \sum_{k=1}^{\infty} \zeta^k \prod_{s=x,y} K_s^{(k)} \left(s, s', t, [t' - ik\hbar\beta]\right) \tag{4.19}$$

Where the kth term in the expansion corresponds to the occupancy of up to k particles in a given mode. The function $K_s^{(k)}(s, s', t, t')$ represents the propagator along the s direction which depends on the trapping frequency, and is given in the Kohnen and Nyman paper[73] equation (20). The theory has no adjustable parameters. The expression can be normalised to obtain the first-order correlation function $g^{(1)}(\vec{r}, \vec{r}', t-t') = G^{(1)}(\vec{r}, \vec{r}', t-t')/\sqrt{G^{(1)}(\vec{r}, \vec{r}, 0)G^{(1)}(\vec{r}', \vec{r}', 0)}$. Below threshold with $\zeta < 1$ the series always converges, the finite series can also converge slightly above threshold given $\zeta - 1 \ll 1$ provided the number of particles is large. For this reason the model is only approximately valid above threshold. Below threshold (in the theory's range of validity) there is agreement between theory and data. The coherence grows as threshold is approached and then decreases far above threshold, at the same time as intensity scale keeps growing. This is due to multimode behaviour, as we shall see.

We now present results for the coherence time for a wider range of powers from far below threshold to just above threshold. The shape of the visibility curve will be Gaussian below and far above threshold and according to Kruchkov[68] will be a non-trivial shape near threshold. Nonetheless we use Gaussian fits to obtain values for coherence times which are plotted against pump power in figure 4.11. Far above threshold an upper bound of coherence time is set by the vibrations of the cavity length, and at higher powers the coherence actually drops in the multimode regime suggesting partial coherence between modes. As before the theory works best below threshold with only approximate validity just above threshold, theory does not match the data as well as in the spatial coherence case, but does match the qualitative increase at threshold. The theory underestimates the measured visibility due to the finite spatial resolution; filtering something will tend to increase the coherence length.

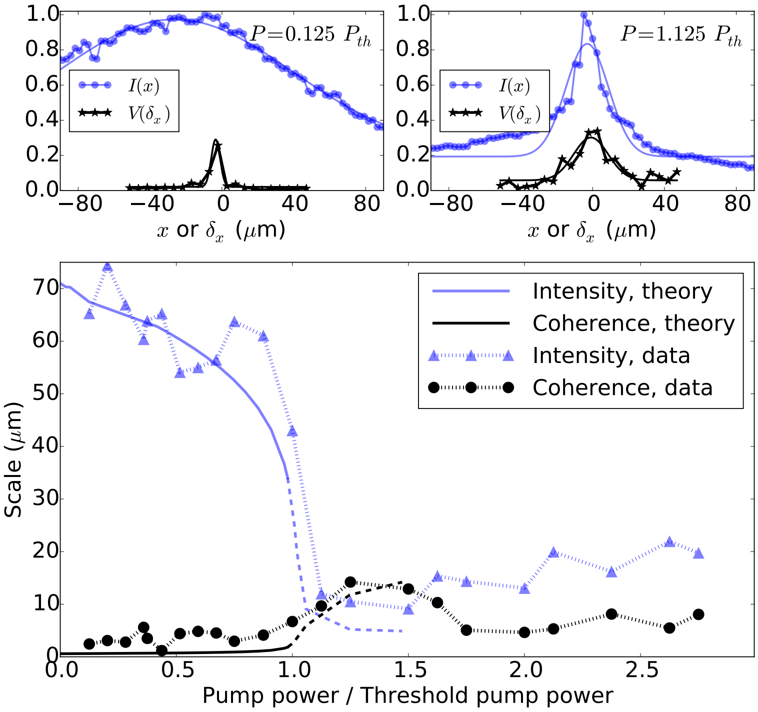

Figure 4.10: Top: Above and below BEC threshold data of spatial extent of thermalized photons, and visibility as a function of spatial shift between two interferometer arms. Taken at a given pixel and at zero time delay, with imperfect centering. Fitted to the gaussian function. Imperfect background subtraction results in offsets in the gaussian fits. Bottom: Width of intensity profile and coherence length as pump power is varied. Fitted to theory, where broken lines show regions where theory is only approximately valid. Finite spatial resolution effects are the likely cause of the theory underestimating measured visibility.

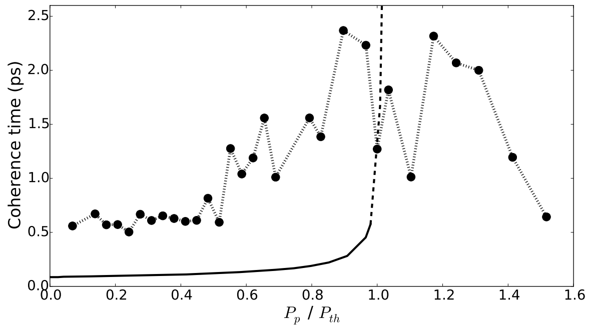

Figure 4.11: Coherence time variation by pump power, found by fitting to a guassian to the visibility against time delay. Line indicates theory from thermal equilibrium assuming no dissipation, which has only approximate validity at and above threshold.

Estimating Threshold Power

We estimate the threshold power using the variation of ground state population with pump power. We calculate the counts in a small circular region, which we use as an estimator for the ground state population. Figure 4.12 shows a bilinear fit (equation (4.20)) which can be used to deduce the threshold power, which in this case is 241 mW. We find that our central intensity measurement has a high uncertainty with a very small number of points near threshold which is likely caused by instability of the pump laser. Chapter 6 will expand on this treatment and create a stabilized laser power to improve this measurement.

$$I(p) = \begin{cases} a(p - p_{th}) + I_{th} & p < p_{th} \\ b(p - p_{th}) + I_{th} & p > p_{th} \end{cases} \tag{4.20}$$

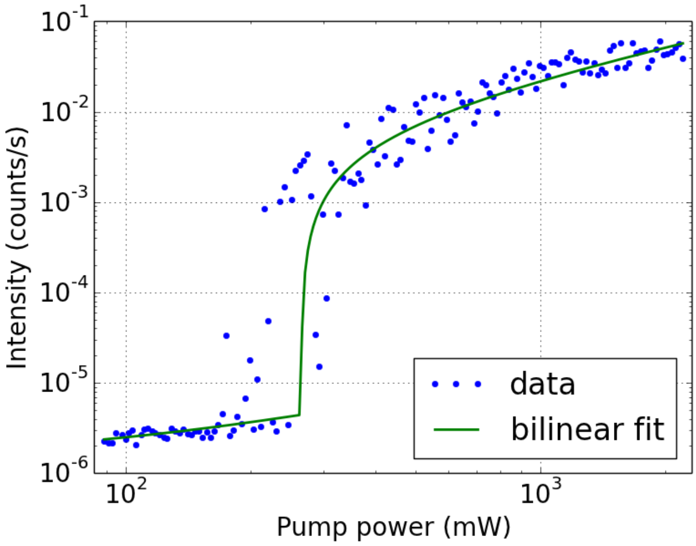

Figure 4.12: Bilinear fit for estimated ground state population verses power. Shows a good fit far above and below threshold but there are very few points and the data is less repeatable near threshold. The threshold power is fitted to 241 mW.

4.3.4 Multimode Condensate

At higher powers we observe the phenomenon of multimode condensation. Above a certain pump power other modes than the ground state mode will become macroscopically populated as well. Figure 4.13 shows the photon gas at three pump powers with the spectrum, intensity image and visibility image being shown. In multimode regimes the condensate width increases in space and the visibility image fragments. At higher powers the most occupied mode is not always the ground state, indeed that mode can be selected to a certain extent by moving the location of the pump spot. The shape of higher condensed modes also depends on details of the dirt in the cavity or damage on the cavity mirrors. The modes are incoherent with each other as can be seen from reduction in coherence in the multimode regime.

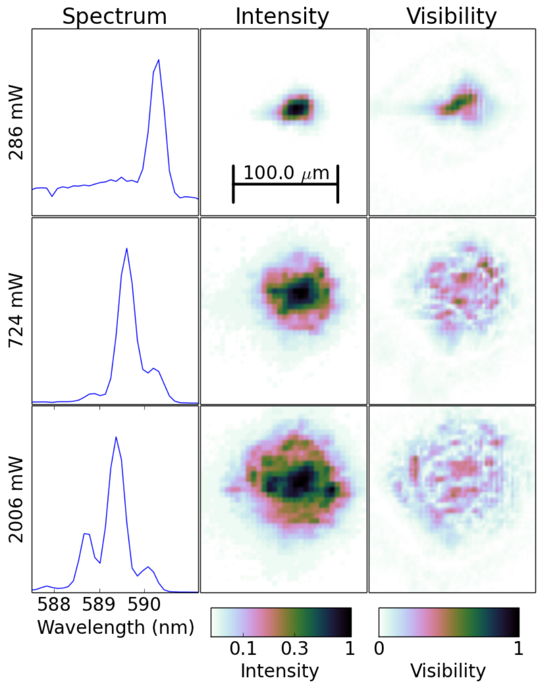

Figure 4.13: Photon BEC at three different powers taken at a small slightly-misaligned pump spot. Left: Spectrum showing transition from single mode to multimode and that the highest occupied mode is not necessarily the ground state at higher powers. Middle: Real space image of photon BEC which becomes broader in the multimode regime. Right: Visibility images which become fragmented in the multimode regime.

A theory of multimode photon BEC was created by Rob Nyman, Henry Hesten and Florian Mintert and it directly builds on Kirton and Keeling's model[54]. The fragmentation cannot be explained by a thermal-equilibrium process, which always produces a single condensate at the ground state mode. The theory is based on the idea of imperfect gain clamping of the excited-state fraction of dye molecules, and the spatial dependence of their interaction with the cavity modes. Figure 4.14 shows the results of this model. Increasing pump power past the threshold results in other excited state modes becoming macroscopically occupied (left panel). One mode reaching threshold will clamp the excited state dye population in its local area, there is still gain further away which allows more modes to reach threshold. A larger pump spot size allows for easier creation of multimode condensates because the spot is large enough to overlap several cavity modes (right panel).

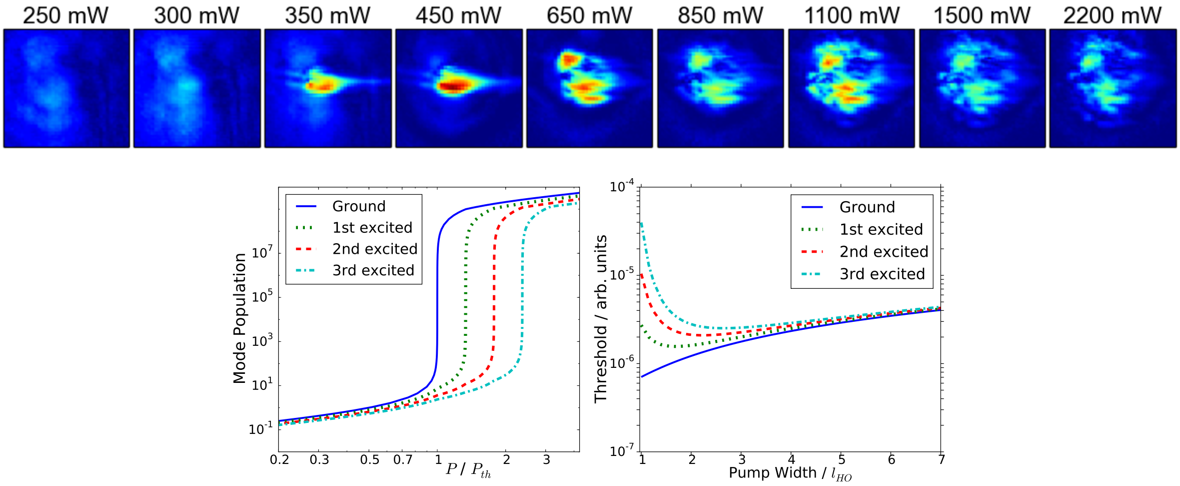

Figure 4.14: Top: Visibility images by power, showing the photon gas passing through BEC threshold (with threshold power $P_{th} = 350$mW) and into the multimode regime. Bottom: Results of a non-equilibrium model describing the multimode behaviour. Left panel shows how increasing the power causes excited state modes to become macroscopically occupied too. Right panel shows how large pump spots result in more multimode condensation happening close to the ground state threshold power. l_{HO} is the harmonic oscillator length scale and the left panel is simulated with a pump spot size of 2.2 l_{HO}.

4.4 Conclusion

In conclusion, we have observed the first-order coherence function in photon BEC using an interferometer. Spatial and temporal coherence is much higher above threshold as expected, although our interferometer underestimated the true coherence time and it was recently discovered how to fix this. We observe multimode condensation far above threshold. We have produced results which may be of interest to others investigating condensation phenomena and their coherence, such as exciton-polariton or atomic BEC groups.

Chapter 5

Momentum-Resolved Spectroscopy

5.1 Introduction

In this chapter we describe the 2-dimensional spectrometer experiment, from which we can obtain momentum- and position-resolved spectra. These spectra give us information of the phase-space distribution of the photon BEC system, as well as a measurement of the photon effective mass, interaction strength, potential energy landscape and coupling between photons and dye molecules. The results were published in our paper in Physical Review A in 2016[50].

5.1.1 Phase Space

Phase-space distribution is a concept from statistical mechanics describing the population at a given position and momentum. In a Hamiltonian (non-damped) system it contains all the relevant physical information about a gas when combined with energy as a function of position or momentum.

The light emitted from the photon BEC microcavity can be thought of as carrying information of the phase-space distribution $f\left(\vec{r},\vec{p}\right)$ at position $\vec{r}$ and momentum $\vec{p}$. Observing this light in different ways can be thought of as obtaining different views of $f\left(\vec{r},\vec{p}\right)$. One of the simplest views is a real-space image $n\left(\vec{r}\right)$ which is the phase-space distribution integrated over all momenta.

$$n\left(\vec{r}\right) = \int f\left(\vec{r},\vec{p}\right) d^2\vec{p} \tag{5.1}$$

Note that this analysis is for a two-dimentional system matching our photon BEC setup, but can be easily extended to higher dimensions. Similarly the population as function of energy (i.e. spectrum) can be found from the phase-space distribution by sampling it with a delta function where the phase-space local energy is matched.

$$n\left(E\right) = \iint f\left(\vec{r},\vec{p}\right) \delta\left[E - \epsilon\left(\vec{r},\vec{p}\right)\right] d^2\vec{p}\, d^2\vec{r} \tag{5.2}$$

In photon BEC, the local energy function is given by the kinetic energy T and potential energy V, as in $\epsilon\left(\vec{r},\vec{p}\right) = T\left(\vec{p}\right) + V\left(\vec{r}\right)$. Kinetic energy in this system is given by $T\left(\vec{p}\right) = \left|\vec{p}\right|^2/2m_{ph}$

and potential energy is determined by the cavity mirrors and given by $V\left(\vec{r}\right) = \frac{1}{2} m_{ph} \Omega^2 \left|\vec{r}\right|^2$ as demonstrated in section 1.5.
Interesting and relevant views into phase space for this chapter are the momentum-resolved and position-resolved spectra

$$n\left(\vec{p}, E\right) = \int f\left(\vec{r}, \vec{p}\right) \delta\left[E - \epsilon\left(\vec{r}, \vec{p}\right)\right] d^2\vec{r} \tag{5.3}$$

$$n\left(\vec{r}, E\right) = \int f\left(\vec{r}, \vec{p}\right) \delta\left[E - \epsilon\left(\vec{r}, \vec{p}\right)\right] d^2\vec{p} \tag{5.4}$$

Expressions for other views such as momentum image $n(\vec{p})$ and position-resolved spectrum $n\left(\vec{r}, E\right)$ can be found in the same way.

5.1.2 Simulation of Phase-Space Views

For distinguishable particles, the Boltzmann distribution, the most probable occupancy of states for a given position in phase space is given by:

$$f\left(\vec{r}, \vec{p}\right) = A \exp\left(-\frac{\epsilon\left(\vec{r}, \vec{p}\right)}{k_B T}\right) \tag{5.5}$$

where A is a normalization constant, k_B is the Boltzmann constant and T the absolute temperature. As before the local energy is given by:

$$\epsilon\left(\vec{r}, \vec{p}\right) = T(\vec{p}) + V(\vec{r}) = \frac{\left|\vec{p}\right|^2}{2m_{ph}} + \frac{1}{2} m_{ph} \Omega^2 \left|\vec{r}\right|^2 \tag{5.6}$$

We substitute these into equation (5.3) and solve the integral to obtain the momentum-resolved spectrum:

$$n\left(\vec{p}, E\right) = \begin{cases} A' \exp\left[-\frac{E}{k_B T}\right] & \text{, if } E > \frac{\left|\vec{p}\right|^2}{2m_{ph}} \\ 0 & \text{otherwise} \end{cases} \tag{5.7}$$

where A' is a constant set by normalisation. We can similarly obtain the position-resolved spectrum with another constant B':

$$n\left(\vec{r}, E\right) = \begin{cases} B' \exp\left[-\frac{E}{k_B T}\right] & \text{, if } E > V(\mathbf{r}) \\ 0 & \text{otherwise} \end{cases} \tag{5.8}$$

In practice this could be observed as an image on a camera by building a momentum-resolved spectrometer described in the rest of this chapter. There would exist a boundary between an area of darkness with zero counts and an area of data that follows an exponential decay. The boundary is the dispersion relation in the momentum-resolved case and is the shape of the potential in the position-resolved case.

Simulations of momentum- and position-resolved spectra are plotted in figure 5.1. The simulations solve equations (5.3) and (5.4) for momentum- and position-resolved spectra respectively. These result in plots following equations (5.7) and (5.8). The boundary line between the zero-population white area and the rainbow-coloured area is the shape of boundary between the two cases in the equations. For the momentum-resolved spectrum this is a dispersion relation and for the position-resolved spectrum it is the potential energy landscape. To provide a finite width in the simulation, the delta function is replaced with a Lorentzian with the damping κ:

$$\delta(a) \to \frac{1}{\pi}\frac{\hbar\kappa}{a^2+\hbar^2\kappa^2} \tag{5.9}$$

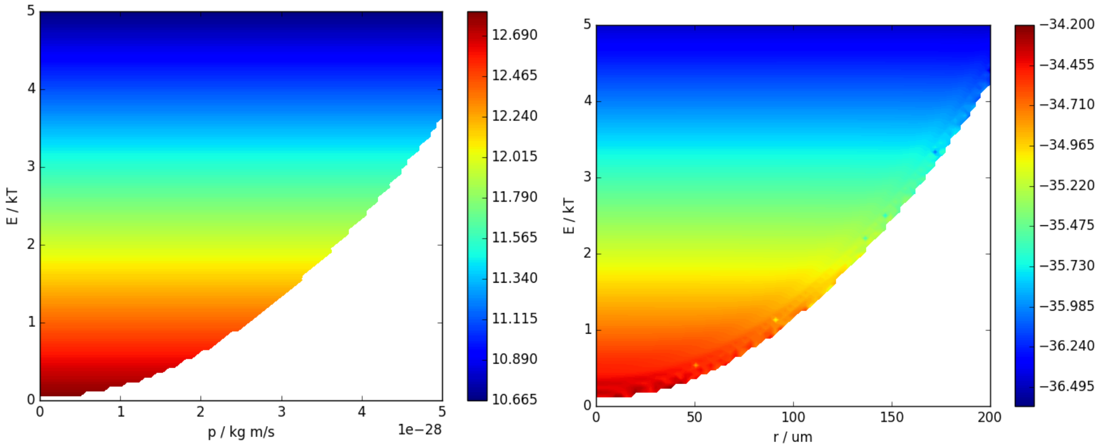

Figure 5.1: Plots of equations of momentum-resolved spectrum (Eq (5.7)) and position-resolved spectrum (Eq (5.8)) resulting from simulations. The boundary between the zero-population white areas and finite-population coloured areas matches the dispersion relation for the momentum-resolved case and matches the shape of the potential in the position-resolved case. Both are parabola shapes because of the quadratic dispersion of a massive particle and the quadratic potential due to the spherical mirror shape. Note that the intensity values are log-scales and the values have arbitrary units.

These measurements of views into phase space were also done by other BEC experiments such as exciton-polariton BEC[25, 70, 26]. They have a homogeneous potential instead of a parabolic potential as in photon BEC as in figure 5.2; meaning the equation (5.3) is solved with a constant potential energy, which results in the same parabola shape but not filled in. Introducing another normalisation constant A'', it is described by equation (5.10)

$$n(\vec{p},E) = \begin{cases} A'' \exp\left[-\frac{E}{k_B T}\right] & \text{, if } E = \frac{|\vec{p}|^2}{2m_{ph}} \\ 0 & \text{otherwise} \end{cases} \tag{5.10}$$

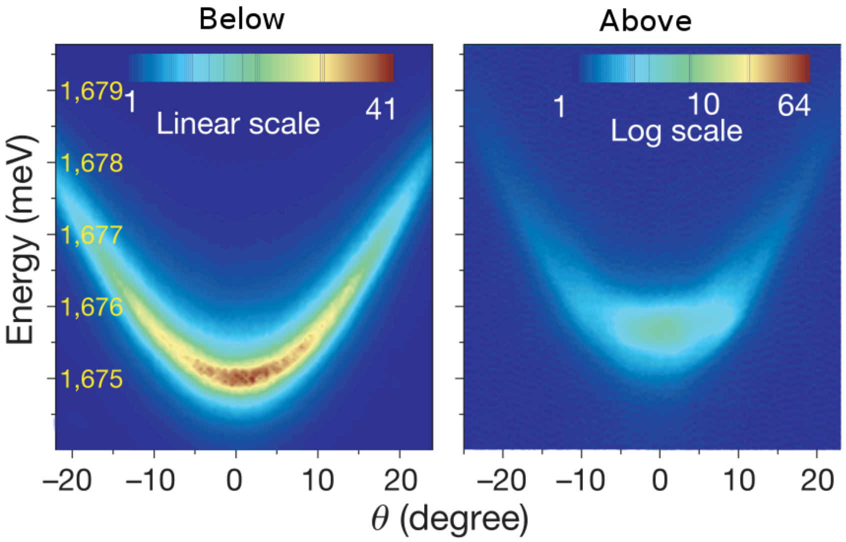

Figure 5.2: Momentum-resolved spectrum from the Kasprzak exciton-polariton BEC paper[25] above and below threshold. The angle on x-axis refers to emission angle and is therefore proportional to the in-plane momentum. As in the photon BEC case, the dispersion relation can be observed from the boundary between the data and dark regions. The plots show a parabolic dispersion relation matching a massive particle.

5.1.3 Dispersion Relation of a Bose Gas

Any nonlinear interaction effects would give rise to deviations from the parabolic dispersion relation shape. In the case of Bogoliubov sound waves, the dispersion would be linear near the bottom of the parabola around zero momentum. The strength of interaction effects giving rise to Bogoliubov dispersion is described by the interaction parameter g.

The Nyman and Szymanska paper[33] on interactions in photon BEC proposes an experimental apparatus for measuring the momentum-resolved spectrum and finding the interaction strength (note that the setup in the paper turned out to require some modifications). The paper considers the precision of measurement under realistic experimental conditions and finds it would be possible to resolve the dimensionless interaction parameter $\tilde{g}$ of order 10^{-5} which is two orders of magnitude below current estimates. The paper discussed likely origins of interactions which could be the nonlinear Kerr effect or thermal lensing. The measurement of dispersion relation $E = p^2/2m_{ph}$ also allows measurement of the effective mass m_{ph}.

What follows is a brief theoretical treatment to show how a nonlinear interaction $\tilde{g}$ gives rise to the dispersion relation for Bogoliubov excitations. This treatment is taken from my undergraduate lecture notes[74]. We start with the Gross-Pitaevskii equation or non-linear Schrödinger equation which describes the condensate wavefunction ψ_c of a Bose-Einstein condensate without pumping or loss and with nonlinear interaction strength g, we also give the formula for converting to the dimensionless interaction parameter $\tilde{g}$:

$$i\hbar\frac{\partial\psi_c}{\partial t} = \left[V(\vec{r}) - \frac{\hbar^2}{2m_{ph}}\nabla^2 + g\left(|\psi_c|^2 - \bar{n}\right)\right]\psi_c \tag{5.11}$$

$$g = \frac{\hbar^2}{m_{ph}}\tilde{g} \tag{5.12}$$

Where $\bar{n}$ is the average particle density and $V(\vec{r})$ is potential as a function of position $\vec{r}$. The equation is converted to dimensionless form by dividing by $\bar{n}^{3/2}g$, we define the Healing length $\xi = \sqrt{\hbar^2/m_{ph}\bar{n}g}$ as the characteristic length of the system and $t_0 = \hbar/\bar{n}g$ as the characteristic time. The dimensionless length $\vec{\rho} = \vec{r}/\xi$ and time $\tau = t/t_0$ are used. We set the wavefunction to be a stationary ground state $\psi_c/\sqrt{\bar{n}} = \eta(\vec{\rho},\tau)\exp(i\theta(\vec{\rho},\tau))$ where both η, θ are also dimensionless. Denoting nabla in these units with $\tilde{\nabla}$ gives us a dimensionless form of the Gross-Pitaevskii equation:

$$\frac{\partial}{\partial\tau}\left(\eta e^{i\theta}\right) = -\frac{1}{2}\tilde{\nabla}^2\left(\eta e^{i\theta}\right) + \left(\eta^2 - 1\right)\eta e^{i\theta} \tag{5.13}$$

Now we multiply both sides by $\eta e^{-i\theta}$ and equate imaginary (equation (5.14)) and real (equation (5.15)) parts.

$$\eta\dot{\eta} = -\eta(\tilde{\nabla}\eta)\cdot(\tilde{\nabla})\theta - \frac{\eta^2}{2}\tilde{\nabla}^2\theta \tag{5.14}$$

$$-\eta^2\dot{\theta} = \frac{1}{2}\eta^2(\tilde{\nabla}\theta)^2 - \frac{\eta}{2}(\tilde{\nabla}^2\eta) + (\eta^2 - 1)\eta^2 \tag{5.15}$$

The equation resulting from the imaginary parts can be shown to be equivalent to the continuity equation of conservation of particle number. We then make a small density perturbation $\psi_c = \left[\sqrt{\bar{n}} + \delta n(\vec{r},t)\right]e^{i\theta}$ or in dimensionless units $\eta = 1 + \frac{\delta n}{\sqrt{\bar{n}}}e^{i\theta} = 1 + \delta\eta$ and substitute into equation (5.15) resulting from the real parts, and keep only the first order terms.

$$-\dot{\theta} = 2\left(1 - \frac{1}{4}\tilde{\nabla}^2\right)\delta\eta \tag{5.16}$$

This is an equation with two unknowns, θ and n. Substitute the same perturbation into the continuity equation (5.14) to find $\delta\dot{\eta} = -\tilde{\nabla}^2\theta/2$ which can be used to eliminate η resulting in a fourth-order linear partial differential equation, shown here in dimensionless and dimensionful forms.

$$\ddot{\theta} = (1 - \frac{1}{4}\tilde{\nabla}^2)\tilde{\nabla}^2\theta \tag{5.17}$$

$$\frac{\hbar^2}{g^2\bar{n}^2}\frac{\partial^2}{\partial t^2}\theta = \xi^2\left(1 - \frac{\xi^2}{4}\nabla^2\right)\nabla^2\theta \tag{5.18}$$

We try a wave-like trial solution $\theta\left(\vec{r},t\right) = \sum_k \theta_k e^{i\left(\vec{k}\cdot\vec{r} - \omega t\right)}$ and obtain a dispersion relation:

$$\omega_k^2 = \frac{g\bar{n}}{m}k^2\left(1 + \frac{k^2\xi^2}{4}\right) \tag{5.19}$$

which as described previously is a parabola shape at large wavevectors/momenta but linear close to the origin. It is also possible to find the velocity of the waves using $V_s = \frac{\hbar}{m}\nabla\theta$ to find that the fluid motion is in the same direction as the wave motion, meaning these are longitudinal waves matching the picture of these excitations as sound waves. Bogoliubov excitations have been observed in exciton-polariton condensates[75] and are shown in figure 5.3; which shows measurements of the dispersion relation with and without interactions, the case with interactions shows a much more linear dispersion relation than without near the origin indicating Bogoliubov sound waves.

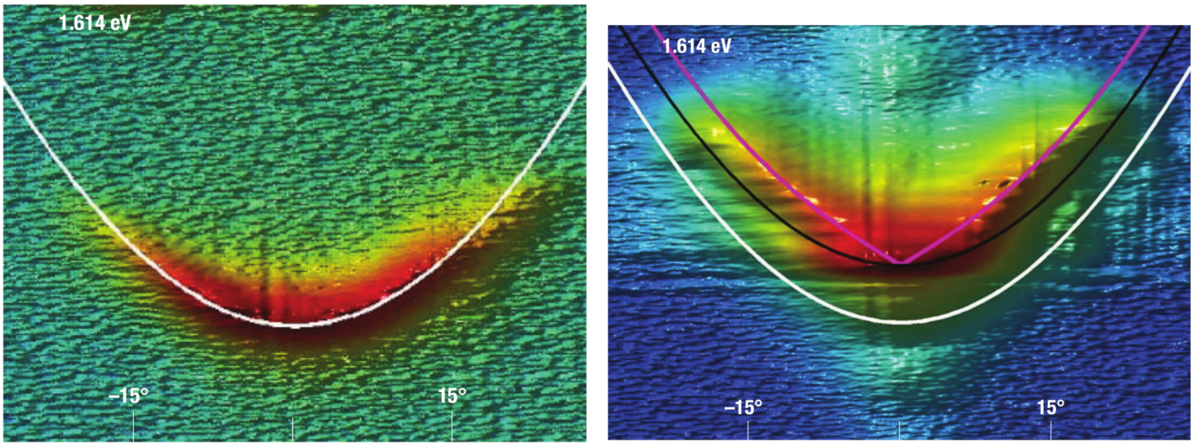

Figure 5.3: Linear intensity plot of energy-momentum spectrum showing Bogoliubov excitations observed in exciton-polariton condensates[75]. x-axis is momentum and y-axis is energy. Left: Parabolic dispersion relation for system below threshold. Right: Bogoliubov dispersion relation showing linearity close to zero-momentum and parabola at larger momenta.

5.2 Setup

5.2.1 Optical Setup

To recap optical theory and the Fourier transforming property of lenses: if a transmissive object is placed one focal length in front of a lens, then its Fourier transform will be formed one focal length behind the lens[76]. This can also be thought of as the lens causing ray positions to be converted to ray angles, in other words all positions are focused to the same angle and all angles are focussed to the same position. In the photon gas cavity experimental setup, angle corresponds to momentum so this Fourier transform property can be used to access the momemta of photons.

The optical setup is shown in figure 5.4, it involves building a 2D spectrometer that can be configured for momentum- or spatial-resolution; what follows is a description of the momentum-resolved spectrometer which can be reconfigured into a real-space one. The cavity emission light is imaged to infinity by an objective lens. There is a graticule of 800μm pitch printed on clear plastic acetate on a flip-mount which is used for calibration. The light is then split by a beamsplitter with one half sent to a diagnostic camera and spectrometer, the rest of the light is directed to the 2D spectrometer. The first lens of a 1:1 telescope creates a momentum-space image and a slit is placed there to choose a narrow band of momenta. The slit chooses a single momentum in the x-direction and is mounted on a three-direction translation stage with a flip-mount. After the telescope there is flip-mirror for choosing whether the light goes to the imaging camera or to the blazed grating. The grating splits the image of the slit by wavelength (or energy). Then two cylindrical lenses focus the energy and momentum components separately onto the camera.

5.2.2 Image Processing and Calibrating Energy

The calibration of energy is done by first lengthening the cavity to about 100 longitudinal mode numbers to produce a frequency comb. A series of parabolas are produced each corresponding to a longitudinal cavity mode. Image processing is used to find the apex of each parabola and its pixel is matched to a spectrum taken simultaneously with a spectrometer calibrated by the manufacturer.

A few techniques of image processing are used. To find the boundary of the data (which is typically in a parabola shape) we use the flood fill algorithm. Flood fill is the same algorithm used in the 'bucket fill' tool in image software like Photoshop. It works by starting from a single pixel and recursively spreading outwards stopping only when it reaches a boundary however that is defined. In our parabola-finding situation the boundary is a threshold in pixel value below which we judge there to be no data. After the flood fill is completed we have a list of all pixels that make up the non-zero pixel values of the data, as well as a list of boundary pixels which we can use to fit the parabola shape. Another image processing technique used was to take slices of the image along the x-axis (energy), smooth it and take the derivative of the pixel values. The parabola-shaped boundary that follows the dispersion relation or the potential energy landscape appears as a peak in these slices, finding these peaks can also be a way of fitting the shape of the parabola.

Figure 5.5 shows through images the energy calibration process. The calibration is nearly linear with the gradient varying by no more than 10% across the image. The figure shows the raw image from the spectrometer camera showing several parabola-shaped data regions, one for each cavity longitudinal mode. The next subfigure is this same image after image processing to find the parabola boundary and fit it to a quadratic equation, which is used to derive the pixels co-ordinates of the parabola apex. These pixels are matched with data from the commercial spectrometer from which a calibration between pixel and wavelength/energy can be found.

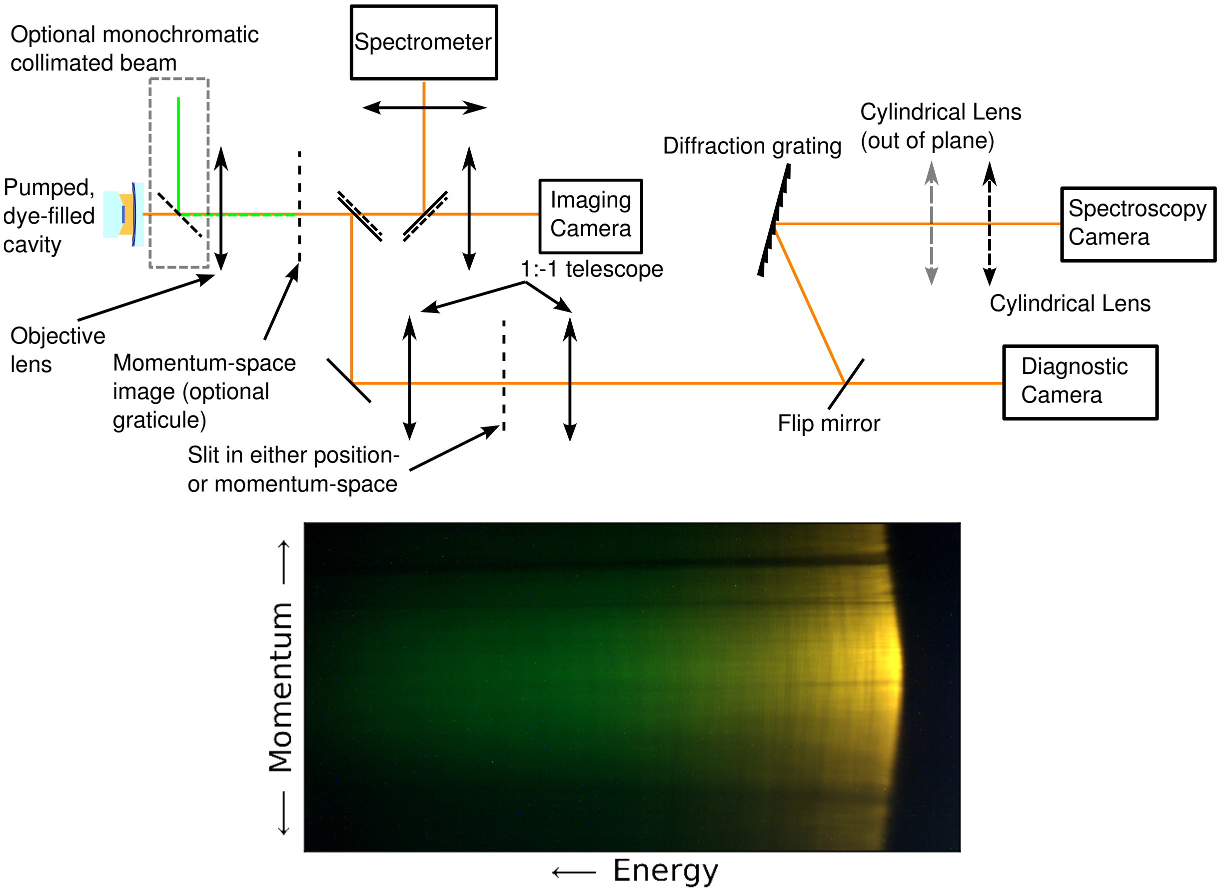

Figure 5.4: Top: Momentum- or position-resolved spectrometer setup. The cavity light passes through a 800μm pitch graticule printed on transparent acetate which can be flipped out. A beamsplitter is used to send half the light to the regular camera and spectrometer, while the other half goes to the 2D spectrometer. A 1:1 telescope with a slit placed in either momentum or real space is used to choose a narrow band of either momenta or area. A flip mirror is used to direct the light either to a diagnostic camera for producing, for example, momentum-space images; or to the grating. The grating has 1800 lines-per-millimetre and splits the light into different wavelengths. Cylindrical lenses are used to separately focus the energy and position/momentum onto the camera. A bypass mirror can be optionally placed to send a monochromatic collimated beam down the beamline used for aligning. Bottom: Typical momentum-resolved spectrum image in real colour.

5.3 Momentum-Resolved Spectrum

5.3.1 Aligning and Calibrating Momentum

The 2D spectrometer is a multi-component optical system and aligning it is a non-trivial task. We make use of the optional monochromatic collimated laser beam after the cavity. This beam is a single-angle (momentum) single-wavelength (energy) light source. The aligning steps happen from the cavity going down-beam. Not shown in figure 5.4 are two mirrors mounted on magnetic bases which can be removed to bypass the telescope. The following procedure is used on an already-existing photon BEC setup:

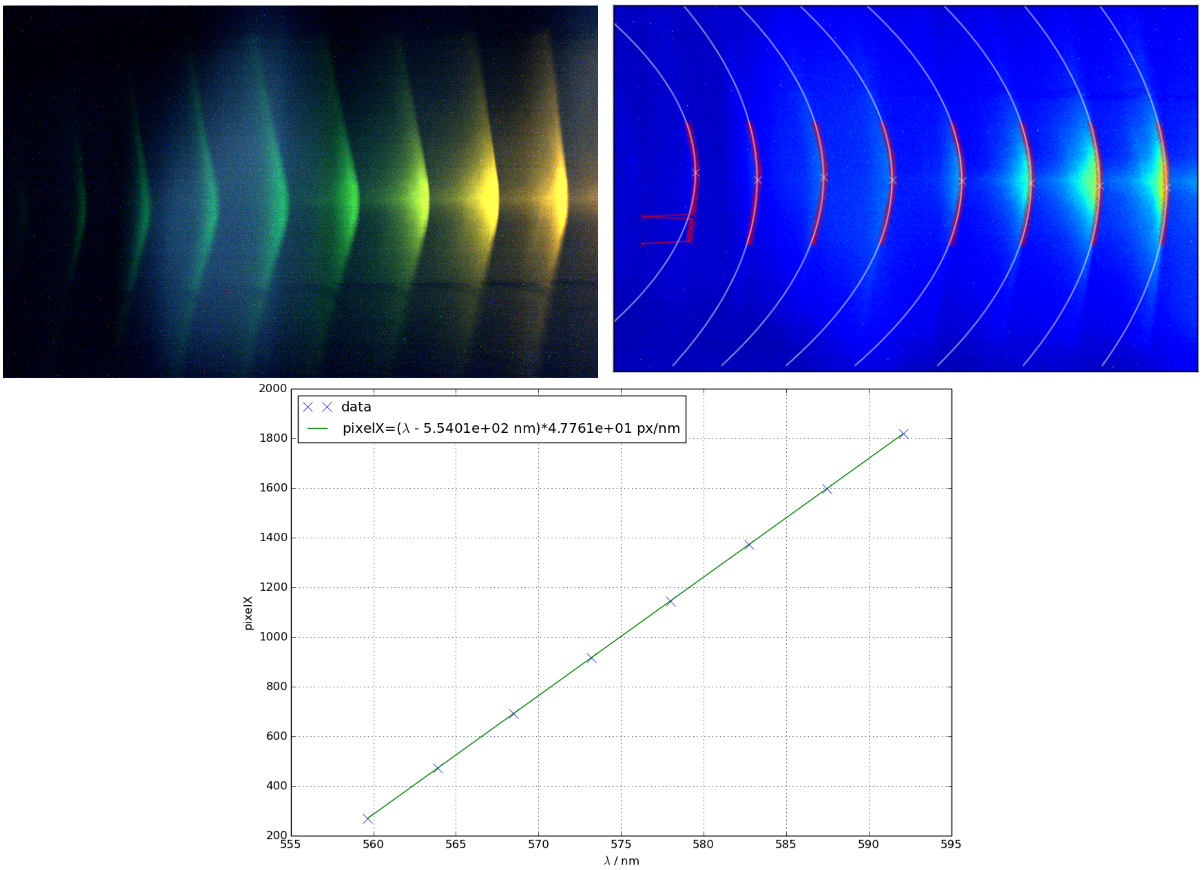

Figure 5.5: Top Left: Raw image from 2D spectrometer camera, with levels, brightness and contrast modified to display better. Shows several parabolas corresponding to longitudinal modes of the cavity. Top Right: Parabolas found by detecting the sharp change in pixel value, fitted with the apex marked by a white cross. Bottom: Energy calibration showing a linear fit between pixel and wavelength/energy.

1. Remove bypass mirrors and focus real-image on diagnostic camera so it looks the same as image on imaging camera. The edge of the small cavity mirror can be used as a sharp feature to focus on.
2. Replace bypass mirrors and focus 1:1 telescope so that the image on diagnostic camera looks the same as before.
3. Place the flip mirror to guide the collimated laser beam behind the cavity.
4. Place the telescope slit at the position where the collimated laser beam is focussed, this is the momentum image.
5. Remove the collimated beam and create a thermal cloud. Flip out the telescope slit. Align the output beam onto the camera via reflecting off the grating with a first-order reflection.
6. Rotate the slit 90° so it is in the perpendicular direction to the grating lines. This creates a

horizontal line on the spectrometer camera, focus this line using the momentum cylindrical lens to make it as narrow as possible. Rotate the slit back afterwards.

7. Create a photon condensate to provide a light source at the ground state energy at zero momentum. Move the telescope slit left-right until the condensate is visible on the spectroscopy camera.

8. Adjust the diagnostic camera to have the image of the slit focussed on it, this means the camera is in momentum space. Moving the pump spot in an extended cavity should not move the location of the gaussian shape in the momentum image, but would in a real-space image.

9. The graticule is placed in momentum space after the objective lens by watching for when its lines appear in-focus on the diagnostic camera. In practice large tolerances in the position of the graticule will work.

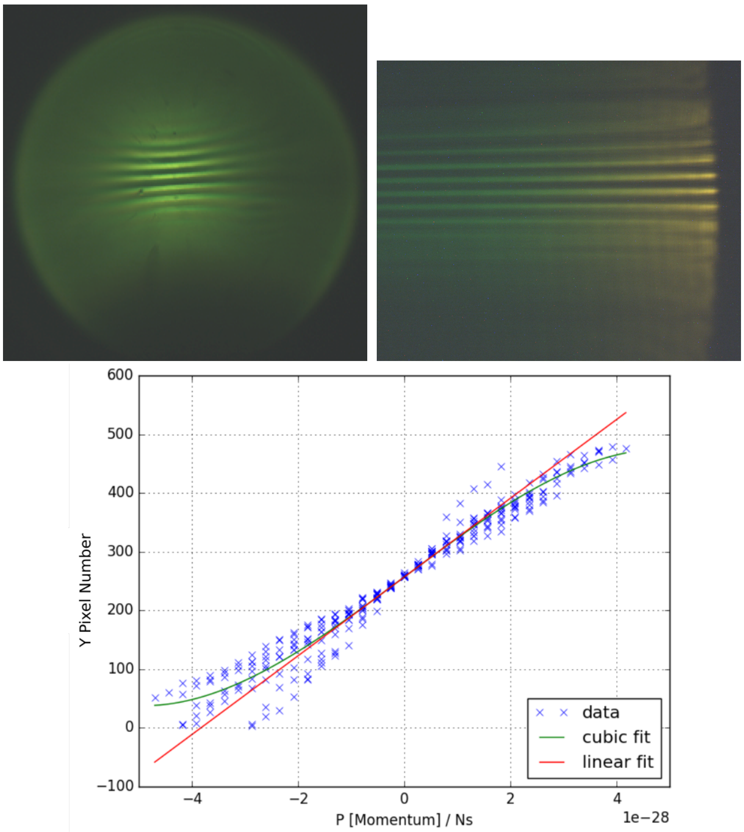

Figure 5.6: Momentum space image (left) and momentum-resolved spectrum (right) with the calibration graticule of pitch 400 μm in place. Both images show pincushion distortion typical of spherical abberations. The momentum-resolved spectrum has energy on the X-axis and momentum on the Y-axis The calibration (bottom) is found by finding the location of the lines in the Y-direction caused the graticule which is the Y-pixel number. This is fitted to a cubic curve against momentum to model the distortion and taking only the linear part near the origin.

A similar procedure is used to align for a spatial-resolved spectrometer. The known pitch of the graticule allows calibration of momentum. Figure 5.6 shows a momentum-space image on the diagnostic camera and an energy-momentum spectrum, both with the graticule in place. The distortions of the parallel lines also show the limits of calibration. We plot the pixel number of the bright lines against the momentum and fit to a cubic to model the pincushion distortion. The linear part of the resulting cubic is the calibration in the non-distorted central region. The momentum resolution limits are set by the spherical aberrations, the achromatic doublets give distortions for angles greater than about 35 mrad which is equivalent to 4×10^{-29} Ns which matches where the distortions are visible.

5.3.2 Results

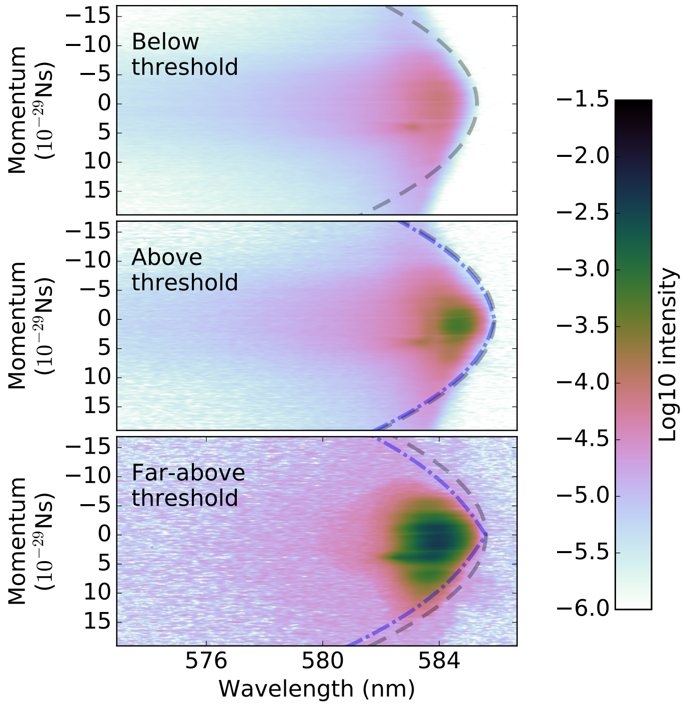

Figure 5.7: Momentum-resolved spectra for below, above and far-above threshold. Dashed lines correspond to quadratic dispersion relation (grey) and Bogoliubov dispersion relation (blue) with a dimensionless interaction parameter that is consistent with other measurements. A Bogoliubov dispersion relation is not plotted below threshold because it does not make sense for a thermal cloud. Far above threshold the multimode phenomenon of BEC changes the shape as shown.

Figure 5.7 shows momentum-resolved spectra for three regimes of pump power. The images are false-colour with background subtracted by method of taking a background image with the AOM in the off state not allowing the pump light through. The grey dashed lines show a quadratic dispersion relation corresponding to an effective photon mass of 7.8×10^{-36} kg. The blue-dashed lines show a Bogoliubov dispersion relation with a dimensionless interaction parameter $\tilde{g} = 10^{-4}$, which sets an upper-bound that is comparable with other measurements of between 7×10^{-4} measured by the Weitz group[36] and 5×10^{-7} inferred by the Stoof group[58] in Utrecht using Weitz group data. From this we conclude that we have measured an upper-bound on the interaction strength which is compatible with observations from other groups.

Figure 5.8 shows fits for each momentum of equation (5.7), the theory momentum-resolved spectrum below threshold. The temperature is directly related to the exponential decay constant of the fit, and is found to be independent of momentum but dependent on the pump spot size. The differing pump spot sizes can be used to degrade thermal equilibrium, the constant temperature fit at every momentum means that ergodicity is still respected, i.e. the system has had time to travel through every point in phase space, the distribution in terms of energy alone is enough to describe it. The distortions in the momentum space as seen in figure 5.6 do not affect the temperature fitting as the energy scale is much less distorted.

Figure 5.9 shows momentum-resolved spectra, real-space images and spectra for several pump powers. We can see how in the multimode regime that several modes at higher energies than the ground state are clearly visible on the spectrum at the higher powers, which extend out to higher momenta. As before the real-space image of the condensate also becomes wider and more peaks are visible on the emitted spectrum although there is saturation of the spectrometer at higher pump powers. The energy resolution of the momentum-resolved data is higher than other data such as figure 5.7 due to greater care taken when aligning, as can be seen with fine features in the multimode regime. However the energy and momentum scales are un-calibrated.

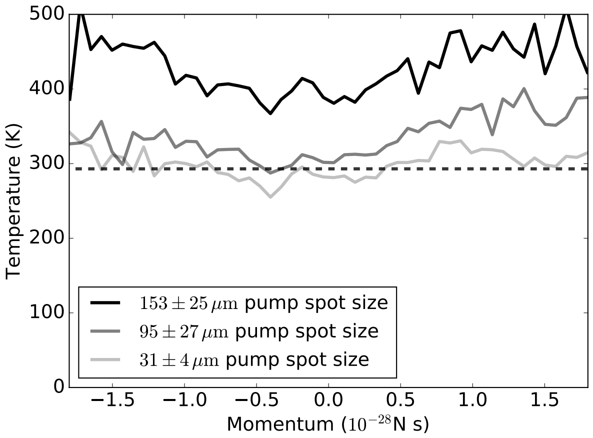

Figure 5.8: Energy scale fit for temperature at each momentum. Lower pump spot sizes show rough match to room temperature while the large spot size does not, meaning thermal equilibrium is degraded at large sizes. The approximately constant temperature fit implies that the system is always ergodic even when it is not at thermal equilibrium.

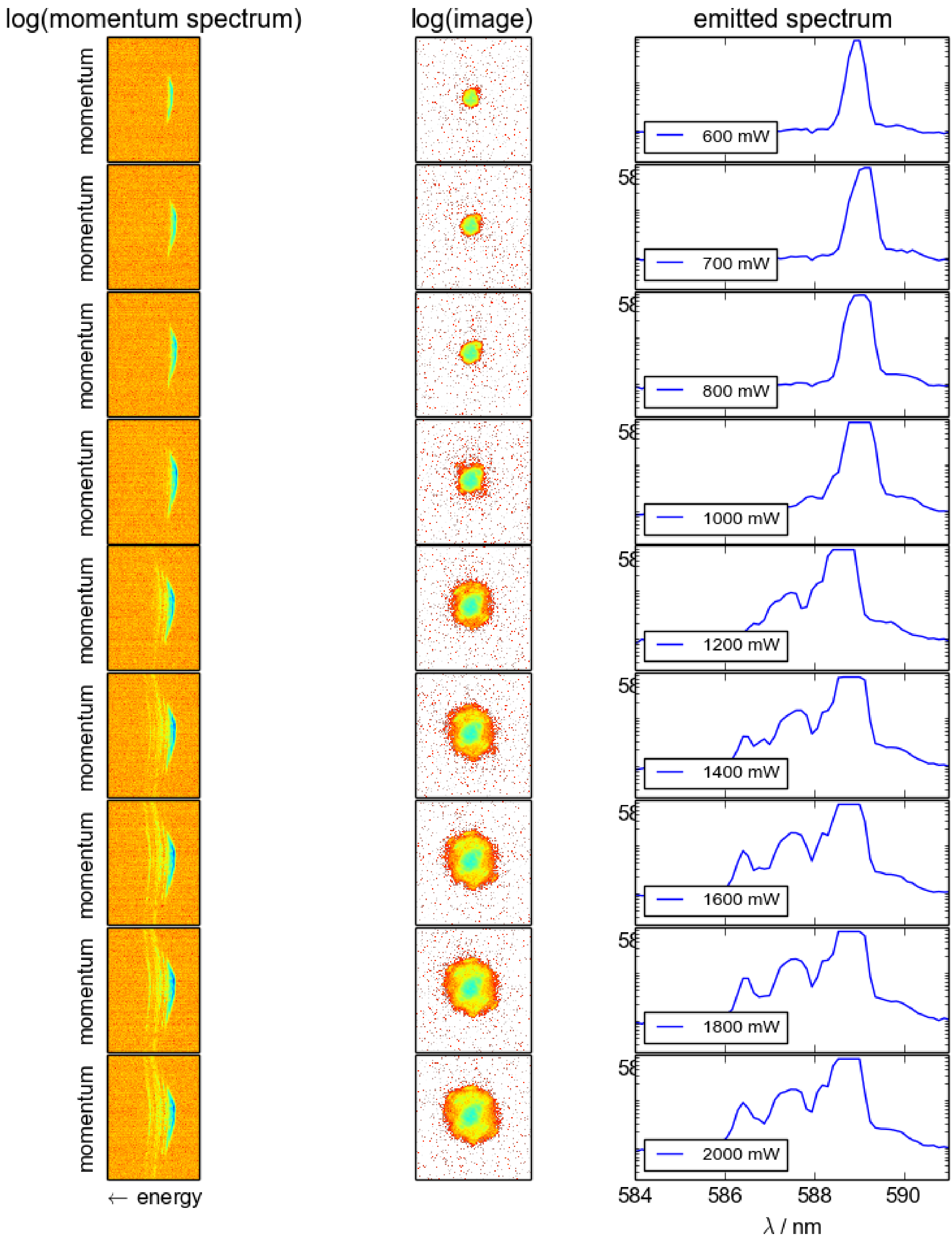

Figure 5.9: Shows momentum-resolved spectra, real space images and normal spectra for several pump powers. Above about 1200 mW the condensate enters the multimode regime which can be seen on the spectra, the condensate width also appears to go up. The emitted spectrum measurements of the ground state become saturated at powers higher than 700 mW at that particular shutter speed.

The diagnostic camera focussed on momentum space can show images of the thermal cloud and BEC. As expected the condensate appears as a bright region at zero momentum. The camera also allows us to measure momentum-space images as shown in figure 5.10. The below-threshold image shows a gaussian intensity profile, as expected given that the corresponding position-space image of the thermal cloud is also a gaussian. The data again shows multimode condensation at far above threshold which results in a wide distribution of momenta. The above-threshold image shows a narrow band of momentum showing that the condensate is concentrated in momentum as well as position. We also show a cut-through of the momentum images showing how a peak appears above threshold which allows the widths of the thermal cloud and condensate peak to be seen. The greyed areas in the plot show sections of distortion where the calibration between pixel and momentum is not trustworthy. The width of the population distributions match estimated values: the condensate momentum width can be found from the width of the harmonic oscillator $p_{ho} = 1.1 \times 10^{-29}$ and the thermal cloud momentum width $p_{th} = 1.8 \times 10^{-28}$ from the thermal energy scale:

$$p_{ho} = \sqrt{\hbar \Omega m_{ph}} \tag{5.20}$$

$$p_{th} = \sqrt{m_{ph} k_B T} \tag{5.21}$$

5.3.3 Photon-Molecule Coupling Strength and Effective Mass

Polaritons are formed if photons strongly couple to dye molecules in the cavity. The effective masses can be found by formulas from a paper by Deng et al[77] which applies here. There are two kinds of polaritons (known as the upper and lower polaritons) which have effective masses $m_{\mp}$ given by:

$$\frac{1}{m_{\mp}} = \frac{|X_{\pm}|^2}{m_{molecule}} + \frac{|X_{\mp}|^2}{m_{ph}} \tag{5.22}$$

where $m_{molecule}$ is the molecule mass, m_{ph} as before is the effective photon mass and $X_{\pm}$ are the Hopfield coefficents given by:

$$|X_{\pm}|^2 = \frac{1}{2}\left(1 \pm \left[\frac{\Delta}{\sqrt{\Delta^2 + 4g_0^2}}\right]\right) \tag{5.23}$$

where g_0 is the light-molecule coupling strength and Δ is the cavity detuning from the molecular resonance, also known as the zero-phonon line, which in the Rhodamine-6G dye used in our experiment is 545 nm.

Fitting a parabola to the dispersion relation of the thermal cloud is a way to measure the effective photon mass using equation (5.7). This allows probing whether there is coupling between photons and molecules closer to resonance, which would show as a sharp increase in mass close to the zero-phonon line wavelength. This data was taken by manually tilting the grating to reach to wider range of energies than can fit on one camera image. Figure 5.11 plots the measured effective mass against the theoretical mass if there were photon-molecule coupling. It shows data consistent with no photon-molecule coupling. The data is quite noisy presumably because of the variation of wavelength calibration. There is essentially no or very weak coupling.

Figure 5.12 shows a plot of inverse curvature against longitudinal mode number showing a match with the above equation (5.24). Image processing is again used to find the co-ordinates of the parabola, inverse curvature data fits well to formula (5.24). We also show an example parabola in a position-resolved spectrum with fit overlaid on image.

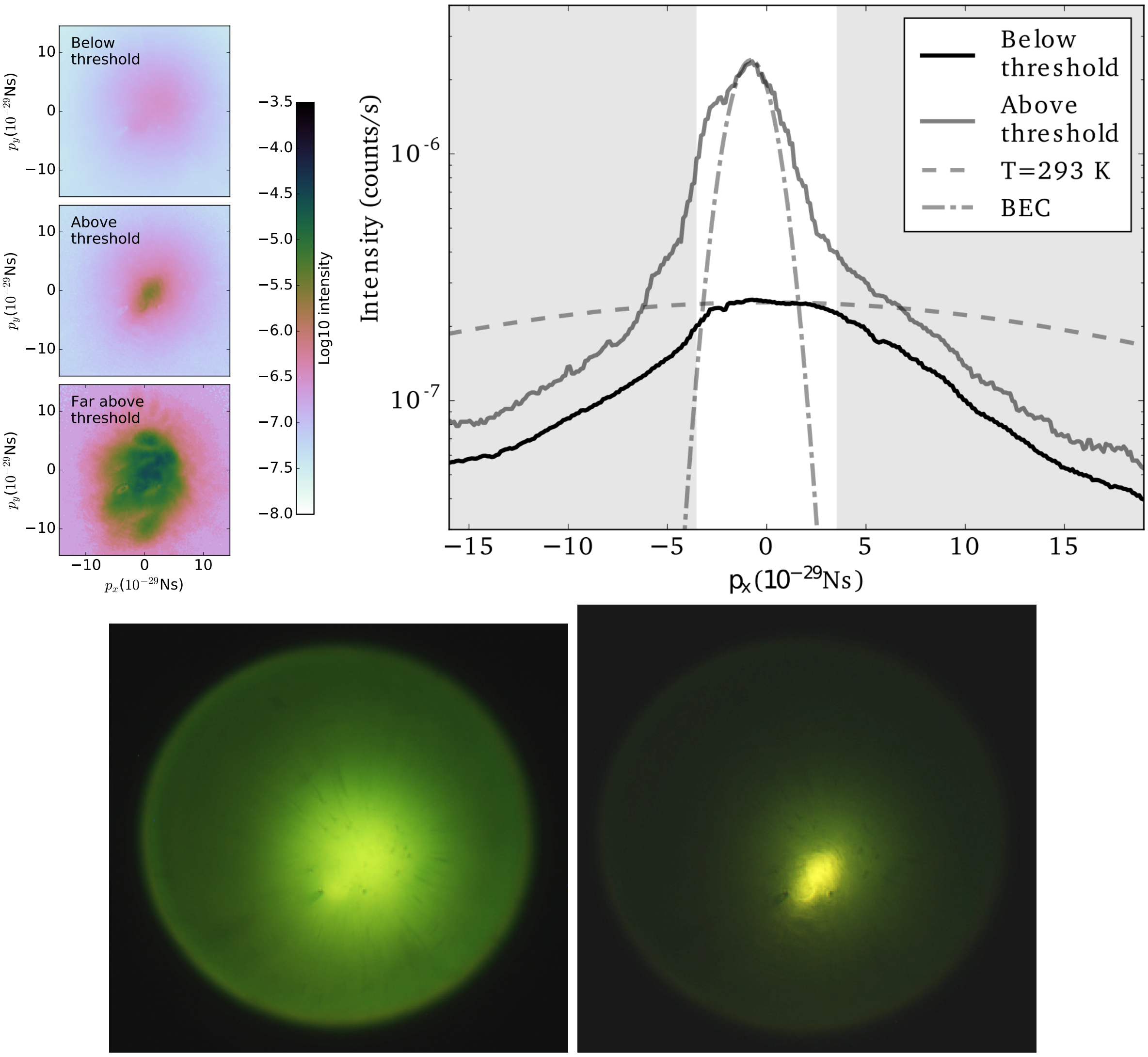

Figure 5.10: Top Left: Images below, above and far-above threshold showing how the BEC is concentrated in momentum. Far above threshold in the multimode regime we see a broadening of momenta. Note that due to pincushion distortion the calibration is only accurate below 4×10^{-29} Ns. Top Right: Cut-through of momentum images. The dashed line is a theoretical thermal cloud at room temprature. The dot-dashed line is a theoretical BEC momentum profile. The greyed region is where pincushion distortion reduces the accuracy. Bottom: Momentum-space images below (left) and above (right) threshold, showing a bright region at zero momentum corresponding to the condensate.

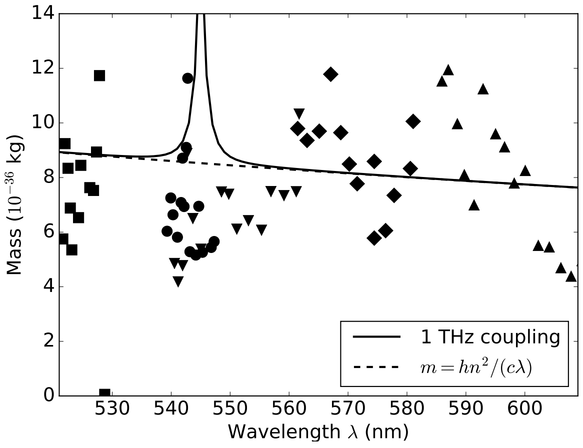

Figure 5.11: Measured effective photon masses at varying cutoff wavelengths, found by fitting a parabola to dispersion relation seen on the momentum-resolved spectrum. Dark line is theoretical showing the case where photon-molecule coupling would be observed. Dashed line is the bare cavity photon mass with no coupling. Each different shape of the points refers to a different manual positioning of the diffraction grating, which is required to get a larger range of wavelengths than can fit on one camera image.

5.4 Position-Resolved Spectrum

5.4.1 Calibrating Position Scale

The position-resolved spectrum will also show a parabola shape matching the quadratic potential landscape (see equation (5.8)). The curvature of this parabola, described by the quadratic coefficent $a(q)$ as in $V = ar^2$, will also depend on the longitudinal mode number q following relation:

$$\frac{1}{a(q)} = R\left(\frac{\lambda_0}{hc}\right)[\lambda^* q - 2L_{off}] \tag{5.24}$$

where R is the radius of curvature of the spherical cavity mirror (= 0.25 m in our experiment), λ_0 and λ^* are the cutoff wavelengths in free space and in the dye medium with refractive index $n_L = 1.44$. L_{off} is the distance the light penetrates into the mirrors.

5.4.2 Potential Energy Landscape

Figure 5.13 shows position-resolved spectra $n(\vec{r}, E)$ for three regimes (far-below, above, and far-above threshold) of pump power, as well as real-space images of the same data. Most light emitted is from close to the bottom of the parabola and at the edges, which is contrary to the model in equation (5.8) which predicts a uniform filling of the parabola. This is likely due to vignetting where the high angles/momenta are blocked off by the imaging optics. Only cavity emission light with a low kinetic energy, corresponding to low emission angles, is accepted by the optical setup. The slit in the telescope placed at the real-space image therefore acts as a momentum-space filter cutting off the higher angles, and therefore the position resolution is no better than about 15 μm.

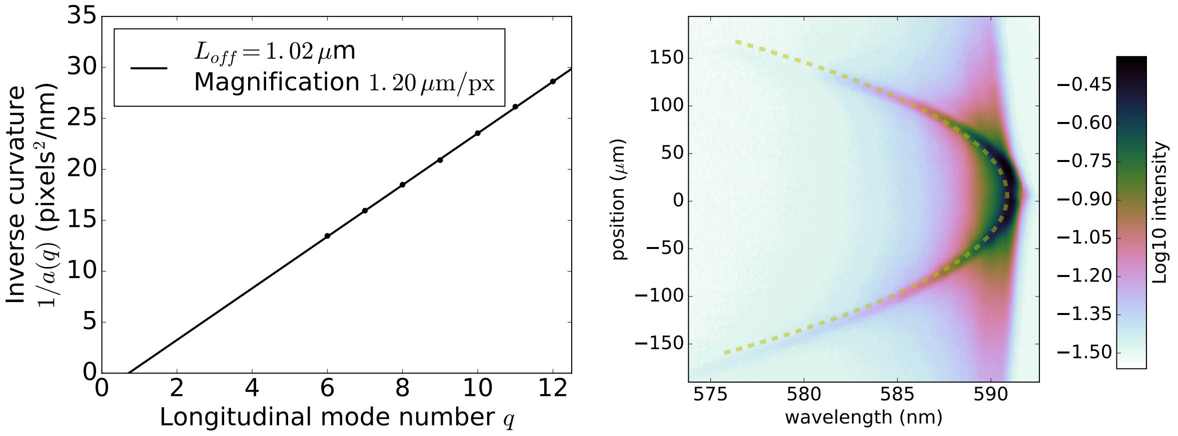

Figure 5.12: Left: Measured inverse parabola curvature a of the position-resolved spectrum. Depends on the longitudinal mode number q as in equation (5.24). The linear fit allows us to calibrate the spatial dimension. Right: An example parabola with arbitrary intensity units in the position-resolved spectrum, with fit matching the potential.

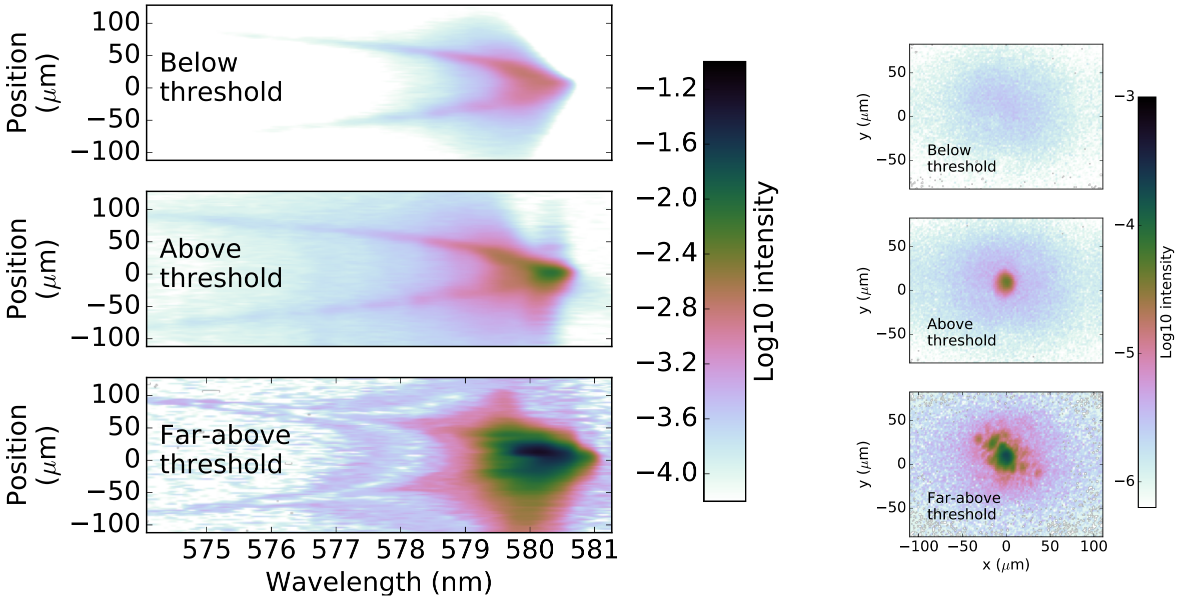

Figure 5.13: Position-resolved spectra (left) and real-space images (right) for below, above and far-above threshold. The parabolic curve can be seen which corresponds to the potential set by the cavity mirrors. Multimode behaviour explains the increase in width of the real space at far-above threshold

5.5 Conclusion

We have constructed a 2-dimensional spectrometer that can be configured to be momentum-resolved or position-resolved. We use it to measure any Bogoliubov effects arising from photon-photon interactions and find a value of the dimensionless interaction parameter consistent with other experiments. The strength of any photon-molecule interactions is also very weak, finding that the light is acting as free photons even close to the zero-phonon-line. We also find that effective temperature is not momentum-dependent implying that the system is always ergodic even when it is not at thermal equilibrium.

The experimental setup seems to work well although the spherical aberrations affect measurements at higher momenta. This could potentially be resolved by larger-aperture optics. Energy resolution could be improved by using a grating with finer spaced lines than our 1800 lines/mm.

Chapter 6

Laser Power Stability

6.1 Motivation

6.1.1 Damm Heat Capacity and Lambda Point

The Bonn group published a paper Damm et al[45] about accessing thermodynamic properties of the Bose-Einstein condensate, in particular the heat capacity. The reasoning used in the paper is that internal energy U and total photon number N can be calculated using spectrometer readings $n(\lambda)$:

$$U = \int_{-\infty}^{\lambda_c} n(\lambda) hc \left(\lambda^{-1} - \lambda_c^{-1}\right) d\lambda \tag{6.1}$$

$$N = \int_{-\infty}^{\lambda_c} n(\lambda) d\lambda \tag{6.2}$$

where as before λ_c is the cutoff wavelength corresponding to the ground state energy, and all other symbols have their usual meaning. A reduced temperature $\theta = T/T_c$ can be calculated from $N/N_c = (T_c/T)^2$ which follows from relation 1.13. Internal energy per particle and (reduced) temperature together can be used to calculate the heat capacity $C = \partial U/\partial T = k_B \partial(U/k_B T_c)/\partial(T/T_c)$. Data from the paper is shown in figure 6.1 and they shows a lambda-point-like structure similar to that appearing in other BEC systems.

First published in 1930[78], the lambda point is a cusp singularity in the specific heat capacity. The phenomenon was apparently first observed by Onnes and Dana in Leiden in 1924 soon after the liquefaction of helium. Just below the temperature of the density maximum at 2.2K they had found values of the specific heat which were so high that they dared not publish them, feeling sure that something had gone wrong with their equipment[79]. Six years later Keesom and Clusius published their measurement of the lambda point[80], so called because it resembles the greek letter λ, and below which the liquid helium became a superfluid[81]. Lambda points can also been seen in atomic BEC[82][83]. That the same phenomenon appears to also be present in photon BEC is an interesting development.

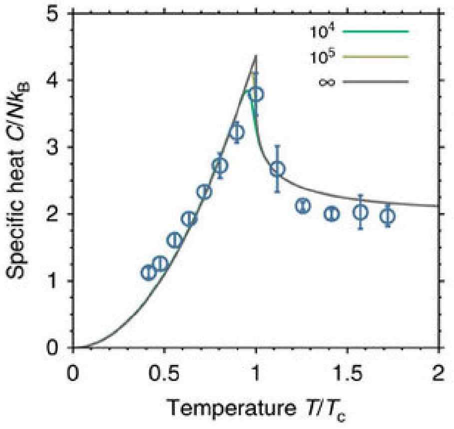

Figure 6.1: Figure from Damm et al[45] showing specific heat per photon versus the reduced temperature T/T_c, showing a cusp discontinuity at the critical temperature.

Examining the maths of Damm et al. more closely, we find that the heat capacity is not the usual thermodynamic heat capacity, defined as $C = \partial U/\partial T$ and as the experiment happens at a constant temperature that quantity must be zero. So we name the *Damm heat capacity* as $C_D = \partial U/\partial \theta$, where $\theta = T/T_C$ which is similar to the heat capacity and also shows the lambda-point feature at BEC threshold.

6.1.2 Measurement of Heat Capacity Without Laser Power Stabilization

We have spectrometer data as a function of many different pump powers, and could use it to calculate the internal energy of the BEC and see if the λ-point feature appears. Unfortunately the data is too noisy to numerically differentiate and extract a meaningful heat capacity. Instead we use relevant theory from Klünder and Pelster[84] to plot the data alongside a function for the specific internal energy. The intention is to then differentiate the specific internal energy to obtain heat capacity.

Theory

From the grand canonical potential many other thermodynamic properties can be derived, like particle count and entropy $S = -\frac{d\Omega}{dT}$ can be found, from which the internal energy $U = \Omega + TS + \mu N$ can be derived. The Klünder paper starts with the grand canonical ensemble description of an ideal Bose gas trapped in a isotropic harmonic potential. We start with the Equation (5) from the paper, the final form of the grand canonical potential Ω:

$$\Omega = -k_B T \sum_{m=0}^{\infty} \binom{m+D-1}{m} \zeta_1 \left(e^{(\mu - E_0 - m\hbar\omega)/k_B T} \right) \tag{6.3}$$

Where $\zeta_a(x)$ is the a-th order polylog function, D is the number of dimensions of the system, T is the temperature, ω is the trap frequency of the simple harmonic oscillator model for the system, E_0 is the ground state energy, $\binom{N}{k}$ is the binomial coefficient function and the other symbols have their usual meanings. From this the particle count $N = -\frac{\partial\Omega}{\partial\mu}$ and entropy $S = -\frac{d\Omega}{dT}$ can be found:

$$N = \sum_{m=0}^{\infty} \binom{m+D-1}{m} \zeta_0 \left(e^{(\mu - E_0 - m\hbar\omega)/k_B T} \right) \tag{6.4}$$

$$\begin{aligned} S = k_B & \sum_{m=0}^{\infty} \binom{m+D-1}{m} \zeta_1 \left(e^{(\mu - E_0 - m\hbar\omega)/k_B T} \right) \\ & - \frac{1}{T} \sum_{m=0}^{\infty} \binom{m+D-1}{m} (\mu - E_0 - m\hbar\omega) \zeta_0 (e^{(\mu - E_0 - m\hbar\omega)/k_B T}) \end{aligned} \tag{6.5}$$

Then the internal energy can be calculated with $U = \Omega + TS + \mu N$

$$U = \sum_{m=0}^{\infty} (m+1)\,(E_0 + m\hbar\omega) \zeta_0 (e^{(\mu - E_0 - m\hbar\omega)/k_B T}) \tag{6.6}$$

$U\,(T)$ can be plotted in terms of N/N_C using the relation

$$\frac{T_C}{T} = \left(\frac{N}{N_C} \right)^2 \tag{6.7}$$

to convert from temperature to number.

For plotting and numerical purposes, we generate a list of μ values which are used to calculate specific energy. We plot the population relative to N_C the threshold population, recalling equation (1.13) to obtain the critical number

$$N_C = \left(\frac{\pi^2}{6} \right) \left(\frac{k_B T}{\hbar\Omega_0} \right)^2 \tag{6.8}$$

Data

A background-subtracted spectrum is integrated between the appropriate limits as in equation (6.1). Figure 6.2 shows this data and the model for energy per particle in units of $k_B T$ plotted on the same axis. Both data and theory show the same shape with the same slope of the line on a loglog graph. The BEC transition at $T = T_C$ as the slope of the line changes at threshold can also be seen on both. The data is very sparse around and immediately below threshold temperature, which when converted to power means there is data far above and far below threshold but almost none near to it. The data levels off far below the threshold temperature, corresponding to higher powers, so this feature is presumably due to the noise floor. The lack of data around the interesting threshold area is due to the instability of the laser power, and is a major part of the motivation for the work in this chapter.

6.1.3 Stabilizing Laser Power

The sharp feature of the Damm heat capacity requires very well stabilized pump laser power with a value known to a high precision. The laser light must arrive at the cavity in short pulses. The parameters used are 500 ns pulses, which are repeated at a rate ranging from 500 Hz to 2000 Hz. These parameters result in a very low duty cycle (500 ns × 2000 Hz = 0.1%). The pulses are created by the acousto-optic modulator (AOM) rapidly switching between high- and low-transmission modes. The AOM still has some transmission in the low-transmission mode, and combined with the small duty cycle, will introduce a large error if measuring the laser power at DC frequencies (e.g. with a power meter or multimeter). Instead we will use sample-and-hold electronics to measure the height of the laser pulses. This electronics can give us a DC signal proportional the laser power which can be fed to a proportional-integral-derivative (PID) controller. This PID controller can reduce the fluctuations of the laser power and, by following the set-point, allow the laser power to be quickly changed.

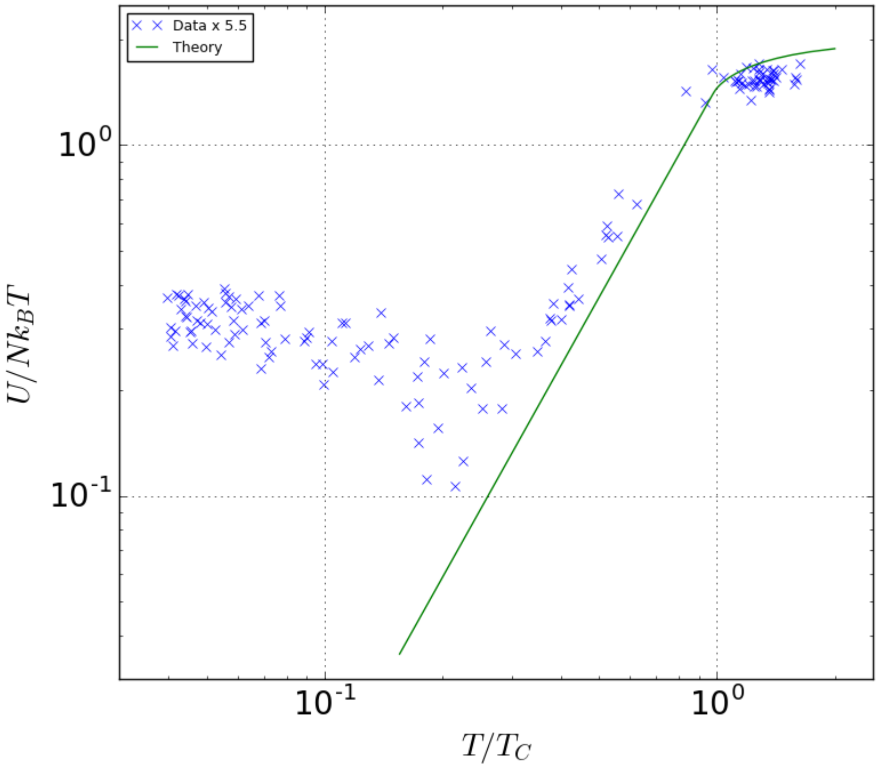

Figure 6.2: Specific energy vs reduced temperature. Plotted model is equation (6.6). There is a factor of 5.5 difference between the theory and data which shows the data shifted downwards on the loglog scale. The upward slope below threshold indicates a constant heat capacity. The lack of data at and immediately below threshold is an indicator of the unstable laser power. The rolloff below a temperature around 0.2 is due to the multimode behaviour which is not handled by the model. The downward slope in the multimode regime seems to indicate a negative heat capacity.

6.2 Circuitry

6.2.1 Acousto-Optic Modulator

The Acousto-Optic Modulator (AOM) part of the laser setup requires some description. The AOM works by having a piezoelectric transducer in contact with a material such as glass or a crystal. The piezoelectric is driven by a voltage-controlled-oscillator (VCO) at a frequency of about 110 MHz to produce sound waves of alternating compressed and expanded regions. These change the index of refraction of the material and diffract the laser light into several beams, all but one of which are stopped by beam blockers. The intensity of this one beam, and therefore the transmission of the entire setup, can be controlled by the amplitude of the radio waves coming from the VCO, henceforth known as the AOM-amplitude. By using an RF switch to block and unblock the radio waves, the AOM setup can be switched from high- to low-transmission modes. The amplitude can be controlled from a BNC input and also has a potentiometer which can be turned with a screwdriver. The extinction ratio of the entire setup is about 10^4, for our typically-used pulse length of 500 ns with a repetition rate of 500Hz, this results in the light passing through during the AOM off-state giving a voltage reading two orders of magnitude more than light passing through during the on-state. In practice if this light was measured with a power meter that averaged over a long period of time, it would overwhelmingly be measuring this leakage rather than the power of the pulse itself.

Figure 6.3 shows the 500 ns trigger pulse from the function generator plotted on the same graph as the resulting light pulse. There is a delay of about 600 ns between them which is the reason a delay circuit is required in the sample-and-hold circuitry.

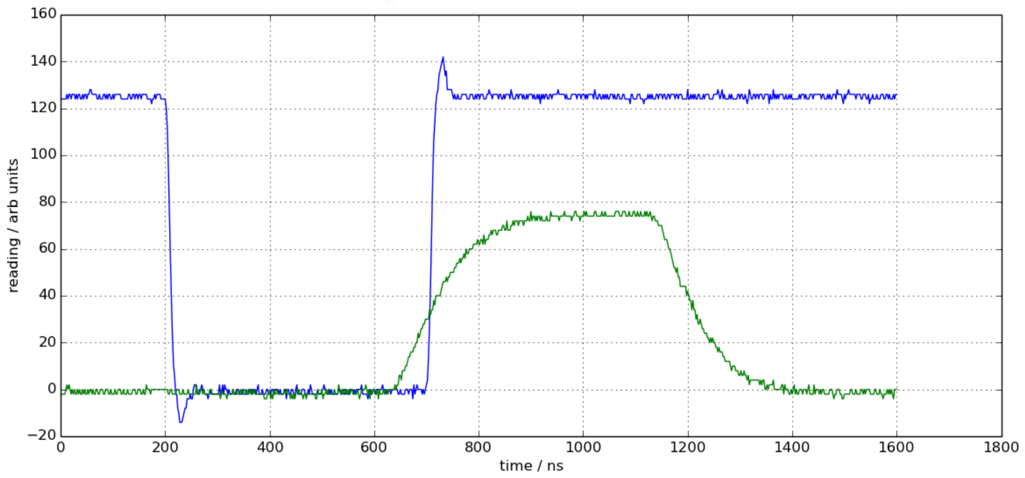

Figure 6.3: Blue: Trigger pulse from function generator. The left falling edge is the “on” trigger. Green: Laser light output on photodiode. The laser light output is delayed by approximately 600 ns relative to the trigger pulse.

6.2.2 Photodiode

After the AOM we pick off a small percentage (about 1%) of the laser beam with a glass wedge. The reason we use a wedge instead of a glass slide with parallel faces is that parallel faces cause etalon-ing which causes drastic changes in reflection from moment to moment. The reflection is attenuated with a neutral-density filter and focussed onto a photodiode. We choose 510 Ω as a resistor value in parallel as a tradeoff between voltage level and response time required to measure the 500 ns laser pulse. The time constant of the system is about 70 ns. The output of the photodiode gives a voltage proportional to the laser power, it saturates at a light level higher than the laser can produce.

6.2.3 Pre-Amplifier

The photodiode is a current source and has an effective capacitance which constrains the output impedance. We cannot increase the output voltage without slowing down the response. The need for high bandwidth and low noise required us to build an amplifier, as a part with the required specification was not available on the market.

The full circuit diagram is on figure 6.4. We use capacitors set very close to the power pins in parallel with ground to damp fluctuations of the op-amp when it was loaded. We use low-noise high-frequency operational-amplifiers (Op-Amps), of part number AD8055 which are capable of amplifying frequencies up to 40 MHz without oscillating. We used capacitors on the feedback branch to damp certain frequencies. Finally the circuit was put inside a box to further isolate from noise sources.

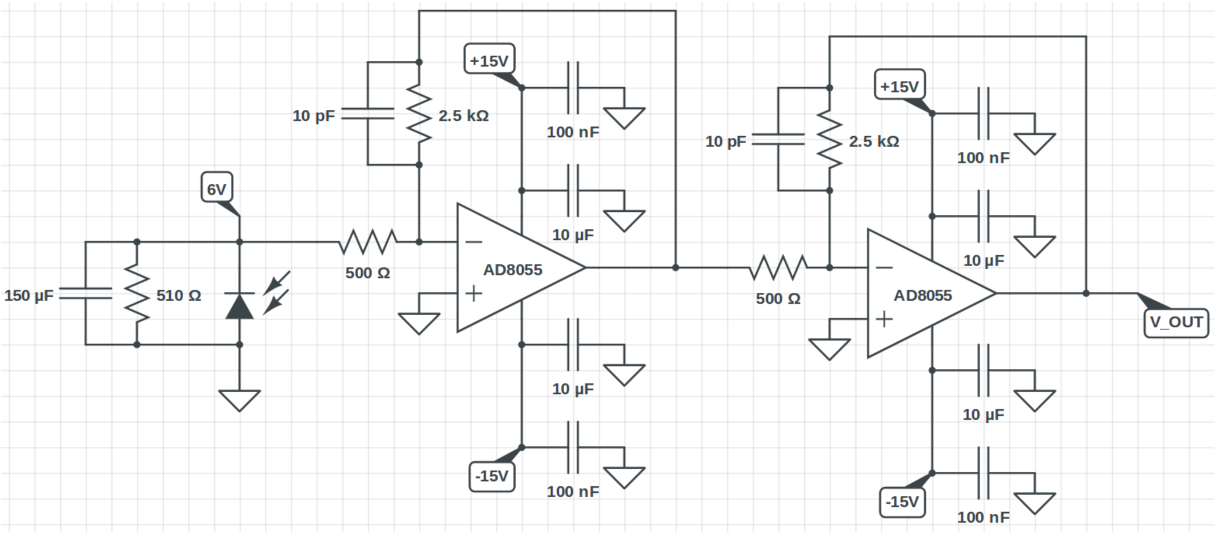

Figure 6.4: Pre-amplifier circuit diagram. Two stages of op-amp amplifiers result in a gain of 20. Ground bypass capacitors placed close to the op-amp integrated circuit are vital for reducing noise.

6.2.4 Sample-and-Hold-Amplifier

The pre-amplified photodiode gives a voltage signal proportional to the laser power. We use a sample-and-hold amplifier (SHA) to measure the height of the pulse. We use part number AD783 which has an acquisition time of 250 ns which is suitable for our needs. Note that the SHA circuit has a gain of 1, so if operating the laser in continuous-wave then the SHA can be removed without affecting anything else in the setup.

6.2.5 Delay

We use a function generator to create the pulses that drive the AOM's beam chopping. We could use this same signal to trigger the SHA and make it sample exactly at the full height of the laser pulse. However there is a problem of delays in the system. The delay between the frequency generator and the actual laser pulse is about 600 ns, and is caused by sound wave propagation time inside the AOM crystal. This means we need a way to delay the pulses from the function generator before reaching the SHA.

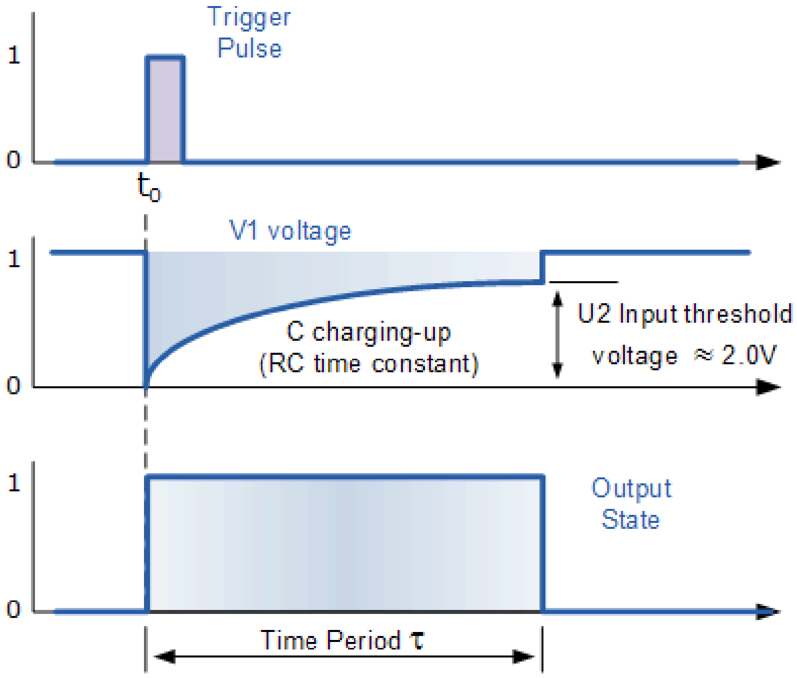

Figure 6.5: Pulse produced by monostable multivibrator, the length of which is determined by a RC circuit. Image from *http://www.electronics-tutorials.ws/waveforms/monostable.html*

We build a pulse delayer using two monostable multivibrators, a flip-flop and a NOT-gate. A monostable multivibrator is an electrical component that when triggered generates a pulse. The width of this pulse can be controlled with an RC component connected externally, see figure 6.5. A flip-flop (also known as a latch) is an electrical component that has two stable states, 1 or 0. Sending binary messages to the component can make it switch from one state to another, it acts as a single bit of memory.

To create a pulse with a controllable delay and width, we use two monostable multivibrators and a flip-flop. A rising edge of the pulse from the function generator produces one pulse on a monostable, the falling else produces another pulse. The two pulses are fed into the flip-flop which makes it go from a 0-state to a 1-state and back again to 0-state depending on the width of the two monostable multivibrator pulses. Since these widths are controllable by RC circuits we can choose the parameters of the resulting pulse. See figure 6.6 for a diagram of pulses showing how each RC value controls the properties of the delayed pulse. We chose R_1C_1 and R_2C_2 so that the pulse has the correct delay and that it is short enough to sample a flat region of the pulse.

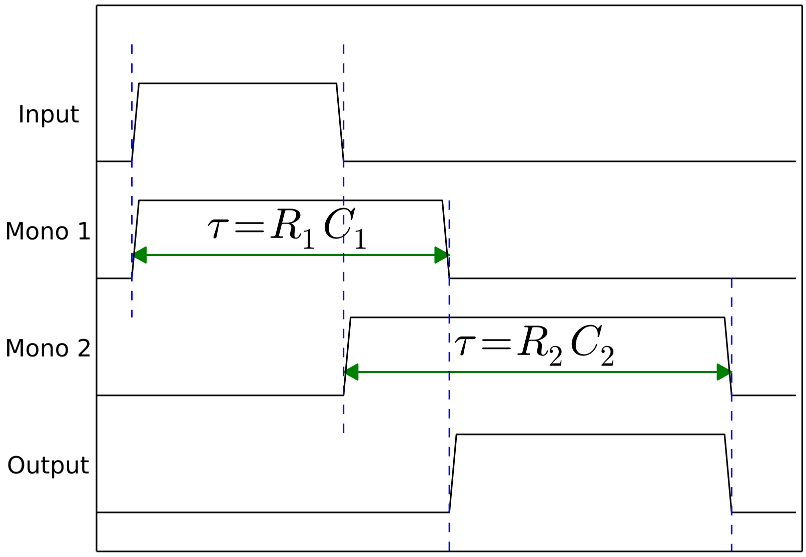

Figure 6.6: Sequence of pulses that produce a pulse output with a tunable delay and width.

The monostable part number we use is MM74HC221A which has two monostables on its integrated circuit. With some calculation and trial-and-error we chose the RC values to cause the SHA to correctly sample the pulse. This scheme of monostable and flip-flop produces an inverted pulse. The NOT-gate is used to correct this.

6.2.6 PID Controller

A PID controller will use the measurement of the laser power from the sample-and-hold circuit with a feedback to the AOM amplitude to reduce the fluctuations in the laser power and allow it to be rapidly changed.

The basic equation of a PID controller is shown in equation (6.9).

$$u(t) = K_p e(t) + K_i \int_0^t e(\tau) d\tau + K_d \frac{de(t)}{dt} \tag{6.9}$$

Where t is time, $u(t)$ is the output also known as control variable, $e(t)$ is error signal defined as the difference between input signal and set point. The output is fed back to device being controlled which will influence the input signal, in this way a PID controller will stabilise a variable such as the laser power around the set point. The weights K_p, K_i, K_d must be carefully chosen so that the PID controller works correctly, reaches the set-point quickly and does not oscillate. PID controllers do not eliminate noise, instead they move it out to different Fourier frequencies. For our purposes we need to create a noise-reduced region from DC up to about a few hundred Hertz.

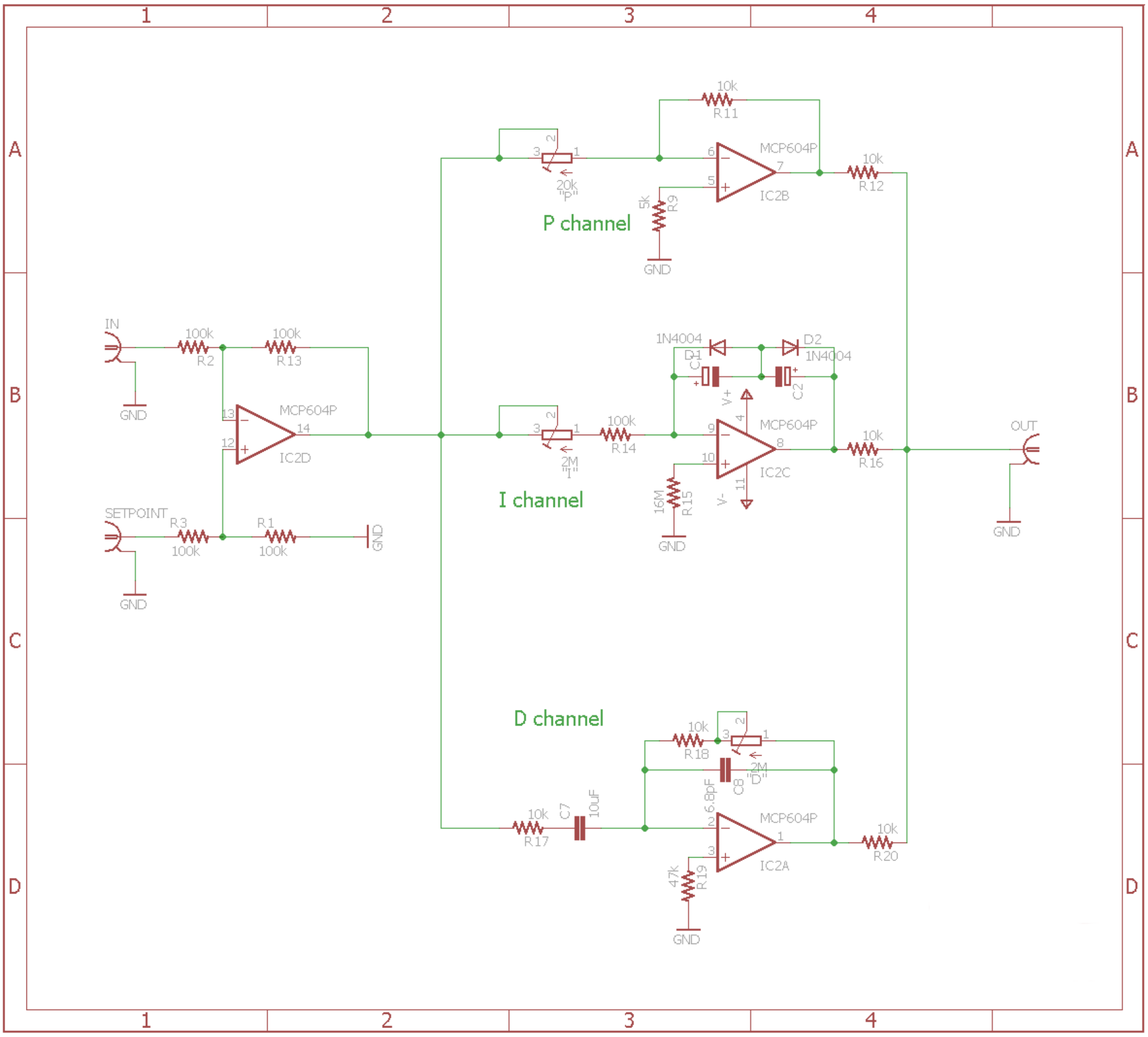

Figure 6.7: PID circuit diagram. The difference between the input signal and set-point ports on the left is found with the first from the left op-amp circuit. The P-, I- and D-channels are calculated with the corresponding actively-driven proportional amplifiers, integrators and differentiators. The results are combined with a passive adding circuit and sent to the output port on the right which is sent to the AOM amplitude for controlling the laser power.

A PID controller in electronics is made from a few basic circuits. Figure 6.7 shows our circuit diagram, the output port is on the right side and the two input ports of the signal and the set-point are on the left side. Op-amps are used to create actively-driven difference-calculators for calculating the error signal, as well as proportional amplifiers, integrators and differentiators. It is possible to create an active adder to combine the results before the output, but for our circuit we used a passive adder with different valued resistors. In practice we leave the differentiator channel unconnected as we found the stabilization works adequately without it, the oscillation due to only having a proportional and integral part is very small in practice.

The correct values of resistors, which control the PID weights, was intended to be chosen by using this procedure:

1. Have the set-point be a square wave driven by a function generator, zoom in with an oscilloscope to see transient behaviour.
2. Only connect proportional part of the circuit.
3. Increase the proportional gain until oscillatory behaviour is just about to begin.
    (a) You should notice that the error signal never reaches zero (i.e. the output never reaches the set-point because as the error signal approaches zero so does the response).
4. Connect integral part of the circuit.
5. Increase integral gain until the output reaches the set-point without oscillating.

Limiting Frequency of Proportional Gain

The laser pulse repetition rate is 500Hz which means the sample-and-hold-amplifier output only updates at that frequency. For this reason we place a suitable capacitor in parallel with the feedback resistor on the proportional gain op-amp. This limits the speed of the proportional gain part of the PID controller.

6.2.7 Putting it all together

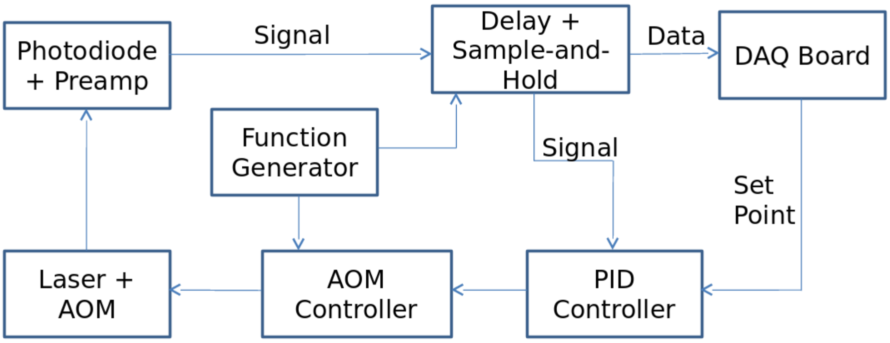

Figure 6.8: Diagram of all components

All the components are connected up as in figure 6.8. The output of the PID controller is fed to the AOM amplitude input, closing the loop. The potentiometer which also controls the AOM amplitude is turned up to just-below-maximum voltage, the PID controller output is added to this and its movements can damp the noise fluctuations as well as turn down the power to follow the set-point. There is also a configuration without the SHA for when the laser setup is operated in continuous-wave mode with pulsing switched off.

6.3 Testing Feedback Control

6.3.1 Set-Point Step-Function Response

We wanted to find the response time of the system when the set-point is driven. We drive the set-point using a frequency generator which produces a clean square wave with a bandwidth much higher than our system and no overshoot, and fit the laser power response to a formula for a finite-response square wave $y(t)$.

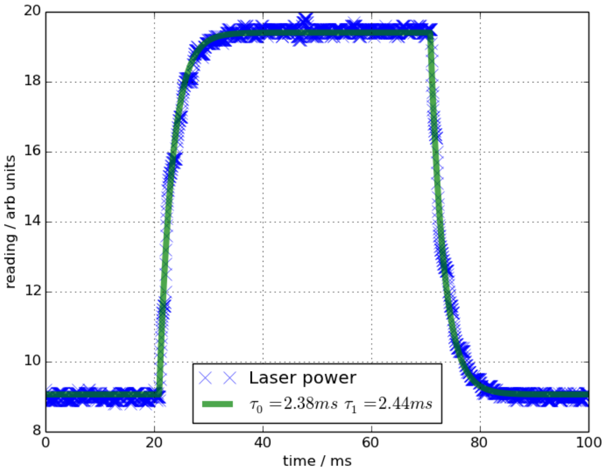

Figure 6.9: Laser power in response to PID set-point being driven by a square wave. Fitted to equation (6.10). The bunching of the blue data crosses on the plot correspond to the individual laser pulses. This shows that the laser power is stabilized within only a few pulses. The response times for the rising and lowering edge correspond to bandwidths of about 410 Hz which is as expected from the PID controller circuit.

$$y(t) = \begin{cases} L & t < t_0 \\ H - (H - L)e^{(t-t_0)/\tau_0} & t_0 < t < t_1 \\ L + (H - L)e^{(t-t_1)/\tau_1} & t_1 < t \end{cases} \tag{6.10}$$

where t is time; t_0, t_1 are the times when the function steps between high and low; τ_0, τ_1 are the response times and H, L are the high and low levels of the square wave. The results are shown in figure 6.9 of the response to the square wave fitted to formula $y(t)$. The individual laser pulses can be seen on the plot, by the bunching of the blue data crosses. This shows that the laser power is stabilized within only a few pulses which is an inherent limit to this particular setup. The response times for the rising and lowering edges are found to be 2.38 ms and 2.44 ms respectively, which correspond to bandwidths of about 410 Hz. This is expected from the bandwidth parameters in the PID circuit, which cannot stabilize faster than the pulse repetition rate due to the fact that the same AOM chops the beam into pulses and also controls their amplitude.

6.3.2 Measured Noise Power

Figure 6.10 shows the calibration of the set-point voltage to laser power. We placed a power meter after the AOM and measured the laser power in CW mode. The figure shows a linear fit between set-point voltage and laser power up to a cutoff above which the calibration is no longer linear because of the AOM behaviour at higher amplitude voltages.

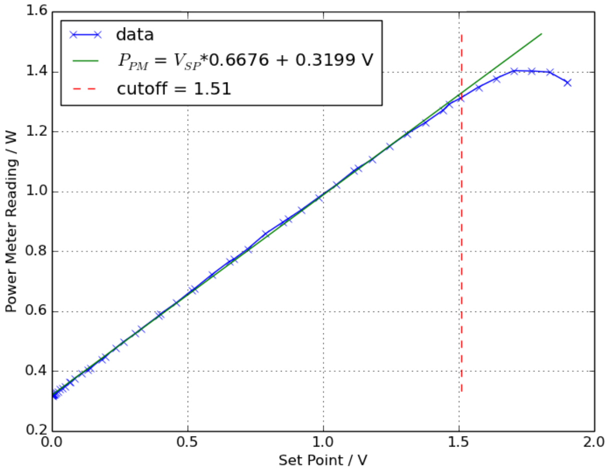

Figure 6.10: Set-point voltage calibration to laser power. Shows a good linear fit up to the cutoff above which the AOM behaviour at higher amplitude voltages changes to show the distortion.

We measured the laser power fluctuations by connecting the photodiode and pre-amplifier straight to the Data Acquisition board (DAQ). We use the NI-USB-6008 DAQ board which can measure at 10 kilosamples-per-second. We took 3 million datapoints per measurement which took 5 minutes. We also take the power spectrum of the fourier transform to see the noise in frequency space. The data is shown in figure 6.11, it shows the laser power fluctuating around 2000 mW with occasional jumps, drifting and with the amount of fluctuation changing with time. The power spectral density shows a spike at DC frequencies followed by a general steady drop with rising frequencies. There are several spikes at multiples of 50 Hz and around 1000 Hz there is a broader feature due to this data being taken at a pulse repetition rate of 1000 Hz.

The power spectral density is calculated using the standard Fast Fourier Transform method of calculating discrete Fourier transforms[85]. The discrete data signal $x(n)$ samples an underlying continuous laser power with N points of discrete time, its Fourier transform being $X(k)$ which represents the amplitude and phase of the associated frequency component. The two are related via the synthesis and analysis equations:

$$x(n) = \sum_{k=0}^{N-1} X(k) e^{i2\pi kn/N} \tag{6.11}$$

$$X(k) = \frac{1}{N} \sum_{n=0}^{N-1} x(n) e^{-i2\pi kn/N} \tag{6.12}$$

The two quantities are also related by Parseval's relation for a discrete series:

$$\sum_{n=0}^{N-1} |x(n)|^2 = \frac{1}{N} \sum_{n=0}^{N-1} |X(k)|^2 \tag{6.13}$$

From which we can deduce that the units of the power spectral density $X(k)$ are $W/\sqrt{Hz}$ if the units of the signal data are watts (W).

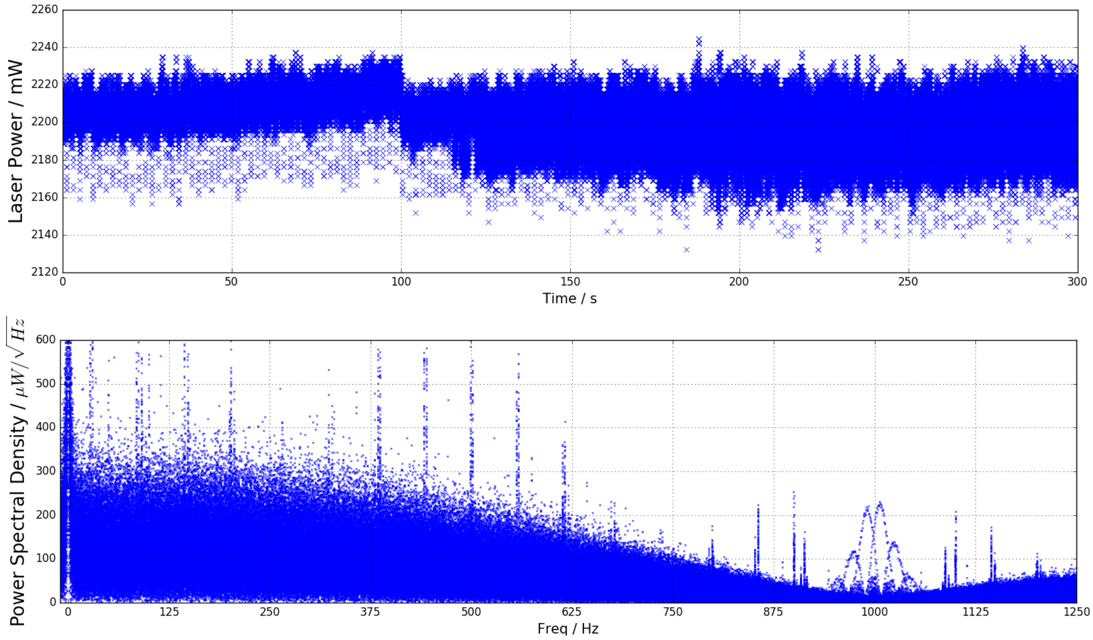

Figure 6.11: Laser power without stabilization. Top: Laser power vs time, shows drifting around 2200 mW as well as noise and jumps. Bottom: Measurement of laser power spectral density showing high noise at DC followed by a steady drop towards higher frequencies.

Connecting up the PID controller and reading again with the DAQ board results in eliminated drift and reduced noise. In certain data sets we see very-high-frequency noise appearing as short-lived bursts, which seems to be the PID controller circuit temporarily oscillating at a very high frequency. The noise averages to zero but it's visible to the 10 kHz device. We can also see the mains noise at multiples of 50 Hz is still there. The PID controller circuity was not in any kind of shielded box so likely picks up mains noise from the environment. The data is shown in figures 6.12 and 6.13. Figure 6.13 shows the laser power with stabilization with short-lived high-frequency bursts. Note that PID controllers in general do not eliminate noise but only shift it outside the frequency range. This is what is seen in the spectral data as the region 0 - 200 Hz has approximately 6 times lower noise than the non-stabilized data.

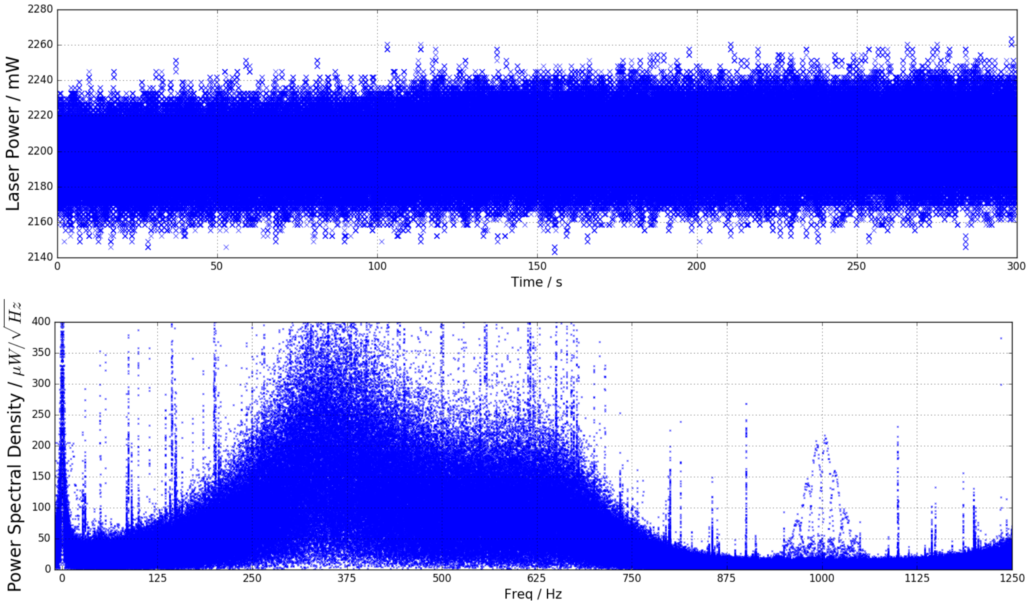

Figure 6.12: Laser power with stabilization. Top: Laser power vs time, shows a stable time trace. Bottom: Measurement of laser power spectrum showing noise shifted to higher frequencies.

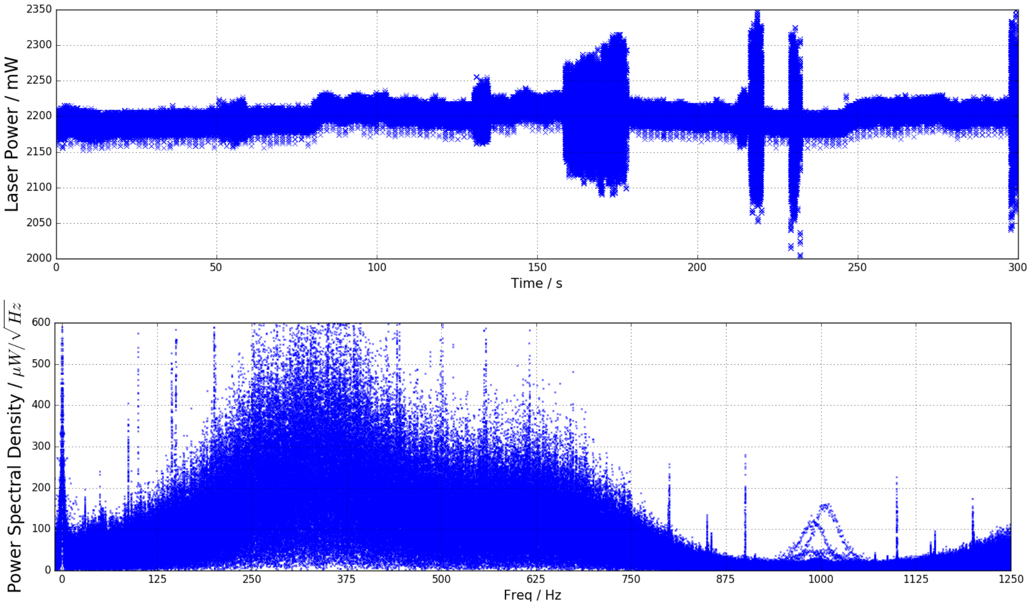

Figure 6.13: Laser power with stabilization with high-frequency bursts. Top: Laser power vs time, shows a stable time trace with some bursts of high frequency noise. Bottom: Measurement of laser power spectrum showing noise shifted to higher frequencies.

6.3.3 Example Usage: BEC Threshold Measurement

The PID controller is used to scan through stabilized laser powers. An image of the cavity light is taken with a camera using an autoexposure algorithm, and the central intensity (which is almost proportional to ground state population) is calculated from the images. The image is background subtracted and scaled to take into account shutter speed and gain. We add up the red and green pixels in a circular aperture centred at the cavity. The radius of the aperture is set equal to the width of the ground state mode of the cavity, which is 6 μm in object space converted to pixels in image space using a measurement of the magnification of the optical system and size of camera pixels. Central intensity is plotted against laser power set-point in figure 6.14, which is fitted to a bilinear function. The central intensity of the thermal cloud increases below threshold approximately linearly, after threshold the central intensity of the condensate also rises linearly but with a different slope. Fitting to both linear curves allows the threshold power to be deduced in noise-resistant way. This method also achieves a large dynamic range of measured power of nearly two orders of magnitude. The bilinear fit equation used is:

$$I(p) = \begin{cases} a(p - p_{th}) + I_{th} & p < p_{th} \\ b(p - p_{th}) + I_{th} & p > p_{th} \end{cases} \tag{6.14}$$

Where $I(p)$ is the central intensity as a function of power, a and b are the slopes below and above threshold, p_{th} is the threshold power and I_{th} is the intensity at threshold.

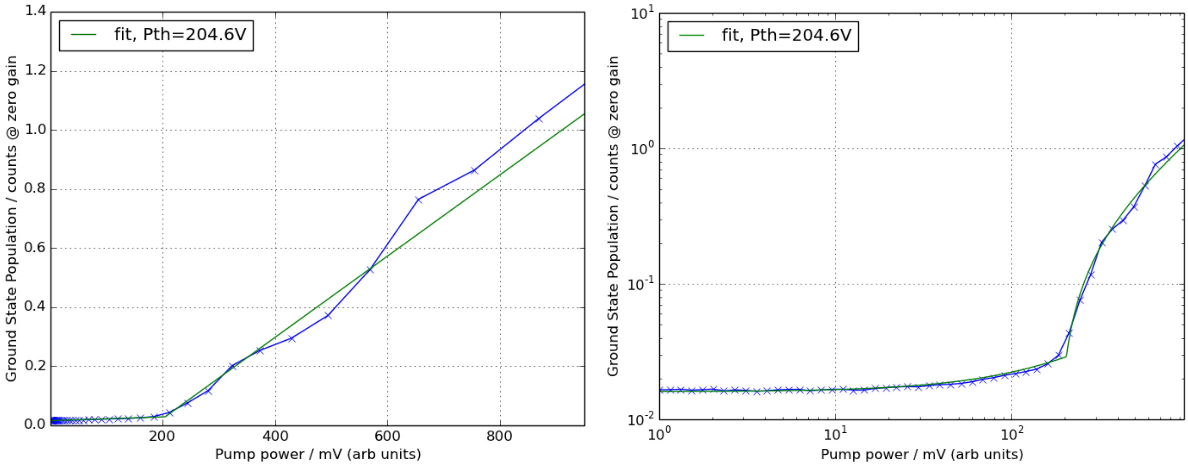

Figure 6.14: Central intensity vs laser power with bilinear fit on linear (left) scale and logarithmic (right) scale. The data is similar to Figure 4.12 but with much lower noise especially around the threshold.

We used this setup to re-take the data from section 4.3.3 but much faster in a more automated way with less noise. This data required approximately 2 minutes to take while the earlier data about one hour. Figure 6.15 shows data of the threshold power versus cutoff wavelength. We again find a minimum corresponding to the tradeoff between lower mirror reflectivity increasing the threshold at longer wavelengths and stronger molecule-photon coupling increasing threshold at shorter wavelengths.

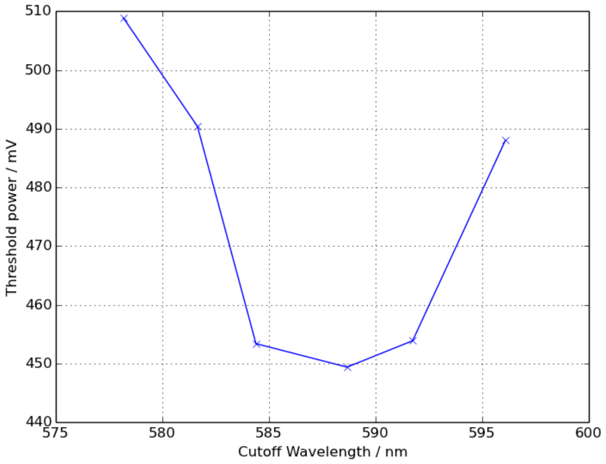

Figure 6.15: Condensation threshold vs Wavelength. Shows a minimum reflecting the tradeoff between molecule-photon coupling and mirror reflectivity. Same measurement as from figure 3.7 but taken in a faster and more automated way, which resulted in less noise. The result has the same shape as expected.

6.3.4 Comparing Threshold Finding With and Without Stabilization

The pump laser power can be changed without using the PID circuitry by changing the AOM amplitude. We took threshold vs wavelength data with and without the stabilization to find to what extent the PID controller stabilizes the pump power delivered to the cavity. We compare the stabilized and non-stabilized fits by plotting the fit residuals, which are defined as the log-difference between the bilinear fit and the actual data which can be interpreted as a measurement of noise and goodness of fit. Higher residuals values indicate a worse fit to the data. The less stable laser power should result in higher residual values, and this is what we see in figure 6.16 where the stabilized case has residuals an order of magnitude lower than the non-stabilized case. Critical phenomena always have large fluctuations close to threshold which appears as a large spike in the residuals for both datasets around threshold.

6.4 Conclusion

This laser power measurement method was done using a photodiode, sample-and-hold amplifier and PID controller. It is able to quickly change the laser power by having its set-point changed, and it damps the noise from DC up to about 250 Hz.

The system still suffers from mains noise which could be reduced by putting everything in shielding boxes. For example the PID controller right now involves long wires going to a solderless plug breadboard to make choosing gain weights faster by changing resistors.

The setup could be greatly improved by having two AOMs, one to control the transmission and the other to chop the laser into pulses. This would stop the requirement to limit the speed of PID to less than 500 Hz, and also remove the need for the pulse delaying and sample-and-hold circuits, however it would also result in 40% less laser power due to the loss in an extra AOM.

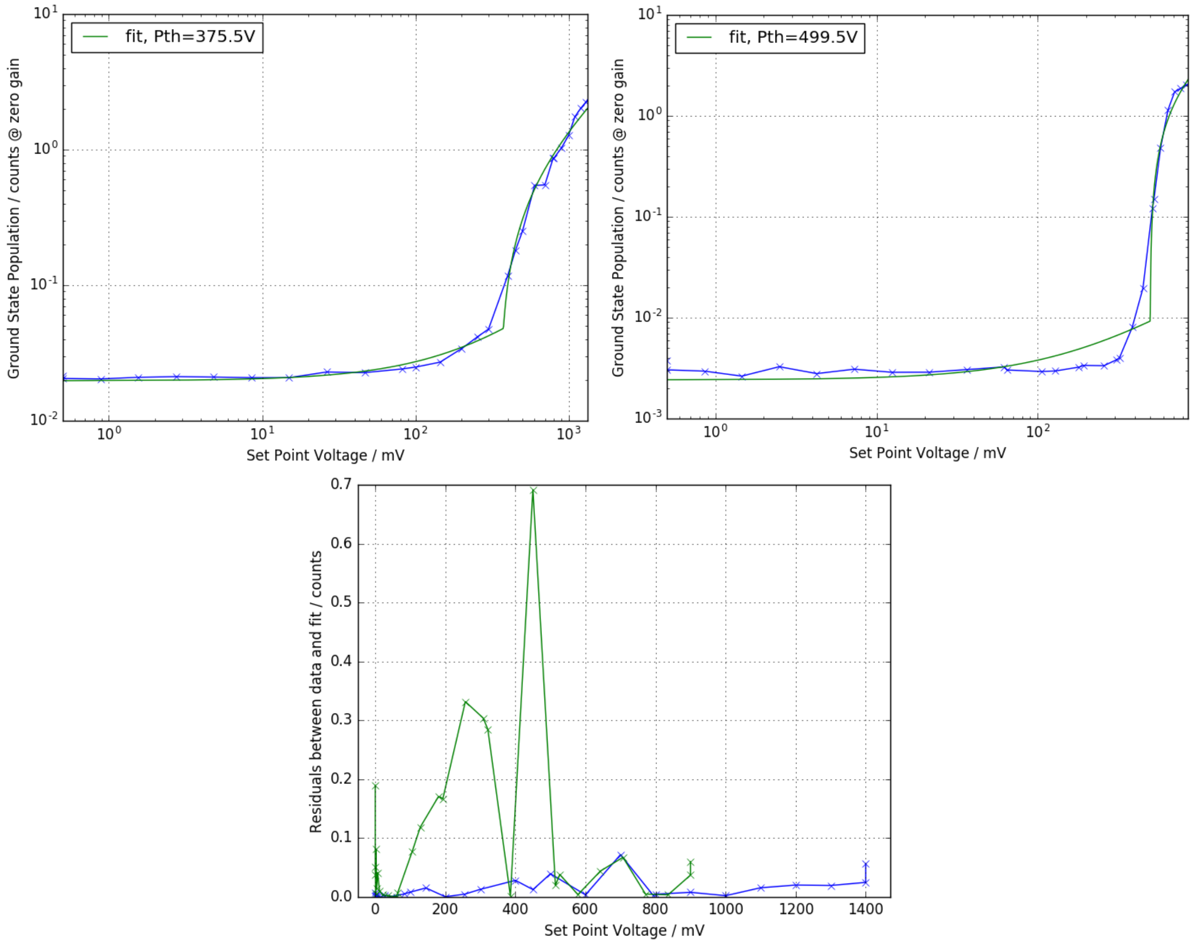

Figure 6.16: Ground state intensity vs cutoff wavelength, for stabilized (top left) and non-stabilized (top right) case. Residuals (bottom) are the log-difference between the data and fit, they are an indication of goodness of fit. The non-stabilized data has an order of magnitude higher residual values than the data with the stabilized pump laser. Also by eye the data with stabilized laser appears to have a better fit.

Chapter 7

Conclusion

The physics of Bose-Einstein condensation has a history going back to the early 20th century, advances in laser cooling of atoms allowed the first creation of BEC in 1995. Condensation is also possible in photons which was achieved in 2010 and again by our group in 2014.

We built an experimental setup for creating photon BEC. Rhodamine-6G dye is held by surface tension between two parallel high-reflectivity mirrors in a cavity. Laser pump light is chopped by an AOM to stop the triplet excited state of the dye from being populated, and enters the cavity at an angle-of-incidence corresponding to the maximum of transmission of the mirrors. The photons in the cavity become thermalised and BEC is achieved when the pump intensity goes above a threshold. The cavity length is stabilised with a He-Ne probe laser and spring screws, and the finesse of the cavity is measured with a ringdown measurement.

We took data of photon BECs and below-threshold thermal clouds in an effort to find under which conditions thermalisation breaks down. Data is taken of the threshold power, thermal cloud size and population of photons inside the cavity. We found that a simple homogeneous pumping model cannot explain some of our results. We found the conditions under which thermalisation can be broken, which shows thermalisation is a real effect matching theory and so BEC is a good description of this system. The Kirton and Keeling model[54] explains our results and reproduces our data on threshold power and cavity photon count versus pump spot size.

We have observed the first-order coherence function in photon BEC using an interferometer. Spatial and temporal coherence is much higher above threshold as expected, although our interferometer underestimated the true coherence time and it was recently discovered how to fix this. We observe multimode condensation far above threshold. We have produced results which may be of interest to others investigating condensation phenomena and their coherence, such as exciton-polariton or atomic BEC groups.

We have constructed a 2-dimensional spectrometer that can be configured to be momentum-resolved or position-resolved. We use it to measure any Bogoliubov effects arising from photon-photon interactions and find a value of the dimensionless interaction parameter consistent with other experiments. The strength of any photon-molecule interactions is also very weak, finding that the light is acting as free photons even close to the zero-phonon-line. We also find that effective temperature is not momentum-dependent implying that the system is always ergodic even when it is not at thermal equilibrium. The experimental setup of the 2D spectrometer seems to work well although the spherical aberrations affect measurements at higher momenta. This could potentially be resolved by larger-aperture optics. Energy resolution could be improved by using a grating with finer spaced lines than our 1800 lines/mm.

The laser power was measured and this measurement used to stabilise the power. The measurement was done using a photodiode, sample-and-hold amplifier and PID controller. It is able to quickly change the laser power by having its set-point changed, and it damps the noise from DC up to about 250 Hz. The photon BEC experimental setup could be greatly improved by having two AOMs, one to control the transmission and the other to chop the laser into pulses. This would stop the requirement to limit the speed of PID to less than 500 Hz, and also removes the need for the pulse delaying and sample-and-hold circuits, however it would also result in 40% less laser power due to the loss in an extra AOM.

Outlook

In the future I would like to see the field of photon BEC develop by trying to replace the dye medium with something else. The biggest technical problem with the experiments is the liquid dye often needs to be changed due to evaporation or becoming dusty or dirty. Candidates would ideally be some kind of solid state medium. All that is needed is that the medium follows the Kennard-Stepanov relation and has a strong enough absorption. The group in Utrecht in the 2016 paper de Leeuw[62] suggest nanofabricated semiconductor microcavities to this end which could also provide a way to control the effective photon-photon interactions for measurement.

It would be interesting to see photon BEC created with different potential shapes. There are experiments currently in progress for creating photon BEC with only a small number of photons, lead by Rob Nyman and Ben Walker. These can be created by using cavities with very tight radii of curvature, which can be created using focussed ion beam milling. A further development would be to measure the time-resolved behaviour of a photon BEC with a pulse pump laser, which could lead to observing the formation and decay of BEC. These could both be another way to study condensation under different conditions.

My work from chapter 6 is unfinished. The heat capacity of photon BEC was not measured by me, it should be measured and the work expanded if possible to other thermodynamic properties which could be obtained by similar methods. A further out possible use for photon BEC is investigating photon correlations.

Bibliography

[1] M. H. Anderson, J. R. Ensher, M. R. Matthews, C. E. Wieman, and E. A. Cornell. Observation of bose-einstein condensation in a dilute atomic vapor. *Science*, 269(5221):198–201, 1995.

[2] Roger Bowley and Mariana Sanchez. *Introductory Statistical Mechanics.* Oxford Science Publications, Great Clarendon Street, Oxford, OX2 6DP, second edition, 1999.

[3] J. Bardeen, L. N. Cooper, and J. R. Schrieffer. Theory of superconductivity. *Phys. Rev.*, 108:1175–1204, Dec 1957.

[4] C. J. Pethick, T. Schaefer, and A. Schwenk. Bose-Einstein condensates in neutron stars. *ArXiv e-prints 1507.05839*, July 2015.

[5] O.G. Benvenuto and M.A. De Vito. On the occurrence and detectability of bose-einstein condensation in helium white dwarfs. *Journal of Cosmology and Astroparticle Physics*, 2011(02):033, 2011.

[6] Tiberiu Harko and Gabriela Mocanu. Cosmological evolution of finite temperature Bose-Einstein condensate dark matter. *Physical Review D*, 85(8), APR 12 2012.

[7] Quantum physics; bose einstein condensate. https://archive.is/ilze. NIST Image Gallery. Accessed: 2017-09-01. Source no longer online, only accessible via archiving websites.

[8] P. Kapitza. Viscosity of Liquid Helium below the λ-Point. *Nature*, 141:74, January 1938.

[9] J. F. Allen and A. D. Misener. Flow phenomena in liquid helium ii. *Nature*, 142:643–644, October 1938.

[10] Franco Dalfovo, Stefano Giorgini, Lev P. Pitaevskii, and Sandro Stringari. Theory of bose-einstein condensation in trapped gases. *Rev. Mod. Phys.*, 71:463–512, Apr 1999.

[11] Thilo Stöferle, Henning Moritz, Christian Schori, Michael Köhl, and Tilman Esslinger. Transition from a strongly interacting 1d superfluid to a mott insulator. *Phys. Rev. Lett.*, 92:130403, Mar 2004.

[12] K. Xu, Y. Liu, D. E. Miller, J. K. Chin, W. Setiawan, and W. Ketterle. Observation of strong quantum depletion in a gaseous bose-einstein condensate. *Phys. Rev. Lett.*, 96:180405, May 2006.

[13] M. Hartmann, R. E. Miller, J. P. Toennies, and A. Vilesov. Rotationally resolved spectroscopy of sf_6 in liquid helium clusters: A molecular probe of cluster temperature. *Phys. Rev. Lett.*, 75:1566–1569, Aug 1995.

[14] K. B. Davis, M. O. Mewes, M. R. Andrews, N. J. van Druten, D. S. Durfee, D. M. Kurn, and W. Ketterle. Bose-einstein condensation in a gas of sodium atoms. *Phys. Rev. Lett.*, 75:3969–3973, Nov 1995.

[15] C. C. Bradley, C. A. Sackett, J. J. Tollett, and R. G. Hulet. Evidence of bose-einstein condensation in an atomic gas with attractive interactions. *Phys. Rev. Lett.*, 75:1687–1690, Aug 1995.

[16] Dale G. Fried, Thomas C. Killian, Lorenz Willmann, David Landhuis, Stephen C. Moss, Daniel Kleppner, and Thomas J. Greytak. Bose-einstein condensation of atomic hydrogen. *Phys. Rev. Lett.*, 81:3811–3814, Nov 1998.

[17] G. Modugno, G. Ferrari, G. Roati, R. J. Brecha, A. Simoni, and M. Inguscio. Bose-einstein condensation of potassium atoms by sympathetic cooling. *Science*, 294(5545):pp. 1320–1322, 2001.

[18] A. L. Fetter and A. A. Svidzinsky. Topical Review: Vortices in a trapped dilute Bose-Einstein condensate. *Journal of Physics Condensed Matter*, 13:135, March 2001.

[19] S. Dettmer, D. Hellweg, P. Ryytty, J. J. Arlt, W. Ertmer, K. Sengstock, D. S. Petrov, G. V. Shlyapnikov, H. Kreutzmann, L. Santos, and M. Lewenstein. Observation of phase fluctuations in elongated bose-einstein condensates. *Phys. Rev. Lett.*, 87:160406, Oct 2001.

[20] C. Kittel. *Introduction to Solid State Physics.* John Wiley and Sons Inc., seventh edition, 1996.

[21] Iacopo Carusotto and Cristiano Ciuti. Quantum fluids of light. *Rev. Mod. Phys.*, 85:299–366, Feb 2013.

[22] J. J. Baumberg, P. G. Savvidis, R. M. Stevenson, A. I. Tartakovskii, M. S. Skolnick, D. M. Whittaker, and J. S. Roberts. Parametric oscillation in a vertical microcavity: A polariton condensate or micro-optical parametric oscillation. *Phys. Rev. B*, 62:R16247–R16250, Dec 2000.

[23] R. M. Stevenson, V. N. Astratov, M. S. Skolnick, D. M. Whittaker, M. Emam-Ismail, A. I. Tartakovskii, P. G. Savvidis, J. J. Baumberg, and J. S. Roberts. Continuous wave observation of massive polariton redistribution by stimulated scattering in semiconductor microcavities. *Phys. Rev. Lett.*, 85:3680–3683, Oct 2000.

[24] A. Baas, J.-Ph. Karr, M. Romanelli, A. Bramati, and E. Giacobino. Quantum degeneracy of microcavity polaritons. *Phys. Rev. Lett.*, 96:176401, May 2006.

[25] J. Kasprzak, M. Richard, S. Kundermann, A. Baas, P. Jeambrun, J. M. J. Keeling, F. M. Marchetti, M. H. Szymanska, R. Andre, J. L. Staehli, V. Savona, P. B. Littlewood, B. Deveaud, and Le Si Dang. Bose-einstein condensation of exciton polaritons. *Nature*, 443:409–414, September 2006.

[26] R. Balili, V. Hartwell, D. Snoke, L. Pfeiffer, and K. West. Bose-einstein condensation of microcavity polaritons in a trap. *Science*, 316(5827):1007–1010, 2007.

[27] H Deng, G Weihs, C Santori, J Bloch, and Y Yamamoto. Condensation of semiconductor microcavity exciton polaritons. *Science*, 298(5591):199–202, OCT 4 2002.

[28] Hui Deng, Glenn S. Solomon, Rudolf Hey, Klaus H. Ploog, and Yoshihisa Yamamoto. Spatial coherence of a polariton condensate. *Physical Review Letters*, 99(12), SEP 21 2007.

[29] Yongbao Sun, Patrick Wen, Yoseob Yoon, Gangqiang Liu, Mark Steger, Loren N. Pfeiffer, Ken West, David W. Snoke, and Keith A. Nelson. Bose-einstein condensation of long-lifetime polaritons in thermal equilibrium. *Phys. Rev. Lett.*, 118:016602, Jan 2017.

[30] K. S. Daskalakis, S. A. Maier, R. Murray, and S. Kena-Cohen. Nonlinear interactions in an organic polariton condensate. *Nature Materials*, 13(3):272–279, MAR 2014.

[31] Johannes D. Plumhof, Thilo Stoeferle, Lijian Mai, Ullrich Scherf, and Rainer F. Mahrt. Room-temperature Bose-Einstein condensation of cavity exciton-polaritons in a polymer. *Nature Materials*, 13(3):248–253, MAR 2014.

[32] Alexey V. Kavokin, Jeremy J. Baumberg, Guillaume Malpuech, and Fabrice P. Laussy. *Microcavities.* Oxford University Press, Great Clarendon Street, Oxford, OX2 6DP, second edition, 2007.

[33] R. A. Nyman and M. H. Szymańska. Interactions in dye-microcavity photon condensates and the prospects for their observation. *Phys. Rev. A*, 89:033844, Mar 2014.

[34] F.P. Schafer, B.B. Snavely, H. Gerhardt, C.V. Shank, E.P. Ippen, K.H. Drexhage, J.J. Snyder, and T.W. Hansch. *Topics in Applied Physics - Dye Lasers.* Springer-Verlag Berlin Heidelberg GmbH, New York, third edition, 1989.

[35] F.J. Duarte and Lloyd W. Hillman. *Dye Laser Principles with Applications.* Academic Press Inc., 1250 Sixth Avenue, San Diego, CA 92101, first edition, 1990.

[36] Jan Klaers, Julian Schmitt, Frank Vewinger, and Martin Weitz. Bose-Einstein condensation of photons in an optical microcavity. *Nature*, 468(7323):545–548, NOV 25 2010.

[37] Peter Moroshkin, Lars Weller, Anne Sass, Jan Klaers, and Martin Weitz. Kennard-Stepanov Relation Connecting Absorption and Emission Spectra in an Atomic Gas. *Physical Review Letters*, 113(6), AUG 6 2014.

[38] Jan Klaers, Frank Vewinger, and Martin Weitz. Thermalization of a two-dimensional photonic gas in a 'white wall' photon box. *Nature Physics*, 6(7):512–515, JUL 2010.

[39] J. Klaers, J. Schmitt, T. Damm, F. Vewinger, and M. Weitz. Bose-einstein condensation of paraxial light. *Applied Physics B*, 105(1):17–33, 2011.

[40] Jan Klaers, Julian Schmitt, Tobias Damm, Frank Vewinger, and Martin Weitz. Statistical physics of bose-einstein-condensed light in a dye microcavity. *Phys. Rev. Lett.*, 108:160403, Apr 2012.

[41] Julian Schmitt, Tobias Damm, David Dung, Frank Vewinger, Jan Klaers, and Martin Weitz. Observation of grand-canonical number statistics in a photon bose-einstein condensate. *Phys. Rev. Lett.*, 112:030401, Jan 2014.

[42] Julian Schmitt, Tobias Damm, David Dung, Frank Vewinger, Jan Klaers, and Martin Weitz. Thermalization kinetics of light: From laser dynamics to equilibrium condensation of photons. *Physical Review A*, 92(1), JUL 27 2015.

[43] Julian Schmitt, Tobias Damm, Frank Vewinger, Martin Weitz, and Jan Klaers. Thermalization of a two-dimensional photon gas in a polymeric host matrix. *New Journal of Physics*, 14, JUL 20 2012.

[44] Julian Schmitt, Tobias Damm, David Dung, Christian Wahl, Frank Vewinger, Jan Klaers, and Martin Weitz. Spontaneous Symmetry Breaking and Phase Coherence of a Photon Bose-Einstein Condensate Coupled to a Reservoir. *Physical Review Letters*, 116(3), JAN 22 2016.

[45] Tobias Damm, Julian Schmitt, Qi Liang, David Dung, Frank Vewinger, Martin Weitz, and Jan Klaers. Calorimetry of a Bose-Einstein-condensed photon gas. *Nature Communications*, 7, APR 2016.

[46] David Dung, Christian Kurtscheid, Tobias Damm, Julian Schmitt, Frank Vewinger, Martin Weitz, and Jan Klaers. Variable potentials for thermalized light and coupled condensates. *Nature Photonics*, 11(9):565+, SEP 2017.

[47] Tobias Damm, David Dung, Frank Vewinger, Martin Weitz, and Julian Schmitt. First-order spatial coherence measurements in a thermalized two-dimensional photonic quantum gas. *Nature Communications*, 8, JUL 31 2017.

[48] J. Marelic and R. A. Nyman. Experimental evidence for inhomogeneous pumping and energy-dependent effects in photon bose-einstein condensation. *Phys. Rev. A*, 91:033813, Mar 2015.

[49] Jakov Marelic, Lydia F Zajiczek, Henry J Hesten, Kon H Leung, Edward YXOng, Florian Mintert, and Robert A Nyman. Spatiotemporal coherence of non-equilibrium multimode photon condensates. *New Journal of Physics*, 18(10):103012, 2016.

[50] Jakov Marelic, Benjamin T. Walker, and Robert A. Nyman. Phase-space views into dye-microcavity thermalized and condensed photons. *Physical Review A*, 94(6), DEC 5 2016.

[51] R. A. Nyman and B. T. Walker. Bose-Einstein condensation of photons from the thermodynamic limit to small photon numbers. *ArXiv e-prints 1706.09645*, June 2017.

[52] Peter Kirton and Jonathan Keeling. Nonequilibrium model of photon condensation. *Phys. Rev. Lett.*, 111:100404, Sep 2013.

[53] Peter Kirton and Jonathan Keeling. Thermalization and breakdown of thermalization in photon condensates. *Phys. Rev. A*, 91:033826, Mar 2015.

[54] Jonathan Keeling and Peter Kirton. Spatial dynamics, thermalization, and gain clamping in a photon condensate. *Physical Review A*, 93(1), JAN 14 2016.

[55] Robert Andrew Nyman. Absorption and fluorescence spectra of rhodamine 6g. https://zenodo.org/record/569817#.WRHxZje1sUQ. [Online; accessed 5-October-2017].

[56] Wassilij Kopylov, Milan Radonjić, Tobias Brandes, Antun Balaž, and Axel Pelster. Dissipative two-mode tavis-cummings model with time-delayed feedback control. *Phys. Rev. A*, 92:063832, Dec 2015.

[57] A. W. de Leeuw, H. T. C. Stoof, and R. A. Duine. Phase fluctuations and first-order correlation functions of dissipative Bose-Einstein condensates. *Physical Review A*, 89(5), MAY 29 2014.

[58] E. C. I. van der Wurff, A.-W. de Leeuw, R. A. Duine, and H. T. C. Stoof. Interaction effects on number fluctuations in a bose-einstein condensate of light. *Phys. Rev. Lett.*, 113:135301, Sep 2014.

[59] A. W. de Leeuw, H. T. C. Stoof, and R. A. Duine. Schwinger-Keldysh theory for Bose-Einstein condensation of photons in a dye-filled optical microcavity. *Physical Review A*, 88(3), SEP 18 2013.

[60] A.-W. de Leeuw, O. Onishchenko, R. A. Duine, and H. T. C. Stoof. Effects of dissipation on the superfluid-mott-insulator transition of photons. *Phys. Rev. A*, 91:033609, Mar 2015.

[61] A.-W. de Leeuw, E. C. I. van der Wurff, R. A. Duine, and H. T. C. Stoof. Phase diffusion in a bose-einstein condensate of light. *Phys. Rev. A*, 90:043627, Oct 2014.

[62] A. W. de Leeuw, E. C. I. van der Wurff, R. A. Duine, D. van Oosten, and H. T. C. Stoof. Theory for Bose-Einstein condensation of light in nanofabricated semiconductor microcavities. *Physical Review A*, 94(1), JUL 22 2016.

[63] Marjan Fani and M. H. Naderi. Thermalization and Bose-Einstein condensation of a photon gas in a multimode hybrid atom-membrane optomechanical microcavity. *Journal of the Optical Society of America B-Optical Physics*, 33(6):1242–1250, JUN 1 2016.

[64] Denis Nikolaevich Sob'yanin. Hierarchical maximum entropy principle for generalized superstatistical systems and Bose-Einstein condensation of light. *Physical Review E*, 85(6, 1), JUN 20 2012.

[65] Denis Nikolaevich Sob'yanin. Bose-Einstein condensation of light: General theory. *Physical Review E*, 88(2), AUG 19 2013.

[66] Eran Sela, Achim Rosch, and Victor Fleurov. Condensation of photons coupled to a Dicke field in an optical microcavity. *Physical Review A*, 89(4), APR 30 2014.

[67] Photon bec github. https://github.com/coldmatter/photonbec, 2017.

[68] Alex Kruchkov. Bose-einstein condensation of light in a cavity. *Phys. Rev. A*, 89:033862, Mar 2014.

[69] M. Fattori, C. D'Errico, G. Roati, M. Zaccanti, M. Jona-Lasinio, M. Modugno, M. Inguscio, and G. Modugno. Atom interferometry with a weakly interacting Bose-Einstein condensate. *Physical Review Letters*, 100(8), FEB 29 2008.

[70] Georgios Roumpos, Michael Lohse, Wolfgang H. Nitsche, Jonathan Keeling, Marzena Hanna Szymaska, Peter B. Littlewood, Andreas Lffler, Sven Hfling, Lukas Worschech, Alfred Forchel, and Yoshihisa Yamamoto. Power-law decay of the spatial correlation function in exciton-polariton condensates. *Proceedings of the National Academy of Sciences*, 109(17):6467–6472, 2012.

[71] Rodney Loudon. *The Quantum Theory of Light*. Oxford University Press, Great Clarendon Street, Oxford OX2 6DP, third edition, 2000.

[72] Lydia Zajiczek. An Optical Interferometer for Investigating the Coherence Properties of a Photon Bose-Einstein Condensate. Master's thesis, Imperial College London, Physics Department, South Kensington Campus, London SW7 2AZ, UK, 2014.

[73] M. Kohnen and R. A. Nyman. Temporal and spatiotemporal correlation functions for trapped Bose gases. *Physical Review A*, 91(3), MAR 10 2015.

[74] Timothy Evans. Lecture notes for quantum theory of matter. University Lecture, 2012.

[75] S. Utsunomiya, L. Tian, G. Roumpos, C. W. Lai, N. Kumada, T. Fujisawa, M. Kuwata-Gonokami, A. Loeffler, S. Hoefling, A. Forchel, and Y. Yamamoto. Observation of Bogoliubov excitations in exciton-polariton condensates. *Nature Physics*, 4(9):700–705, SEP 2008.

[76] Eugene Hecht. *Optics*. Addison Wesley, San Francisco, fourth edition, 2002.

[77] Hui Deng, Hartmut Haug, and Yoshihisa Yamamoto. Exciton-polariton bose-einstein condensation. *Rev. Mod. Phys.*, 82:1489–1537, May 2010.

[78] W. H. Keesom and A. P. Keesom. New measurements on the specific heat of liquid helium. *Physica*, 2:557–572, 1935.

[79] K. Mendelssohn. *The Quest for Absolute Zero*. Taylor & Francis Ltd, 10-14 Macklin Street, London, WC2B 5NF, second edition, 1977.

[80] W. H Keesom and K Clusius. *Commun. Phys. Lab. Univ. Leiden*, 1931.

[81] F. London. The λ-phenomenon of liquid helium and the bose-einstein degeneracy. *Nature*, 141(3571):643–644, April 1938.

[82] JR Ensher, DS Jin, MR Matthews, CE Wieman, and EA Cornell. Bose-Einstein condensation in a dilute gas: Measurement of energy and ground-state occupation. *Physical Review Letters*, 77(25):4984–4987, DEC 16 1996.

[83] T Haugset, H Haugerud, and JO Andersen. Bose-Einstein condensation in anisotropic harmonic traps. *Physical Review A*, 55(4):2922–2929, APR 1997.

[84] B. Klünder and A. Pelster. Systematic semiclassical expansion for harmonically trapped ideal bose gases. *The European Physical Journal B*, 68(3):457, 2009.

[85] John G. Proakis and Dimitris G. Manolakis. *Digital Signal Processing.* Pearson Prentice Hall, Upper Saddle River, New Jersey 07458, fourth edition, 2007.